Investigation of noise sources in the LTP interferometer
S2-AEI-TN-3028
Version 1.2 2008/07/01

G. Heinzel, V. Wand, A. García, F. Guzmán, F. Steier,
AEI Hannover,

C. Killow, D. Robertson, H. Ward,
University of Glasgow,

C. Braxmaier,
EADS Astrium Immenstaad*

July 1, 2008

*now at the University of Applied Sciences (Fachhochschule) Konstanz.

Abstract

All breadboards for the LTP interferometer showed an extra noise term that was, until recently, not fully understood. In this report that noise term is investigated in detail. It turns out that it is caused by sidebands on the light. In our lab, these sidebands were caused by nonlinear mixing processes in the power amplifiers that drive the AOM, if electromagnetic interference at a frequency near the operating frequency ($\approx 80\,\mathrm{MHz}$) is picked up by the power amplifier. The disturbing nearby frequency is the frequency of the other AOM, with a difference of exactly f_{het}, causing multiple sidebands at integer multiples of f_{het} from the carrier. They appear as pairs with a phase relationship that corresponds to phase-modulation (PM).

Experiments with a very different electrical setup (in Glasgow) also showed sidebands which demonstrates that they are not caused by peculiarities of the Hannover setup.

While the effect of a pair of first-order PM sidebands cancels and causes no harm, only one of the second-order sidebands produces noise which cannot be cancelled by its second-order mirror image. Hence the second-order sidebands are the dominant noise source.

Various strategies of mitigation are also investigated. The two most important ones, both of which are already implemented as baseline for the LTP interferometer, are (1) to reduce the sidebands by careful EMC design and dedicated testing, and (2) to stabilize the optical pathlength difference (OPD) between the two fibers with a Piezo device. The combination of these two measures will reduce this error term to insignificance.

We have also investigated other noise sources such as laser amplitude noise and beam jitter noise. Laser amplitude noise does have an influence on the total performance of the interferometer. Using a laser amplitude stabilization (part of the baseline), its influence can also be sufficiently reduced. Contrary to earlier worries, we did not find a significant noise contribution from beam jitter noise in conjunction with quadrant photodiodes.

As part of this investigation we have also developed a mathematical model for the sideband coupling that fully describes their effect and has been experimentally verified. Furthermore we have developed various numerical procedures to find correlations between auxiliary data streams (such as alignment signals) and the main interferometer output. They are useful for diagnostic purposes, but in general too complex to implement on LTP.

Using only those procedures that are the baseline for the FM, the noise performance of the LTP EM interferometer in the lab is now well below its specifications at all frequencies, with remaining noise sources mainly driven by ground-based disturbances, such that we are confident that the LTP interferometer will perform well on orbit and will enable the detailed study of the behaviour and noise performance of the inertial sensor and DFACS systems, which indeed is the primary job of the interferometer.

Contents

List of Figures

Glossary

Some commonly used terms, abbreviations and symbols are listed here with a short description of their usual meaning in this work.

AEI: Max-Planck-Institut für Gravitationsphysik (Albert-Einstein-Institut); in this document the experimenal section in Hannover, Germany.

AM: amplitude modulation.

AOM: an acousto-optic modulator (used to shift the frequency of a light beam).

beam injector, also fibre launcher or collimator: The optical component that emits a collimated free-space beam that comes from an optical fiber.

BS: a beamsplitter, usually **the** main beamsplitter of a Michelson interferometer.

CCD: charge-coupled device.

DC: the average of a fluctuating signal; also used to indicate the limit of some function for low frequencies.

EM: Engineering model

LPF: LISA Pathfinder

LTP: LISA technology package, the European scientific payload on LPF

M: a mirror.

OB: Optical Bench

OPD: Optical Pathlength Difference (between two fiber paths), also called Δ_F.

PD: a photodiode.

PDM: photodiode in the 'measurement' interferometer (can stand for one of PD1, PD12 or PDF depending on configuration of the particular experiment).

PDF: photodiode in the frequency interferometer.

PDR: photodiode in the reference interferometer..

PD1: photodiode in the x_1 interferometer.

PD12: photodiode in the $x_1 - x_2$ interferometer.

Piezo: a piezo-electric transducer, used to control the microscopic position of a mirror; see also 'PZT'.

PM: Phase modulation.

PZT: originally 'Lead Zirconate Titanate', $\mathrm{Pb}\,(\mathrm{Zr}_{0.52}\mathrm{Ti}_{0.48})\,\mathrm{O}_3$, a piezoelectric material; often 'PZT' is used as a synonym for a piezo-electric transducer.

RF: radio frequency (here usually around 80 MHz).

rms: root mean square.

SBDFT: Single bin discrete Fourier transform

SNR: signal-to-noise ratio.

TNO: The Netherlands Organisation for Applied Scientific Research (TNO), Technisch Physische Dienst (TPD), Delft, The Netherlands [location of OB test campaign in 2004].

VCXO: a voltage-controlled crystal oscillator (driving the AOM).

---

a, b: amplitudes of various light beams in models.

a_{-2}, a_{-1},... b_{+2}: amplitudes of sidebands on the light (see Section 3).

c: the speed of light in vacuum, 299792458 m/s.

f: a frequency with the unit Hz.

f_{het}: the heterodyne frequency, 1623 Hz in our experiments.

I: a current, in particular a photocurrent.

i: $\sqrt{-1}$.

$J_0, J_1, \ldots$ the Bessel functions of the first kind (see Section A.1).

L: a physical distance or optical pathlength in the interferometer (see Section 2).

m: modulation index (in radians) of a modulation, usually a phase modulation (see Section A.1).

R: a radius of curvature (of a mirror or wavefront); also a resistor or its resistance (in Ohms).

U: a voltage.

Z: an impedance (usually complex).

α, β, γ: Various phase offsets.

α_1, α_2, ...: fit coefficients in noise correlation models.

Δ: a pathlength difference in the interferometer, expressed as phase (see Section 2).

Δ_F: the pathlength difference between the two fiber paths expressed as phase (see Section 2). Same as OPD.

ε: Ratio of sideband amplitude to carrier amplitude. If nothing else is mentioned, $\varepsilon_{\mathrm{opt}}$ is meant.

$\varepsilon_{\mathrm{opt}}$: Ratio of sideband amplitude to carrier amplitude in the light.

$\varepsilon_{\mathrm{el}}$: Ratio of sideband amplitude to carrier amplitude in the AOM RF drive signal.

λ: the wavelength of the light, 1064 nm in LTP.

φ: a phase at f_{het} measured with the phasemeter in the heterodyne interferometer to represent an optical pathlength, in particular $\varphi = \varphi_R - \varphi_M$ (see Section 2).

φ_M: measured phase in the 'measurement' interferometer (see Section 2).

φ_R: measured phase in the Reference interferometer (see Section 2).

φ_{el}: phase of the electrical oscillator that produces f_{het}.

ω: an angular frequency $\omega = 2\pi f$ with the unit rad/s.

ω_{m}: an angular modulation frequency, often $\omega_{\mathrm{m}} = 2\pi f_{\mathrm{het}}$.

$\Re\{z\}$: the real part of the complex number z.

$\Im\{z\}$: the imaginary part of the complex number z.

$\tilde{x}$: the linear spectral density of x, with the unit of x divided by $\sqrt{\mathrm{Hz}}$.

Changelog

1.1 initial public release

1.2 2008-07-01 label of y-axes in Figures 51–53 corrected

1 Introduction

The LISA Technology Package (LTP) aboard the LISA pathfinder mission is dedicated to demonstrate and verify key technologies for LISA, in particular drag free control, ultra-precise laser interferometry and gravitational sensors.

Essential parts of the LTP are the inertial sensors and the optical interferometry. The validation and diagnostics of the drag free operation in orbit will be done by measuring laser-interferometrically the relative displacement between two test masses (and the optical bench) with a noise level of $10\,\mathrm{pm}/\sqrt{\mathrm{Hz}}$ between 3 mHz and 30 mHz. Heterodyne Mach-Zehnder interferometry was selected as baseline for LTP due to its ability to operate with constant sensitivity at any operating point within a range of many fringes.

It has long been known that heterodyne interferometers can suffer from a periodic nonlinearity on the nm level (see References in Appendix G on page 138). Most of these observations were done in polarizing interferometers, and noise sources could often be traced to polarization phenomena.

We (the EM OB study team) have on purpose chosen a non-polarizing interferometer for LTP. However, we also observed unexpected noise sources. In our project, they were first described at a meeting by D. Robertson [1]. Comparable phenomena had also been observed as early as 2002 in table-top experiments in Hannover.

The magnitude of the noise is shown in Figure 1 on the following page, using data taken during the measurement campaign at TNO in 2004. The upper curve shows the noise level in the basic setup without OPD stabilization, clearly showing a noise level that is unacceptably high and demonstrating the necessity to mitigate that noise. The middle curve shows the enormous improvement that is achieved when the optical pathlength difference (OPD) between the two fibers is actively stabilized. For comparison, the lowest curve shows a recent noise spectrum using the new phasemeter and other improvements.

The noise has a characteristic appearance in the time domain. As an example, Figure 2 on page 13 shows one time series of the φ measurement, measured by AEI at TNO using the LTP EM. During that measurement, the interferometer was in air such that φ showed understandable slow drifts, which were subtracted. The fiber pathlength difference Δ_F was freely drifting (several fringes per minute, see Section 7 on page 50), and the error term shows up as a quasiperiodic variation of φ with a slowly fluctuating amplitude of up to several mrad.

The main purpose of the present investigation was to understand the origin of the noise and investigate methods for its mitigation, in particular the active stabilization of the optical pathlength difference (OPD).

In addition to those primary goals, which have fully been achieved, a number of other results have also been obtained in the course of the investigation.

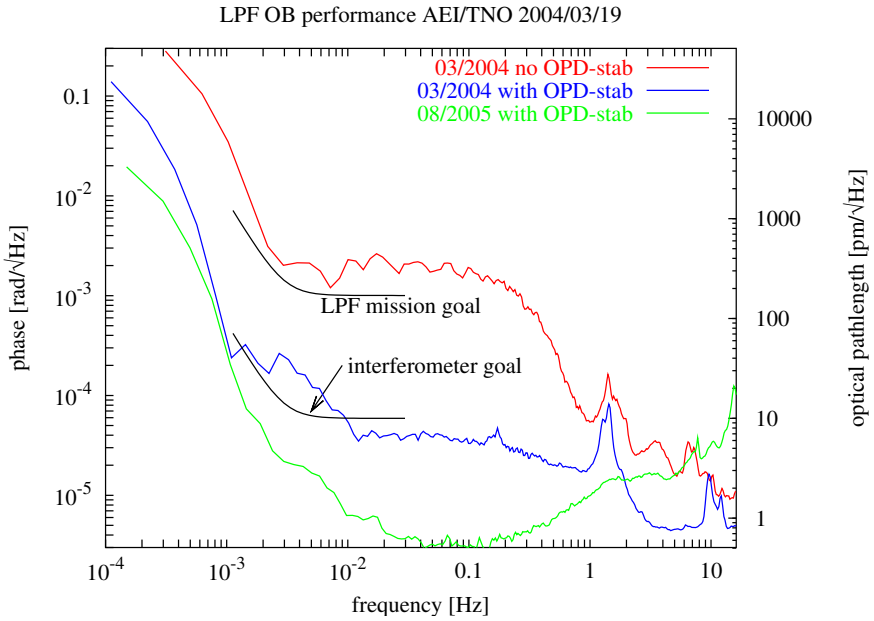

Figure 1: Performance test results with and without active suppression of the differential OPD noise. The upper two curves show data taken in 2004 during the tests at TNO.

2 Basic setup and observations

The noise term can best be described using a sketch of a simplified interferometer (Figure 3 on page 14).

The laser light is split into two equal parts at beamsplitter BS. Each part is frequency-shifted by an acousto-optic modulator AOM, operating at frequencies f_1 and f_2, respectively. While $f_1 \approx f_2 \approx 80\,\mathrm{MHz}$, their difference is fixed to the preselected heterodyne frequency: $f_1 - f_2 = f_{\mathrm{het}} \approx 1\,\mathrm{kHz}$. This frequency is produced by an electrical oscillator, which is coherent to the system clock, as are the clocks of the data acquisition and the phasemeter clock, and its phase is called φ_{el}. In all our experiments, the heterodyne frequency was $f_{\mathrm{het}} = 10\,\mathrm{MHz}/6160 \approx 1623.376\,\mathrm{Hz}$.

At photodiodes PDR (reference) and PDM (measurement), beams of the two different frequencies are recombined and produce a beatnote of frequency f_{het}. The primary observables are the phases of these beatnotes (φ_R and φ_M), which are referred to the phase φ_{el} of the electrical reference oscillator.

Their dependence on the optical pathlengths can be simplified as follows for the present discussion:

$$\begin{aligned} \varphi_R &= \frac{2\,\pi}{\lambda}\,(L_1 + L_{1R} - L_2 - L_{2R})\,, \\ \varphi_M &= \frac{2\,\pi}{\lambda}\,(L_1 + L_{1M} - L_2 - L_{2M})\,. \end{aligned} \tag{1}$$

While the part of the interferometer that defines the distances L_{1M}, L_{1R}, L_{2M} and L_{2R} is constructed by monolithic bonding on the very stable Zerodur baseplate and is furthermore located in a thermally very stable environment, all pathlengths associated with the laser, AOMs

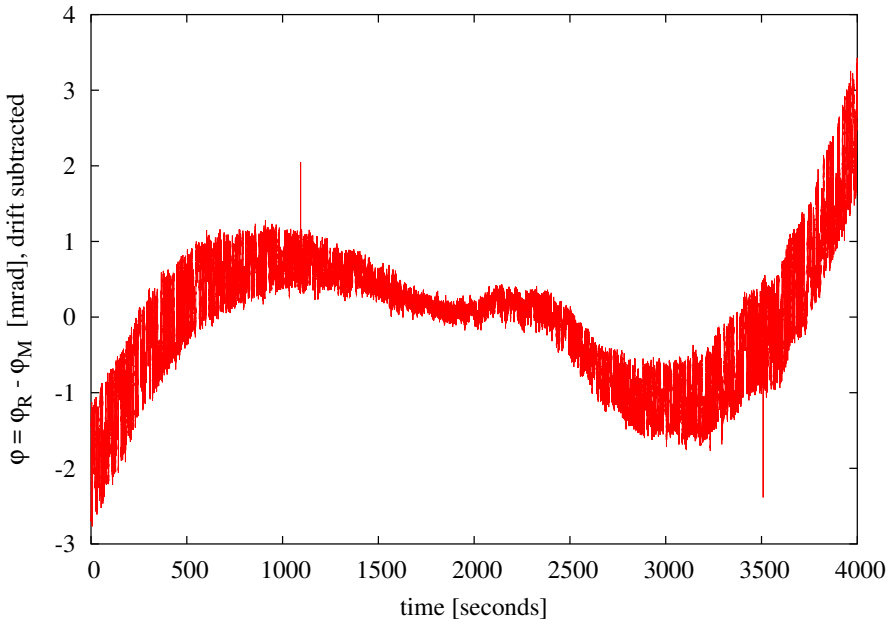

Figure 2: Time series of a φ measurement without Δ_F stabilization, taken by AEI at TNO using the LTP EM (03/2004). A linear drift was subtracted.

and fibers have much less stability. In the lab, these latter pathlengths typically fluctuate by several fringes per minute (see Section 7 on page 50), and no data is available on how strong the fluctuations on orbit might be.

We introduce the phases

$$\begin{aligned}\Delta_F &= \frac{2\,\pi}{\lambda}(L_1 - L_2),\\ \Delta_R &= \frac{2\,\pi}{\lambda}(L_{1R} - L_{2R}),\\ \Delta_M &= \frac{2\,\pi}{\lambda}(L_{1M} - L_{2M}),\end{aligned} \tag{2}$$

which represent differential pathlength fluctuations of the unstable part (mostly the fibers), the stable reference interferometer and the stable measurement interferometer, respectively and neglect any static pathlength differences.

The primary observables thus become

$$\begin{aligned}\varphi_R &= \Delta_F + \Delta_R,\\ \varphi_M &= \Delta_F + \Delta_M.\end{aligned} \tag{3}$$

The main measurement consists of taking the difference between φ_R and φ_M:

$$\varphi = \varphi_R - \varphi_M. \tag{4}$$

Ideally, Δ_F should cancel and φ should represent the test mass motion Δ_M, provided that the reference path on the optical bench Δ_R is stable. Experimentally, this is true to the mrad

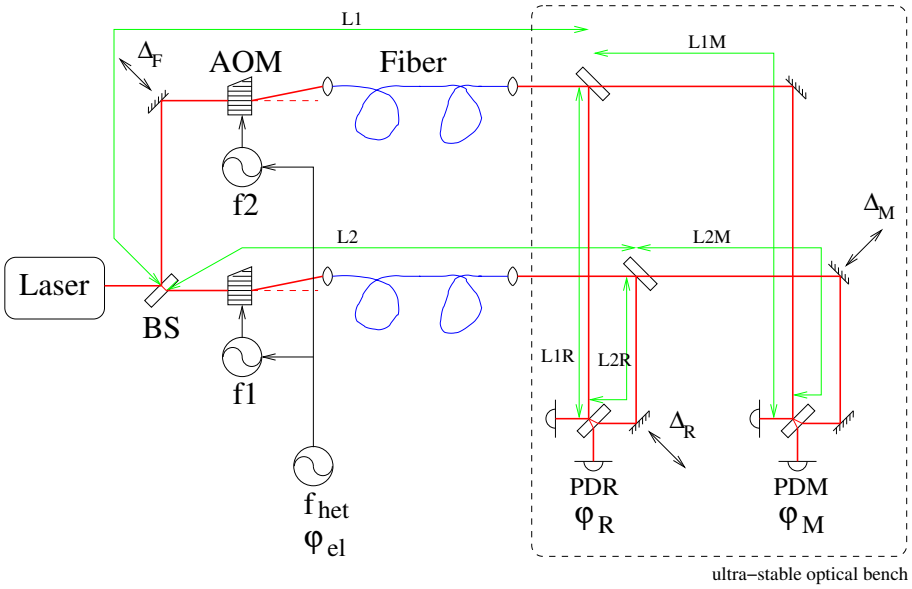

Figure 3: Simplified diagram of a heterodyne interferometer. Optical pathlengths are symbolized by L_1, L_{1a}, etc. and are meant to be measured from and to the respective beamsplitting surfaces.

(equivalently nm) level. Looking more closely, however, one discovers that φ is not perfectly independent of the fiber pathlength difference Δ_F, even if both Δ_R and Δ_M are stable.

Figure 4 on the next page shows such a measurement, taken with the LTP OB EM. Δ_F was intentionally scanned over several fringes with a PZT actuator, while Δ_R and Δ_M were stable during the duration of these measurements.

The error in φ has two main components: one that varies with $\sin(\Delta_F + \alpha)$ and another one that varies with $\sin(2\Delta_F + \beta)$, where α and β are phases that vary from one experiment to another. In most cases, the $\sin(2\Delta_F + \beta)$ is dominant.

One result of this study is a consistent explanation of both these components in terms of sidebands on the light, which are caused by electrical sidebands on the AOM driving signal.

3 Sideband-induced noise: Theory

Early in the study it was discovered that the light in each of the two channels, which should ideally be monochromatic and separated by $f_{\rm het}$, contains additional frequency components that are separated by integer multiples of $f_{\rm het}$ from the nominal frequency. Most easy to understand is the occurence of the each frequency in the other channel, which can be caused by electrical crosstalk between the two AOM drivers and/or AOMs. Measurements (see Section 8 on page 52) showed, however, that in addition sidebands at offsets of $\pm f_{\rm het}$ and $\pm 2 \times f_{\rm het}$ from the carrier are present in both beams. This section examines the effect of such sidebands, while their possible origin mechanism and mitigation will be examined in later Sections.

Figure 5 on page 16 illustrates the sidebands at offsets of $\pm f_{\rm het}$ and $\pm 2 \times f_{\rm het}$ from each carrier and their frequency relationships.

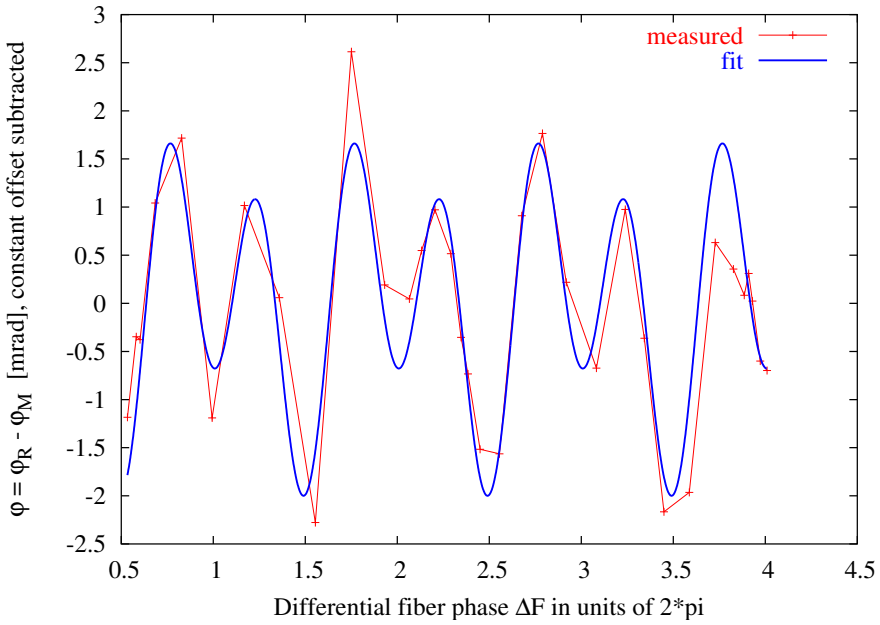

Figure 4: Measurement of the periodic nonlinearity in the LTP EM interferometer (measured by AEI at TNO Delft 03/2004). The $\sin(\Delta_F)$ component has an amplitude of 0.72 mrad, while the $\sin(2\Delta_F)$ component has an amplitude of 1.33 mrad. See also Figure 27 on page 42 for a similar, more recent, measurement.

The two beams are described mathematically by

$$\begin{aligned} e_1 &= \exp(\,\mathrm{i}\,\omega_0 t) + a_{-2}\exp(\,\mathrm{i}\,(\omega_0 - 2\omega_\mathrm{m})t) + a_{-1}\exp(\,\mathrm{i}\,(\omega_0 - \omega_\mathrm{m})t) \\ &\quad + a_{+1}\exp(\,\mathrm{i}\,(\omega_0 + \omega_\mathrm{m})t) + a_{+2}\exp(\,\mathrm{i}\,(\omega_0 + 2\omega_\mathrm{m})t), \\ e_2 &= \exp(\,\mathrm{i}\,(\omega_0 + \omega_\mathrm{m})t) + b_{-2}\exp(\,\mathrm{i}\,(\omega_0 - \omega_\mathrm{m})t) + b_{-1}\exp(\,\mathrm{i}\,\omega_0 t) \\ &\quad + b_{+1}\exp(\,\mathrm{i}\,(\omega_0 + 2\omega_\mathrm{m})t) + b_{+2}\exp(\,\mathrm{i}\,(\omega_0 + 3\omega_\mathrm{m})t), \end{aligned} \tag{5}$$

where equal and unity carrier amplitude for both beams has been assumed. This general expression includes all possible first- and second-order sidebands on both beams.

Without loss of generality, all phaseshifts can be assigned to one of the two beams (beam 2). The field amplitude at the photodiodes is then given by

$$\begin{aligned} e_\mathrm{M} &= e_1 + \exp(-\,\mathrm{i}\,(\Delta_\mathrm{F} + \Delta_\mathrm{M}))e_2, \\ e_\mathrm{R} &= e_1 + \exp(-\,\mathrm{i}\,(\Delta_\mathrm{F} + \Delta_\mathrm{R}))e_2, \end{aligned} \tag{6}$$

for the measurement and the reference interferometer, respectively.

The photocurrent in each interferometer is proportional to $|e|^2 = ee^*$, which is a lengthy

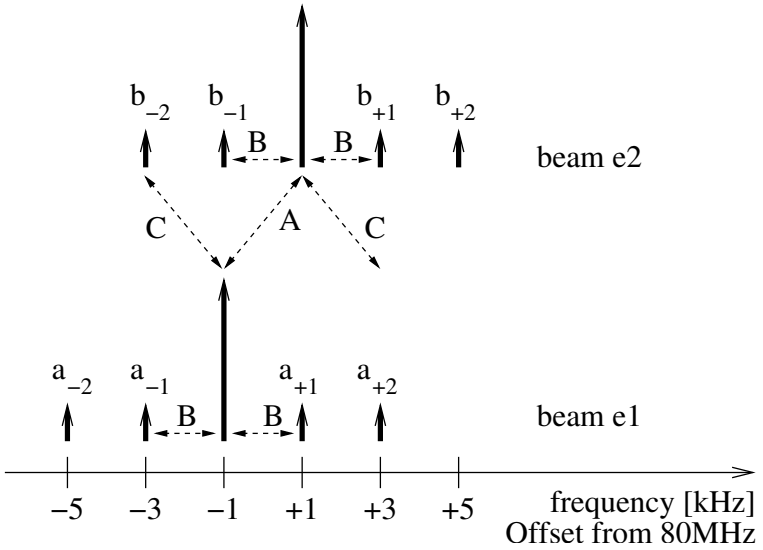

Figure 5: Illustration of the sidebands at offsets of $\pm f_{\mathrm{het}}$ and $\pm 2 \times f_{\mathrm{het}}$ from both beams. The fat vertical arrows represent the light amplitudes, while the dashed arrow 'A' represents the main carrier-carrier beat (desired), and 'B' and 'C' two types of undesired beat notes. For simplicity, $f_{\mathrm{het}} = 2\,\mathrm{kHz}$ has been chosen in this illustration.

expression such as:

$$
\begin{aligned}
&|e_{\mathrm{M}}|^2 = \\
&2 + {a_{-1}}^2 + {a_{-2}}^2 + {a_{+1}}^2 + {a_{+2}}^2 + {b_{-1}}^2 + {b_{-2}}^2 + {b_{+1}}^2 + {b_{+2}}^2 \\
&+ 2\,(a_{-1} + a_{-1}\,a_{-2} + a_{+1} + a_{+1}\,a_{+2} + b_{-1} + b_{-1}\,b_{-2} + b_{+1} + b_{+1}\,b_{+2})\,\cos(\omega_{\mathrm{m}} t) \\
&+ 2\,(a_{-2} + a_{-1}\,a_{+1} + a_{+2} + b_{-2} + b_{-1}\,b_{+1} + b_{+2})\,\cos(2\,\omega_{\mathrm{m}} t) \\
&+ 2\,(a_{-2}\,a_{+1} + a_{-1}\,a_{+2} + b_{-2}\,b_{+1} + b_{-1}\,b_{+2})\,\cos(3\,\omega_{\mathrm{m}} t) \\
&+ 2\,(a_{-2}\,a_{+2} + b_{-2}\,b_{+2})\,\cos(4\,\omega_{\mathrm{m}} t) \\
&+ 2\,\cos(\Delta_{\mathrm{F}} + \Delta_{\mathrm{M}})\,(a_{+1} + b_{-1} + a_{-1}\,b_{-2} + a_{+2}\,b_{+1} \\
&+ (1 + a_{+2} + a_{-1}\,b_{-1} + a_{+1}\,b_{-1} + b_{-2} + a_{-2}\,b_{-2} + a_{+1}\,b_{+1} + a_{+2}\,b_{+2})\,\cos(\omega_{\mathrm{m}} t) \\
&+ (a_{-1} + (a_{-2} + a_{+2})\,b_{-1} + b_{+1} + a_{+1}\,(b_{-2} + b_{+2}))\,\cos(2\,\omega_{\mathrm{m}} t) \\
&+ (a_{-2} + a_{+2}\,b_{-2} + a_{-1}\,b_{+1} + b_{+2})\,\cos(3\,\omega_{\mathrm{m}} t) \\
&+ (a_{-2}\,b_{+1} + a_{-1}\,b_{+2})\,\cos(4\,\omega_{\mathrm{m}} t) + a_{-2}\,b_{+2}\,\cos(5\,\omega_{\mathrm{m}} t)) \\
&- 2\,(1 + a_{-1}\,b_{-1} - a_{+1}\,b_{-1} + (-1 + a_{-2})\,b_{-2} + a_{+1}\,b_{+1} + a_{+2}\,(-1 + b_{+2}))\times \\
&\times \sin(\Delta_{\mathrm{F}} + \Delta_{\mathrm{M}})\,\sin(\omega_{\mathrm{m}} t) \\
&- 2\,(a_{-1} + a_{-2}\,b_{-1} - a_{+2}\,b_{-1} - a_{+1}\,b_{-2} + b_{+1} + a_{+1}\,b_{+2})\,\sin(\Delta_{\mathrm{F}} + \Delta_{\mathrm{M}})\,\sin(2\,\omega_{\mathrm{m}} t) \\
&- 2\,(a_{-2} - a_{+2}\,b_{-2} + a_{-1}\,b_{+1} + b_{+2})\,\sin(\Delta_{\mathrm{F}} + \Delta_{\mathrm{M}})\,\sin(3\,\omega_{\mathrm{m}} t) \\
&- 2\,(a_{-2}\,b_{+1} + a_{-1}\,b_{+2})\,\sin(\Delta_{\mathrm{F}} + \Delta_{\mathrm{M}})\,\sin(4\,\omega_{\mathrm{m}} t) \\
&- 2\,a_{-2}\,b_{+2}\,\sin(\Delta_{\mathrm{F}} + \Delta_{\mathrm{M}})\,\sin(5\,\omega_{\mathrm{m}} t)
\end{aligned}
\tag{7}
$$

To avoid mistakes, this and all other complicated expressions were calculated using a computer-algebra system (MATHEMATICA).

Since our SBDFT phasemeter is in effect a bandpass filter that examines only the $\omega_{\mathrm{m}} t$ compo-

nent of the photocurrent, the next step[1] is to extract all parts of this expression with a $\sin(\omega_\mathrm{m} t)$ or $\cos(\omega_\mathrm{m} t)$ time dependence:

$$\begin{aligned} &I_\mathrm{M} = (e_\mathrm{M} e_\mathrm{M}^*)|_{\omega=\omega_\mathrm{m}} = \\ &2\,((a_{-1} + a_{-1}\,a_{-2} + a_{+1} + a_{+1}\,a_{+2} + b_{-1} + b_{-1}\,b_{-2} + b_{+1} + b_{+1}\,b_{+2})\,\cos(\omega_\mathrm{m} t) \\ &+ (a_{+2} + a_{+1}\,b_{-1} + b_{-2})\,\cos(\Delta_\mathrm{F} + \Delta_\mathrm{M} - \omega_\mathrm{m} t) \\ &+ (1 + a_{-1}\,b_{-1} + a_{-2}\,b_{-2} + a_{+1}\,b_{+1} + a_{+2}\,b_{+2})\,\cos(\Delta_\mathrm{F} + \Delta_\mathrm{M} + \omega_\mathrm{m} t)) \end{aligned} \tag{8}$$

$$\begin{aligned} &I_\mathrm{R} = (e_\mathrm{R} e_\mathrm{R}^*)|_{\omega=\omega_\mathrm{m}} = \\ &2\,((a_{-1} + a_{-1}\,a_{-2} + a_{+1} + a_{+1}\,a_{+2} + b_{-1} + b_{-1}\,b_{-2} + b_{+1} + b_{+1}\,b_{+2})\,\cos(\omega_\mathrm{m} t) \\ &+ (a_{+2} + a_{+1}\,b_{-1} + b_{-2})\,\cos(\Delta_\mathrm{F} + \Delta_\mathrm{R} - \omega_\mathrm{m} t) \\ &+ (1 + a_{-1}\,b_{-1} + a_{-2}\,b_{-2} + a_{+1}\,b_{+1} + a_{+2}\,b_{+2})\,\cos(\Delta_\mathrm{F} + \Delta_\mathrm{R} + \omega_\mathrm{m} t)) \end{aligned} \tag{9}$$

This expression represents the sinusoidal component of the photocurrent at the frequency ω_m. The phasemeter measures its phase by a DFT operation. Analytically this phase measurement can be realized as follows: First, the amplitudes of the $\sin(\omega_\mathrm{m} t)$ and $\cos(\omega_\mathrm{m} t)$ components are extracted:

$$\begin{aligned} x &= \frac{1}{T}\int_0^T I(t)\cos(\omega_\mathrm{m} t)dt, \\ y &= \frac{1}{T}\int_0^T I(t)\sin(\omega_\mathrm{m} t)dt, \end{aligned} \tag{10}$$

with $T = 2\pi/\omega_\mathrm{m}$ the period of the heterodyne frequency[2]. The $\omega_\mathrm{m} t$ component of the photocurrent is represented as a complex amplitude

$$z = x + \mathrm{i}\,y. \tag{11}$$

The phase ('argument') of this complex number represents the phase that would be measured by an ideal phasemeter.

The main measurement is the phase difference φ between PDM and PDR, which mathematically can conveniently[3] be represented by the phase of the complex quotient

$$z_\mathrm{M}/z_\mathrm{R}. \tag{12}$$

This expression in the general case (all sidebands present) is far too complex to be useful. Hence the relevant special cases are examined separately.

3.1 First-order sidebands

To study the effect of a first order sideband, e.g. a_{-1}, we set

$$a_{-1} = \varepsilon\exp(-\mathrm{i}\,\gamma) \tag{13}$$

[1] Strictly speaking, this step is not necessary because the phase extraction in the next step ignores all other frequency components. Due to the complexity of the intermediate results, however, this step is often helpful to reduce the computation time.

[2] The normalization ($1/T$ or factors of $\sqrt{2}$ etc.) of x and y are irrelevant as long as they are the same for both of them since they will cancel in the next step.

[3] Taking the difference of two arctan functions is analytically more complex and practically susceptible to phase jumps of $\pm 2\pi$ radians.

where ε is the amplitude of the sideband (which will later be assumed to be small such that the results can be linearized in ε) and γ is an arbitrary phase of that sideband with respect to the carrier. All other sideband amplitude a_{-2}, a_{+1}, a_{+2}, b_{-2}, ... are set to zero.

Please note that ε represents the amplitude of the optical sideband on the light with respect to the optical carrier amplitude. See section 4 on page 21 on how electrical sidebands are converted into optical sidebands in an AOM.

The calculation then proceeds as described above. For this example, we find

$$z_{\mathrm{M}}/z_{\mathrm{R}} = \frac{\cos(\Delta_{\mathrm{F}}+\Delta_{\mathrm{M}}) + \varepsilon\cos\gamma - \mathrm{i}\,(\sin(\Delta_{\mathrm{F}}+\Delta_{\mathrm{M}}) + \varepsilon\sin\gamma)}{\cos(\Delta_{\mathrm{F}}+\Delta_{\mathrm{R}}) + \varepsilon\cos\gamma - \mathrm{i}\,(\sin(\Delta_{\mathrm{F}}+\Delta_{\mathrm{R}}) + \varepsilon\sin\gamma)} \tag{14}$$

The phase error due to the sideband is the phase difference between $z_{\mathrm{M}}/z_{\mathrm{R}}$ and that same quantity for the case that all sidebands are zero. It is represented as a near-unity vector

$$\frac{z_{\mathrm{M}}/z_{\mathrm{R}}}{z_{\mathrm{M}}/z_{\mathrm{R}}|_{\mathrm{sidebands}=0}}. \tag{15}$$

Finally, the phase error is the angle of this vector. At this point we make use of the assumption $\varepsilon \ll 1$ and are hence allowed to approximate the angle of this near-unity vector by its imaginary part[4]. For this example (single a_{-1} sideband), the result is

$$\begin{aligned}
\frac{\delta\varphi}{\varepsilon} &= \sin(\Delta_{\mathrm{F}}+\Delta_{\mathrm{M}}-\gamma) - \sin(\Delta_{\mathrm{F}}+\Delta_{\mathrm{R}}-\gamma) \\
&= \sin(\varphi_M-\gamma) - \sin(\varphi_R-\gamma) \\
&= 2\cos\left(\Delta_{\mathrm{F}} + \frac{\Delta_{\mathrm{M}}+\Delta_{\mathrm{R}}}{2} - \gamma\right)\cdot\sin\left(\frac{\Delta_{\mathrm{M}}-\Delta_{\mathrm{R}}}{2}\right) \\
&= 2\cos\left(\frac{\varphi_{\mathrm{M}}+\varphi_{\mathrm{R}}}{2} - \gamma\right)\cdot\sin\left(\frac{\varphi_{\mathrm{M}}-\varphi_{\mathrm{R}}}{2}\right).
\end{aligned} \tag{16}$$

The corresponding result for the a_{+1} sideband is:

$$\begin{aligned}
\frac{\delta\varphi}{\varepsilon} &= \sin(\varphi_M+\gamma) - \sin(\varphi_R+\gamma) \\
&= 2\cos\left(\Delta_{\mathrm{F}} + \frac{\Delta_{\mathrm{M}}+\Delta_{\mathrm{R}}}{2} + \gamma\right)\cdot\sin\left(\frac{\Delta_{\mathrm{M}}-\Delta_{\mathrm{R}}}{2}\right) \\
&= 2\cos\left(\frac{\varphi_{\mathrm{M}}+\varphi_{\mathrm{R}}}{2} + \gamma\right)\cdot\sin\left(\frac{\varphi_{\mathrm{M}}-\varphi_{\mathrm{R}}}{2}\right).
\end{aligned} \tag{17}$$

The results for the b_{-1} and b_{+1} sidebands are identical to those for the a_{-1} and a_{+1} sidebands, respectively.

Written in the form of Equation 17, the error term consists of two factors: The first one varies rapidly as $\cos(\Delta_{\mathrm{F}})$. It is multiplied by a slowly varying factor that depends on the current operating point of the interferometer. This is in accordance with the observations as shown e.g. in Figure 29 on page 43.

These error terms correspond to the beatnotes labelled 'B' in Figure 5 on page 16. The phase error due to **all first-order sidebands** can be written in general form as

$$\delta\varphi = \left\{\alpha_1\sin\left(\frac{\varphi_{\mathrm{M}}+\varphi_{\mathrm{R}}}{2}\right) + \alpha_2\cos\left(\frac{\varphi_{\mathrm{M}}+\varphi_{\mathrm{R}}}{2}\right)\right\}\cdot\sin\left(\frac{\varphi_{\mathrm{M}}-\varphi_{\mathrm{R}}}{2}\right) \tag{18}$$

[4] A unity vector with a small perturbation $1+\delta\exp(\mathrm{i}\,\alpha)$ has the angle $\arctan(\delta\sin\alpha/(1+\delta\cos\alpha))$, and the first term in the Taylor expansion around $\delta=0$ is $\delta\sin\alpha$, i.e. the imaginary part of the perturbation.

where the constants α_1 and α_2 are combinations of the amplitudes ε and phases γ of the individual first-order sidebands.

3.2 Amplitude- and phase-modulation

Particular combinations of first-order sidebands appear when a beam carries *amplitude modulation* or *phase-/frequency- modulation*. These will now be considered, using the formulae from Appendix A on page 92.

Amplitude modulation (AM) at the heterodyne frequency f_{het} on one beam can be described as a set of sidebands around the carrier with

$$\begin{aligned} a_{-1} &= m/2, \\ a_{+1} &= m/2, \end{aligned} \tag{19}$$

where m is the modulation index (Equation 79 on page 95). Alternatively, the other quadrature of the modulation can be described by

$$\begin{aligned} a_{-1} &= \mathrm{i}\, m/2, \\ a_{+1} &= -\mathrm{i}\, m/2. \end{aligned} \tag{20}$$

(Equation 80 on page 95.) The resulting total phase error for these two cases is

$$\begin{aligned} (79): &\quad \delta\varphi = m\,(\sin(\varphi_{\mathrm{M}}) - \sin(\varphi_{\mathrm{R}})), \\ (80): &\quad \delta\varphi = m\,(\cos(\varphi_{\mathrm{M}}) - \cos(\varphi_{\mathrm{R}})), \end{aligned} \tag{21}$$

The general case is given by Equation 81 on page 95:

$$\begin{aligned} a_{-1} &= \frac{m}{2}\exp(-\mathrm{i}\,\gamma), \\ a_{+1} &= \frac{m}{2}\exp(\mathrm{i}\,\gamma), \end{aligned} \tag{22}$$

and yields an error term of the form

$$\begin{aligned} \delta\varphi &= m\,(\sin(\varphi_{\mathrm{M}} - \gamma) - \sin(\varphi_{\mathrm{R}} - \gamma)) \\ &= 2m\cos\left(\frac{\varphi_{\mathrm{M}} + \varphi_{\mathrm{R}}}{2} - \gamma\right) \cdot \sin\left(\frac{\varphi_{\mathrm{M}} - \varphi_{\mathrm{R}}}{2}\right). \end{aligned} \tag{23}$$

Exactly the same results are obtained when the AM is applied to the second beam instead of the first beam; and consequently the result is double when the same AM is synchronuously applied to both beams.

Phase modulation (PM) with a small modulation index on one beam at the heterodyne frequency f_{het}, on the other hand, can be described as a set of sidebands around the carrier with

$$\begin{aligned} a_{-1} &= -m/2, \\ a_{+1} &= m/2, \end{aligned} \tag{24}$$

where m is the modulation index (Equation 76 on page 94). Alternatively, the other quadrature of the modulation can be described by

$$\begin{aligned} a_{-1} &= \mathrm{i}\, m/2, \\ a_{+1} &= \mathrm{i}\, m/2. \end{aligned} \tag{25}$$

(Equation 78 on page 94.) The resulting total phase error for these two cases (and consequently also for a linear combination describing weak PM with arbitrary phase) is

$$\delta\varphi = 0. \tag{26}$$

Note that phase modulation also produces higher order sidebands in addition to the first-order sidebands. The effect of the second-order sidebands will be examined in the next section, while sidebands of order three and above cause no phase error.

3.3 Second-order sidebands

For the second-order sidebands, we proceed in a similar fashion, e.g. by setting

$$a_{-2} = \varepsilon \exp(-\mathrm{i}\,\gamma) \tag{27}$$

and all other sidebands to zero. The resulting phase error for each of the second-order sidebands is:

$$\begin{aligned}
a_{-2}: \quad & \frac{\delta\varphi}{\varepsilon} = 0, \\
a_{+2}: \quad & \frac{\delta\varphi}{\varepsilon} = 2\cos(2\Delta_F + \Delta_R + \Delta_M + \gamma)\sin(\Delta_M - \Delta_R) \qquad (28)\\
& \quad = 2\cos(\varphi_\mathrm{M} + \varphi_\mathrm{R} + \gamma))\sin(\varphi_M - \varphi_R), \\
b_{-2}: \quad & \frac{\delta\varphi}{\varepsilon} = 2\cos(2\Delta_F + \Delta_R + \Delta_M - \gamma)\sin(\Delta_M - \Delta_R) \qquad (29)\\
& \quad = 2\cos(\varphi_\mathrm{M} + \varphi_\mathrm{R} - \gamma))\sin(\varphi_M - \varphi_R), \\
b_{+2}: \quad & \frac{\delta\varphi}{\varepsilon} = 0. \qquad (30)
\end{aligned}$$

This result has a number of interesting features. These error terms correspond to the beatnotes labelled 'C' in Figure 5 on page 16, and it is hence immediately clear why a_{-2} and b_{+2} have no effect. Correspondingly, AM or PM/FM at $2\omega_\mathrm{het}$ has no special features as opposed to the ω_het case above, since only one single sideband on each beam is effective.

The dependence on Δ_F of these error terms is given by $\cos(2\Delta_F + \Delta_R + \Delta_M \pm \gamma)$, which shows that they finally can explain the $\cos(2\Delta_F)$ type sidebands (Figure 4 on page 15).

A less precise but more intuitive explanation is: When Δ_F changes by a certain amount, this corresponds to a shift of all frequencies in one laser beam by that amount. In Figure 5 on page 16, this would mean e.g. a right-shift of the upper comb of frequencies. The effect on the beatnotes is as follows: The main signal 'A' gets 'longer' by Δ_F. i.e. its phase changes by $+\Delta_F$. The beatnotes caused by first-order sidebands ('B') remain unchanged, and those caused by the second-order sidebands ('C') get 'shorter', i.e. their phase changes by $-\Delta_F$. The important observation now is that by using the reference interferometer, which undergoes the same changes due to Δ_F, we effectively refer all phases to the main signal 'A'. With respect to that signal, the sideband beatnotes 'B' change by $-\Delta_F$, whereas those caused by the second-order sidebands ('C') change by $-2\Delta_F$. We have produced an animated GIF file (`sidebandsmove.gif`) that illustrates this behaviour and that is distributed together with this technical note.

Finally, the error term is proportional to $\sin(\varphi_M - \varphi_R)$ which means that it should vanish when $\varphi_M - \varphi_R = \pm k\,\pi$, i.e. when the phasors of φ_M and φ_R are parallel or antiparallel, a feature that had been experimentally observed before this theoretical explanation was found (see also Figure 30 on page 44 for an experimental demonstration).

The phase error due to the **second-order sidebands** can be written in general form as

$$\alpha_3 \sin(\underbrace{\varphi_\mathrm{M} + \varphi_\mathrm{R}}_{=2\Delta_F+\Delta_R+\Delta_M}) \sin(\varphi_\mathrm{M} - \varphi_\mathrm{R}) + \alpha_4 \cos(\varphi_\mathrm{M} + \varphi_\mathrm{R}) \sin(\varphi_\mathrm{M} - \varphi_\mathrm{R}). \tag{31}$$

3.4 Magnitude and scaling of error terms

All non-zero results in the previous sections 3.1 ... 3.3 have approximately the same order of magnitude and the same scaling behaviour. As an example, we look at the first-order sideband a_{-1} for which we had found

$$\frac{\delta\varphi}{\varepsilon} = 2\cos\left(\Delta_\mathrm{F} + \frac{\Delta_\mathrm{M} + \Delta_\mathrm{R}}{2} - \gamma\right) \cdot \sin\left(\frac{\Delta_\mathrm{M} - \Delta_\mathrm{R}}{2}\right) \tag{32}$$

In the worst case, $\Delta_\mathrm{R} = \Delta_\mathrm{M} + \pi$ and hence

$$\delta\varphi = 2\varepsilon \sin(\Delta_\mathrm{F} + \Delta_\mathrm{M} - \gamma). \tag{33}$$

This represents an error which is periodic with Δ_F and which has a peak-peak amplitude of 4ε. Having set the carrier amplitude to unity, ε represents the sideband amplitude with respect to the carrier, which is often expressed in dBc. For example, $-60\,\mathrm{dBc}$ is equivalent to $\varepsilon = 10^{-3}$ and a peak-peak phase error of $4 \cdot 10^{-3}\,\mathrm{rad}$.

Please note that ε represents the amplitude of the optical sideband on the light with respect to the optical carrier frequency. See Section 4 on how electrical sidebands are converted into optical sidebands in an AOM.

Maybe the most important consequence of these results is that the error term scales with the *amplitude* of the offending sideband, not with its power. This means that a reduction of the error (expressed in radian) by a factor of 10 requires a reduction of the sideband by a factor of 10 in amplitude, i.e. by 20 dB, *not* 10 dB. This is true for all sideband-induced errors. Fundamentally it is caused by the fact that the error results as interference product between the small offending sideband and a large carrier, and is as such proportional to the product of the two amplitudes, one of which (the carrier) is large and constant.

Because of the important consequences of this scaling behaviour, we have conducted a series of measurements to verify it (see Section 6.2.2 on page 41 and Figure 35 on page 47).

4 Conversion of electrical sidebands into optical sidebands in the AOM

The theoretical analysis in Section 3 on page 14 starts from a certain ratio ε of sideband amplitude to carrier amplitude *in the light*. For clarity, this ratio will sometimes also be called ε_opt in this Section.

The most prominent way to produce these sidebands is via *electrical* sidebands in the RF signal that drives the AOM. The ratio of sideband amplitude to carrier amplitude in these electrical signals is called ε_el. This section investigates experimentally the relationship of ε_opt to ε_el and its dependence on the AOM drive levels.

While ε_el can be directly measured with an RF spectrum analyzer in the electrical drive signal ($\varepsilon_\mathrm{el} = 10^{\mathrm{dBc}/20}$), ε_opt must be measured in the light emerging from the AOM. This can be done as follows:

For the case of a single sideband, we have the total optical amplitude

$$a = \exp(\mathrm{i}\,\omega_0 t) + \varepsilon_{\mathrm{opt}} \exp(\mathrm{i}\,(\omega_0 + \Delta\omega)t), \tag{34}$$

which on a photodiode produces a photocurrent proportional to

$$|a|^2 = 1 + 2\varepsilon_{\mathrm{opt}} \cos(\Delta\omega t) + \varepsilon_{\mathrm{opt}}^2 \approx 1 + 2\varepsilon_{\mathrm{opt}} \cos(\Delta\omega t). \tag{35}$$

By measuring the ratio of the DC photocurrent to the $\Delta\omega$ component in the photocurrent, we can thus directly measure $\varepsilon_{\mathrm{opt}}$:

$$\varepsilon_{\mathrm{opt}} = \frac{I_{\mathrm{pk}}(\Delta\omega)}{2\,I_{\mathrm{DC}}} = \frac{I_{\mathrm{pk-pk}}(\Delta\omega)}{4\,I_{\mathrm{DC}}} = \frac{I_{\mathrm{rms}}(\Delta\omega)}{\sqrt{2}\,I_{\mathrm{DC}}}. \tag{36}$$

4.1 Observations using a stable interferometer

This part of the investigation was undertaken in Glasgow to establish how the level of spurious heterodyne frequency signal (arising from the two frequencies of light having been mixed at the photodiode) varies with the level of drive frequency signals.

It was found that the level of spurious signal varies linearly with the sideband amplitude over a wide range of sideband amplitudes. The relative magnitude of the optical sideband w.r.t. the carrier (called ε throughout this report and for clarity $\varepsilon_{\mathrm{opt}}$ in this section) is somewhere between 0.1 and 1.0 of the same ratio in the electrical drive signal (which will be called $\varepsilon_{\mathrm{el}}$ in this section), depending on the RF drive power.

The set up for the monolithic optical bench (OB) stability tests at Glasgow comprised of one laser (Nd:YAG NPRO laser operating at 1064 nm) that was split and directed through two individual acousto-optic modulators (AOMs). One AOM was driven at 80 MHz and the other at 80.01 MHz. The AOMs were aligned so as to deliver most of the light into the first order. This was in order to generate a beatnote at a convenient frequency (∼kHz) upon beam recombination. These beams were sent through fibres and onto the OB where they were split and recombined in three places, making three Mach-Zender interferometers. The recombined beams left the OB and were measured using single element silicon photodiodes.

The detailed setup of the interferometer and the results obtained can be found in references [12] and [13].

When one beam was blocked before travelling through an AOM, a small amount of signal at 10 kHz (the heterodyne frequency) was detected at the photodiode, suggesting that both 80 and 80.01 MHz signals were present at the photodiode. This 10 kHz signal was not present when the second beam was blocked, eliminating direct electrical RF pick-up as the source. The mechanism for a signal at the heterodyne frequency appearing at the photodiode under these circumstances is the mixing of light beams shifted in frequency from the original by the two drive frequencies.

The level of RF drive to the AOMs was of order 1.5 W, which was provided by using signal generators and power amplifiers. While much care was taken to avoid pick-up between the two transmission lines, an RF isolation factor of 120 dB would be necessary to reduce the pickup to insignificant levels. It is very difficult to achieve this level of isolation in a compact experimental arrangement.

4.2 Dependence on sideband amplitude

A separate experiment was set up to investigate the dependence on sideband amplitude.

The apparatus was set up as shown in Figure 6. A Nd:YAG NPRO laser operating at 1064 nm was directed through a single AOM and the beam was incident on a single element silicon photodiode. All tests described in this Section were done using AOMs from Isomet, model 1205C-2. Some of the laser beam was also directed into a Fabry-Perot scanning cavity (not shown) to ensure the laser was running single mode for all measurements.

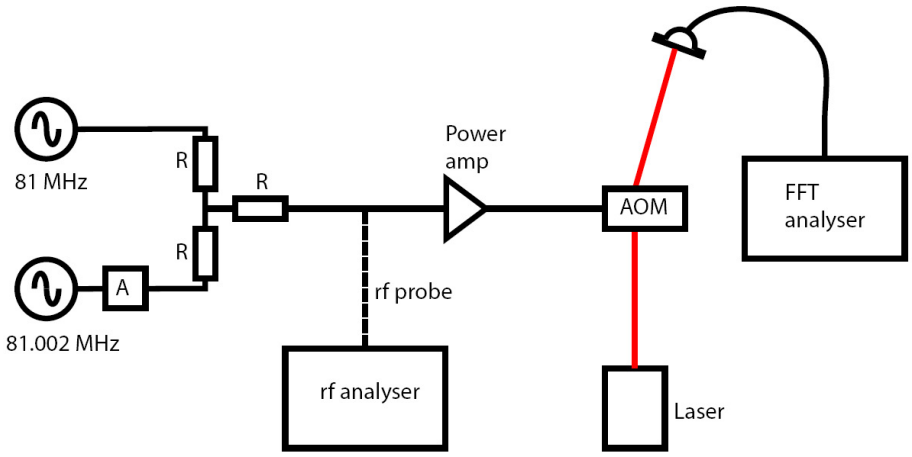

Figure 6: Overview of the test setup for the AOM conversion measurements in Glasgow.

The AOM drive was from two signal generators, combined using a resistive network, and power amplifier. A high frequency probe attached to a spectrum analyser was used immediately before the power amplifier to measure the absolute and relative levels of the signals from the two generators. The output of the photodiode was connected to either an oscilloscope (for DC light level measurements) or FFT analyser (to measure the amplitude of the 2 kHz signal).

The aim was to drive the AOM with two frequencies (whose amplitude could be varied) and measure the beatnote level from the photodiode under varying conditions. The drive frequency for the AOM was 81 MHz with the second drive frequency being 2 kHz away at 81.002 MHz. These values were chosen for the spectral purity of the generators and as a heterodyne frequency of the order of 2 kHz is expected for LISA Pathfinder.

Data was taken showing that the actual drive to the AOM (after the power amplifier) was linear as the signal generator output level was increased over the entire range that readings were taken.

Figure 7 on the next page shows the DC light level at the photodiode as a function of RF drive (the power amplifier adds $\sim$ 35 dB to this). This shows how the optical power level in the diffracted beam varies non-linearly with applied RF power.

Figure 8 on the following page shows the size of the 2 kHz signal from the photodiode against the difference in signal size of the drive frequencies for three different carrier levels.

The data show a linear relationship between electrical sideband amplitude and optical sideband amplitude over a wide range of sideband amplitudes. They were fitted with a linear model (using the data expressed in dB). The results were:

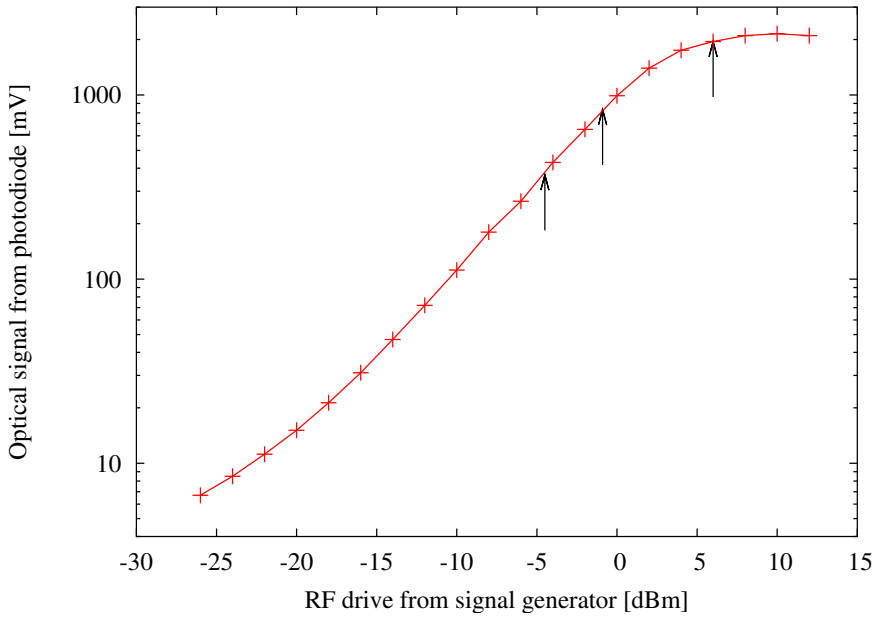

Figure 7: DC light level at photodiode as a function of RF drive from signal generator. The vertical arrows indicate the three power levels that were used in the measurements shown in Figure 8.

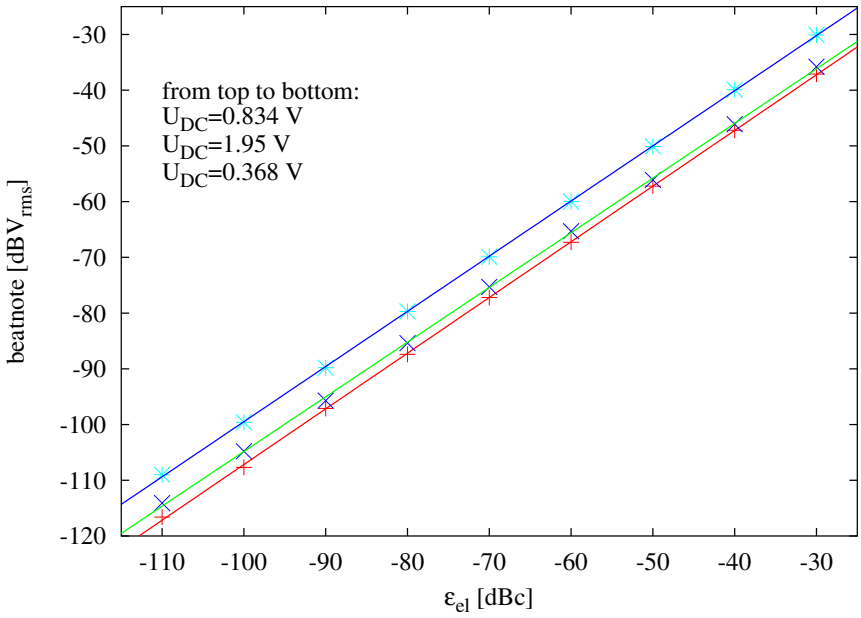

Figure 8: Magnitude of 2 kHz signal as a function of 81.002 MHz amplitude with respect to 81 MHz amplitude. Points are experimental data, solid lines are fits.

U_{DC} [V]	slope	intercept [$\mathrm{dBV_{rms}}$]	$\varepsilon_{\mathrm{opt}}/\varepsilon_{\mathrm{el}}$
0.368	0.999	-7.27	0.832
0.834	0.990	-0.51	0.799
1.95	0.981	-6.73	0.167

Note that for the highest DC power level, the coupling factor $\varepsilon_{\mathrm{opt}}/\varepsilon_{\mathrm{el}}$ is lower than for the other two measurements. It can be seen in Figure 8 on the previous page that this measurement was taken at a point where the slope efficiency of the AOM is lower than for the other two measurements so this lower coupling factor is to be expected.

4.3 Dependence on carrier level

After these results indicated a dependence of the coupling efficiency on the carrier power, we performed another series of measurements in Hannover to investigate this dependency. Using a setup similar to Figure 6 on page 23 (see also Section 5 on page 27 for a general description of the setup in Hannover, in particular Sections 5.4 and 5.5), we obtained results listed in Table 1.

electrical					optical				interferometer	
offset	P_{c}	P_{sb}	$P_{\mathrm{sb}}/P_{\mathrm{c}}$	$\varepsilon_{\mathrm{el}}$	U_{c}	U_{sb}	$\varepsilon_{\mathrm{opt}}$	$\varepsilon_{\mathrm{opt}}/\varepsilon_{\mathrm{el}}$	$\delta\varphi$	φ
	[dBm]	[dBm]	[dBc]		[$\mathrm{mV_{DC}}$]	[$\mathrm{mV_{pp}}$]			[$\mathrm{mrad_{pp}}$]	rad
f_{het}	32.3	−8.7	−41.0	0.0089	800	14.2	.0044	0.494	19.2	$0.940\,\pi$
f_{het}	31.7	−8.7	−40.4	0.0095	700	14.4	.0051	0.537	22.3	$0.931\,\pi$
f_{het}	31.5	−8.7	−40.2	0.0098	600	13.2	.0055	0.561	22.4	$0.928\,\pi$
f_{het}	30.7	−8.8	−39.5	0.0106	500	13.0	.0065	0.613	28.9	$0.923\,\pi$
f_{het}	29.5	−8.8	−38.3	0.0122	370	12.1	.0081	0.664	35.8	$0.912\,\pi$
f_{het}	28.6	−8.8	−37.4	0.0135	280	11.3	.0101	0.748	43.3	$0.911\,\pi$
f_{het}	24.4	−8.8	−33.2	0.0219	120	9.1	.0190	0.867	82.0	$0.910\,\pi$
$2f_{\mathrm{het}}$	32.3	−8.7	−41.0	0.0089	730	13.1	.0045	0.506	26.5	$0.477\,\pi$
$2f_{\mathrm{het}}$	31.8	−8.7	−40.5	0.0094	640	13.3	.0052	0.553	28.8	$0.475\,\pi$
$2f_{\mathrm{het}}$	30.8	−8.8	−39.6	0.0105	500	13.1	.0066	0.628	33.2	$0.476\,\pi$
$2f_{\mathrm{het}}$	30.2	−8.7	−38.9	0.0114	440	13.0	.0074	0.649	35.4	$0.489\,\pi$
$2f_{\mathrm{het}}$	29.2	−8.8	−38.0	0.0126	360	12.7	.0088	0.698	42.1	$0.492\,\pi$
$2f_{\mathrm{het}}$	28.2	−8.8	−37.0	0.0141	300	12.7	.0106	0.752	46.9	$0.493\,\pi$
$2f_{\mathrm{het}}$	26.8	−8.8	−35.6	0.0164	220	11.8	.0134	0.817	57.6	$0.488\,\pi$
$2f_{\mathrm{het}}$	25.7	−8.8	−34.5	0.0188	190	11.9	.0157	0.835	62.9	$0.486\,\pi$
$2f_{\mathrm{het}}$	24.9	−8.8	−33.7	0.0207	130	8.9	.0171	0.826	72.6	$0.483\,\pi$
$2f_{\mathrm{het}}$	23.9	−8.8	−32.7	0.0232	100	8.0	.0200	0.862	84.3	$0.481\,\pi$
$2f_{\mathrm{het}}$	22.0	−8.8	−30.8	0.0288	80	7.8	.0244	0.847	106.6	$0.481\,\pi$
$2f_{\mathrm{het}}$	20.7	−8.8	−29.5	0.0335	50	5.5	.0275	0.821	121.1	$0.482\,\pi$

Table 1: Results of single sideband injection experiments in Hannover.

The results for $\varepsilon_{\mathrm{opt}}/\varepsilon_{\mathrm{el}}$ are plotted in Figure 9 on the next page. They show a conversion efficiency $\varepsilon_{\mathrm{opt}}/\varepsilon_{\mathrm{el}}$ of $0.8 \ldots 0.9$ for small carrier powers which decreases to ≈ 0.5 for those power levels near saturation that are typically used.

The interferometric results are discussed in Section 6.2.2 on page 41.

In the context of measuring the effect of amplitude modulation on the interferometer, similar

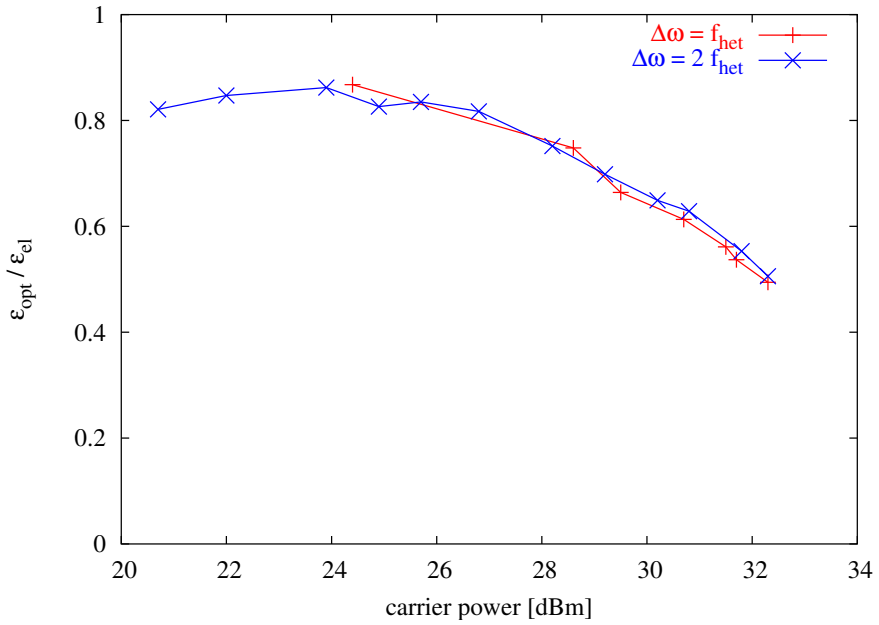

Figure 9: Dependence of the coupling efficieny $\varepsilon/\varepsilon_{\mathrm{el}}$ on the carrier power.

measurements were also done for the case of amplitude modulation (see Section 6.3 on page 47). There a ratio $m_{\mathrm{opt}}/m_{\mathrm{el}} = \varepsilon_{\mathrm{opt}}/\varepsilon_{\mathrm{el}}$ of ≈ 0.44 was found for +32.8 dBm carrier level, in accordance with the results shown here.

4.4 Summary of coupling results

From the measurements described above it follows that:

- For sidebands that are considerably smaller than the carrier, an AOM linearly converts electrical sidebands into optical sidebands, i.e. reducing the electrical sideband by a factor of 10 in amplitude results in an optical sideband that is also a factor of 10 smaller in amplitude.
- The ratio of sideband amplitude to carrier amplitude (called ε) is *not exactly* equal in the electrical signals and the optical signals. For all our measurements, we found $\varepsilon_{\mathrm{opt}}/\varepsilon_{\mathrm{el}} \lessapprox 1$, with the ratio approaching 1.0 for small carrier powers and getting smaller for those higher carrier powers that approach saturation of the AOM efficiency. Since typically the AOM will be operated in the latter regime, the ratio $\varepsilon_{\mathrm{opt}}/\varepsilon_{\mathrm{el}}$ in practice is expected to be somewhere between 0.4 and 0.8.
- Practically this poses no problem, since the sideband requirements for the AOMU have been written referring to the optical sidebands. If the same requirements are met for the electrical sidebands, the optical sidebands will hence be a little smaller than required and thus on the safe side.

5 Test equipment

In this section, the most important equipment that was used during the experiments in Hannover is described.

5.1 Interferometer

We have used the engineering model (EM) of the LTP optical bench (OB) for the experiments. A general description of the interferometer is given in References [9], [10], [11] and [6]. Figure 10 shows the optical paths, and Figure 11 on the next page shows a picture of the interferometer in the vacuum tank in Hannover.

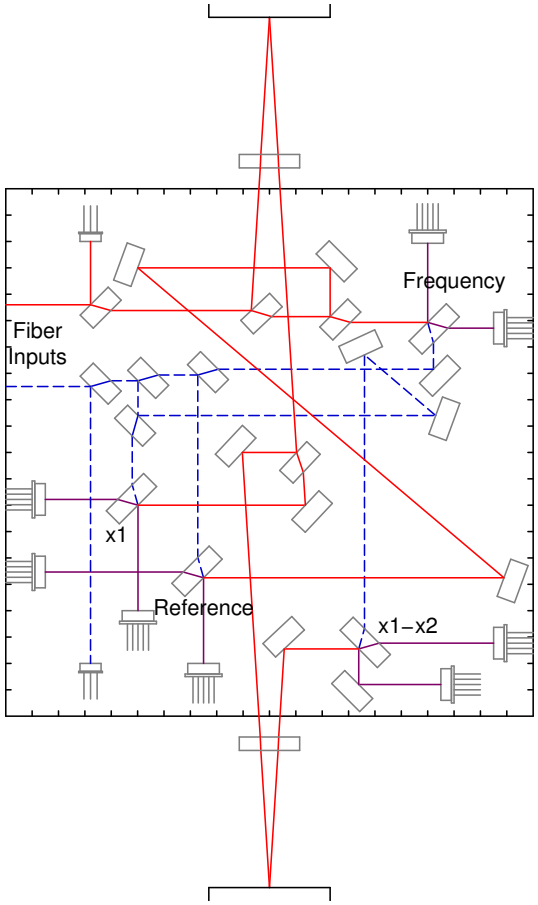

Figure 10: The optical paths in the interferometer.

For later reference, Figures 12 on page 29 and 13 on page 30 show the individual optical paths in each of the four interferometers.

5.2 Vacuum system

The vacuum system consists of the following components:

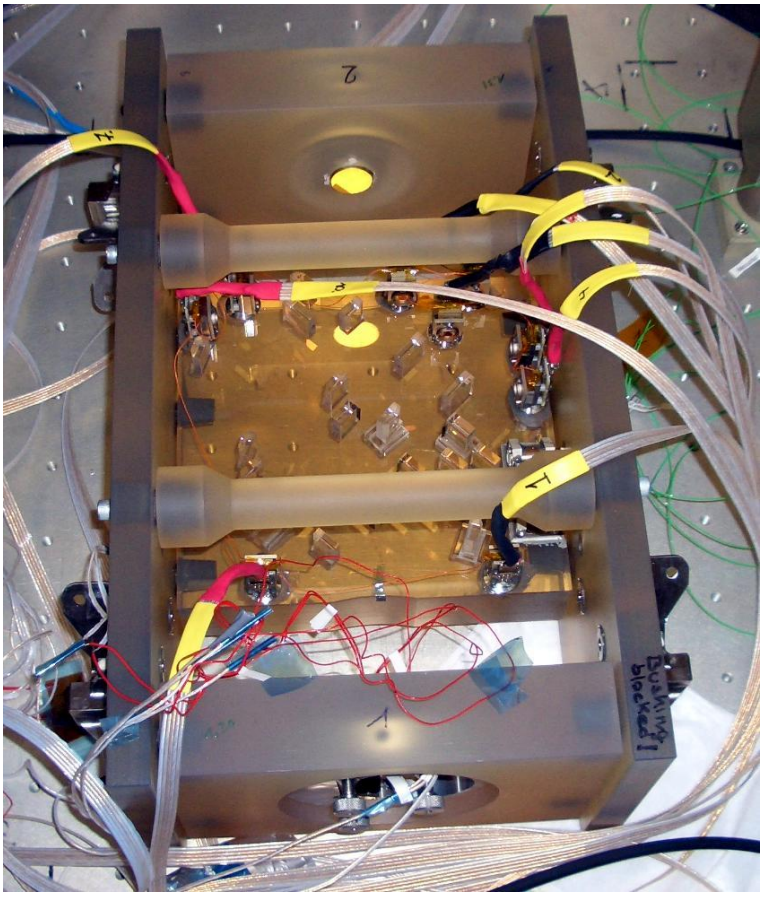

Figure 11: Picture of the optical bench in the vacuum tank in Hannover.

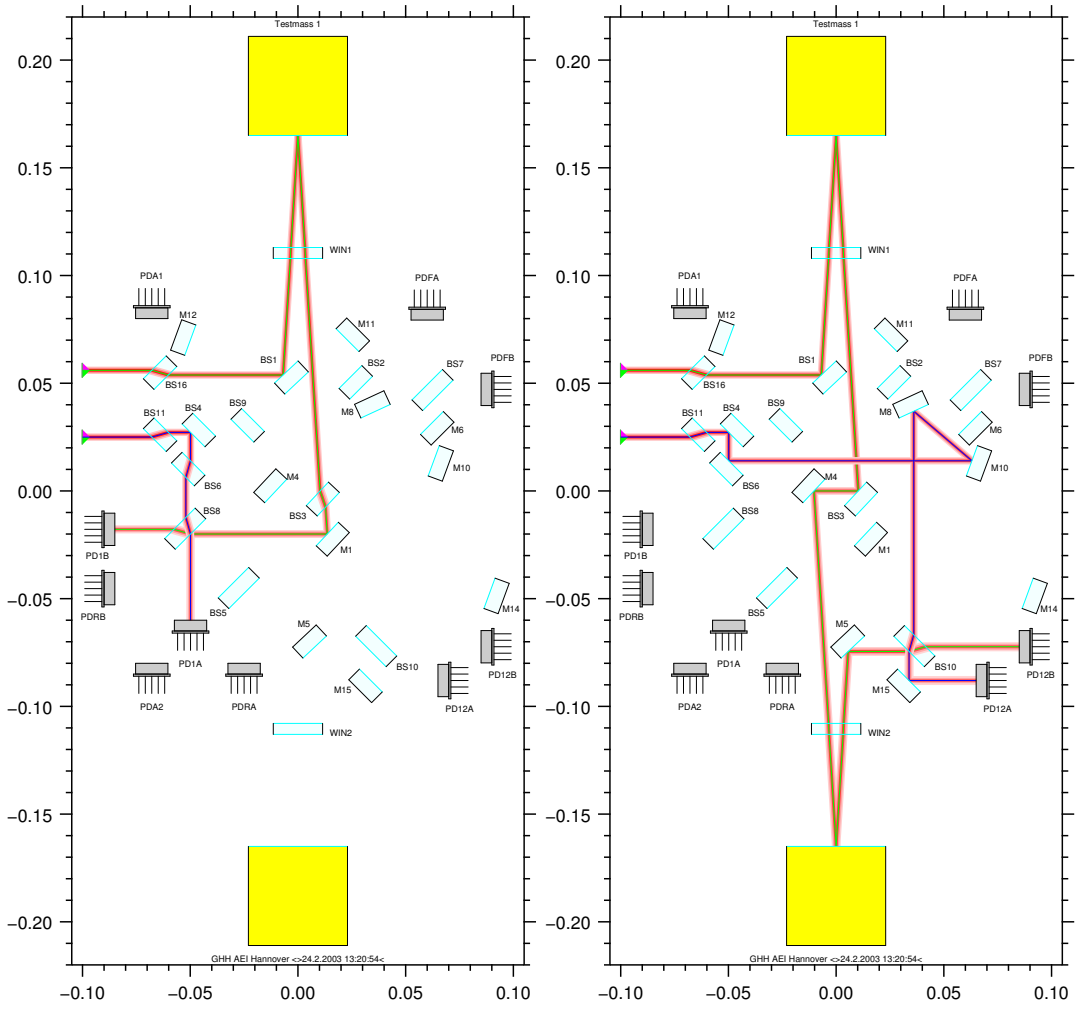

Figure 12: Optical paths of the 'x_1' and '$x_1 - x_2$' interferometers. The pathlength differences between both beams are zero, when an extra pathlength of 356.7 mm in the reference fiber is included.

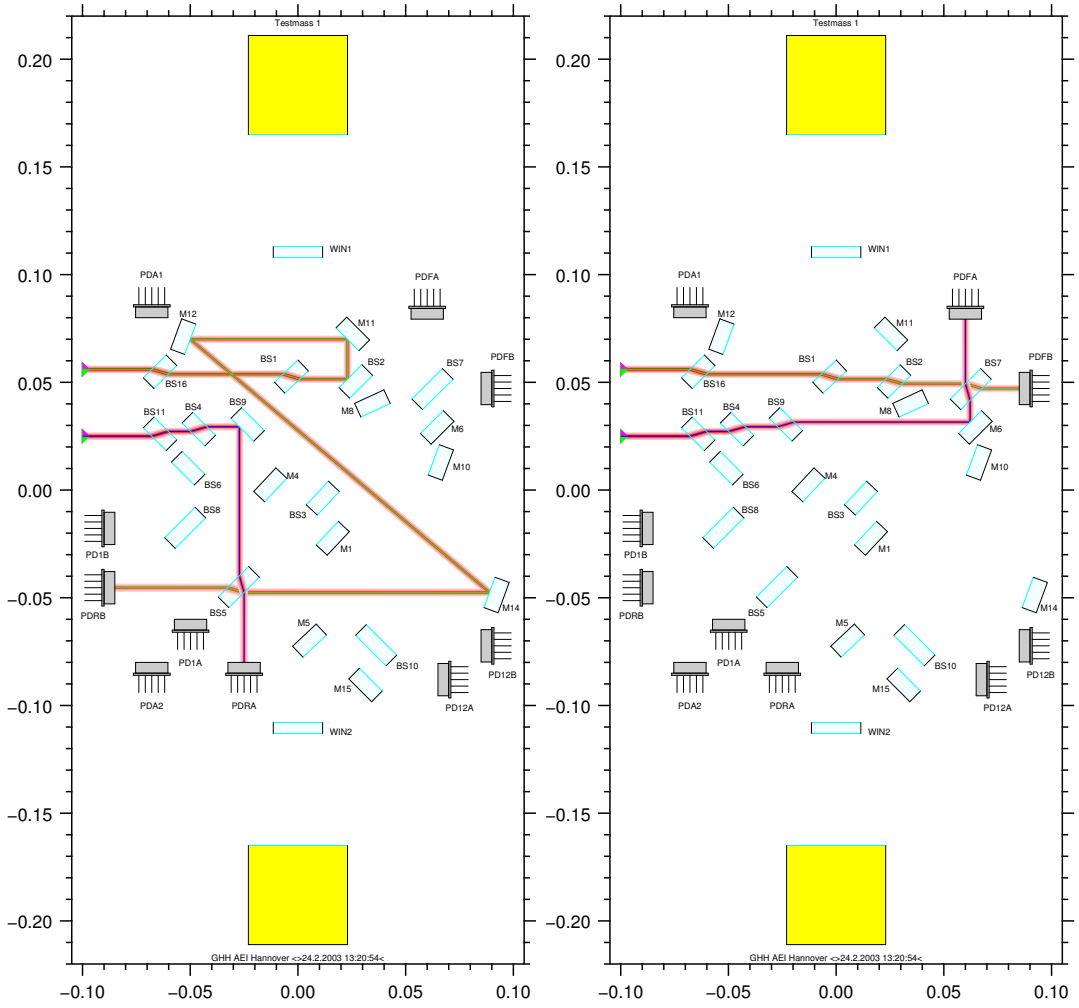

Figure 13: Optical paths of the reference and 'frequency' interferometers. The pathlength differences between both beams are zero in the reference interferometer (left), when an extra pathlength of 356.7 mm in the reference fiber is included. The pathlength difference in the 'frequency' interferometer (right) is then 380 mm.

Component	Manufacturer	Specifications
Scroll Pump	Franklin Electric	Mod.1301007453. Power: 3/4 hp
Turbo Pump	Pfeiffer	Typ. TPH170. Volume flow rate: 170 l/s
Vacuum Sensor	Leybold Vakuum GmbH	Typ. ITR90, Nr.12094. Pressure Range: $5 \times 10^{-10} - 1000$ mbar
Vacuum Tank	not specified	Volume (approx.): 950 l

The optical bench is located inside a cylindrical vacuum tank. On the bottom plate there are two fiber-optical feedthroughs (Schäfter-Kirchhoff) and about 100 electrical feedthroughs. Both vacuum pumps are connected in series. The minimum pressure normally reached after evacuating the tank is approx. 3×10^{-5} mbar. For an over-night performance measurement, both pumps are turned off after evacuating the tank, in order to avoid vibrations that could couple into the control loops due to acoustics (e.g. free-beam modulation bench outside the tank). Therefore, the typical value of the pressure during a performance measurement is approx. 10^{-3} mbar.

5.3 Laser

Initially we used both a prototype of a space-qualified laser from Tesat laser (Figure 14) and an Innolight Mephisto 500. Both are diode-pumped monolithic Nd:YAG lasers operating in the near-Infrared (≈ 1064 nm). While the Tesat laser delivers 25 mW at the end of an optical fiber, the Innolight laser delivers up to 500 mW as a free beam that needs separate fiber coupling. The measured frequency noise of the Tesat laser is shown in Figure 78. While we have not measured the frequency noise of the Innolight laser, other experiments have shown that it is comparable. The results of early tests did not depend on which laser was used, and they could both be used interchangeably. In the latest tests we have only used the Innolight laser.

The frequency stabilization uses the auxiliary PDF interferometer and an analog servo with a unity-gain frequency of a few Hz and is described in [6] and Section 12 on page 84.

The laser power was also stabilized in the most recent experiments (see Section 11 on page 81.

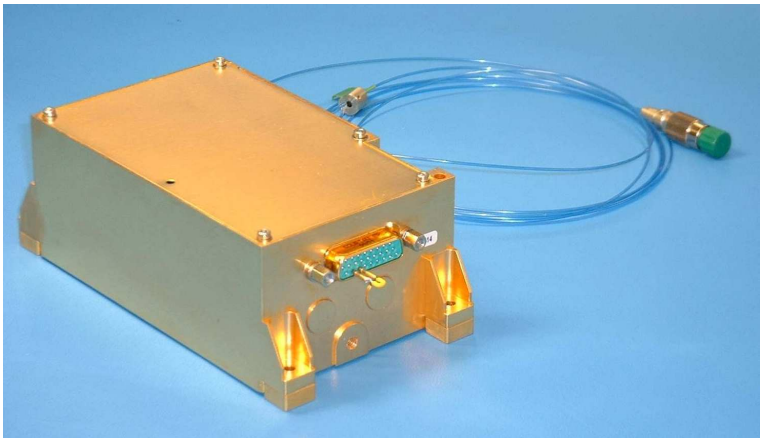

Figure 14: The Tesat laser head.

5.4 Acousto-optical modulators (AOMs)

We used both the Contraves modulation bench (Figure 15) and a free-beam modulation unit assembled from discrete optical components (Figure 16 on the following page). While the Contraves modulation bench is more compact, the discrete free-beam setup has better efficiency and more flexibility. In particular, the OPD stabilization using a PZT between beamsplitter and one of the AOMs could only be implemented with the free-beam setup. Otherwise, the two modulation units could be used interchangeably. We have used the free-beam setup for most of the tests.

The free-beam AOMs are 2 mm aperture models from Isomet (1205C-2) operating nominally at 80 MHz and 2 Watt RF power.

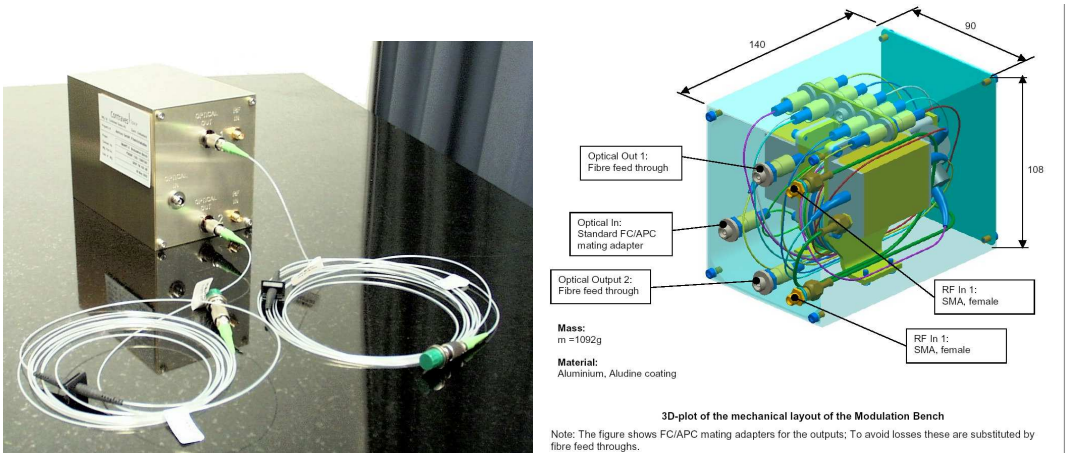

Figure 15: The Contraves modulation bench.

5.5 AOM driving electronics

We used the prototype AOM driving electronics that were developed and built by AEI during the preinvestigations for all tests. Figure 17 on the next page shows a block diagram of the frequency synthesizers, and Figure 18 on page 34 shows the phase noise measured with one such system, which is smaller than $10^{-6}\,\mathrm{rad}/\sqrt{\mathrm{Hz}}$ at 1 kHz. Note that this measurement was done with 2 VCXOs locked to the same frequency. See Section 8 on page 52 for results with different frequencies.

Each power amplifier is built around a Mitsubishi RF power module M67743L (68-81 MHz, 7 Watt maximum output), which is supplied with specially regulated low-noise supply voltages of 5.0 V and 12.5 V. Since it turned out that these amplifiers play an important role in the generation of the sidebands, the datasheet is reproduced in Appendix D on page 104.

Figure 19 on page 35 shows a block diagram of the power amplifier and amplitude control and the RF amplitude noise measured with this system, which is smaller than $\approx 10^{-8}/\sqrt{\mathrm{Hz}}$ at 1 kHz. Figure 20 on page 36 shows a circuit diagram of the relevant parts.

A sample of the RF output power is obtained with a 20 dB directional coupler (model PDC20-3 from Minicircuits), bandpass filtered and rectified with low-noise Schottky diodes (Agilent HSMS2815). The resulting DC voltage is low-pass filtered and amplified to a nominal level of 10 V.

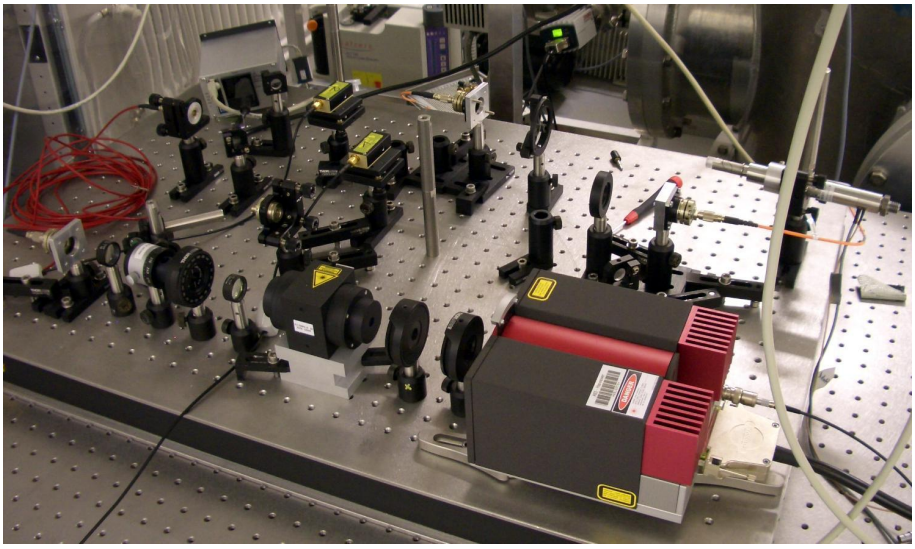

Figure 16: The modulation bench, showing the Innolight laser (bottom), the discrete (free-beam) and fiber coupling components, the two free-beam AOMs (top center) and the PZT used as OPD actuator (top right).

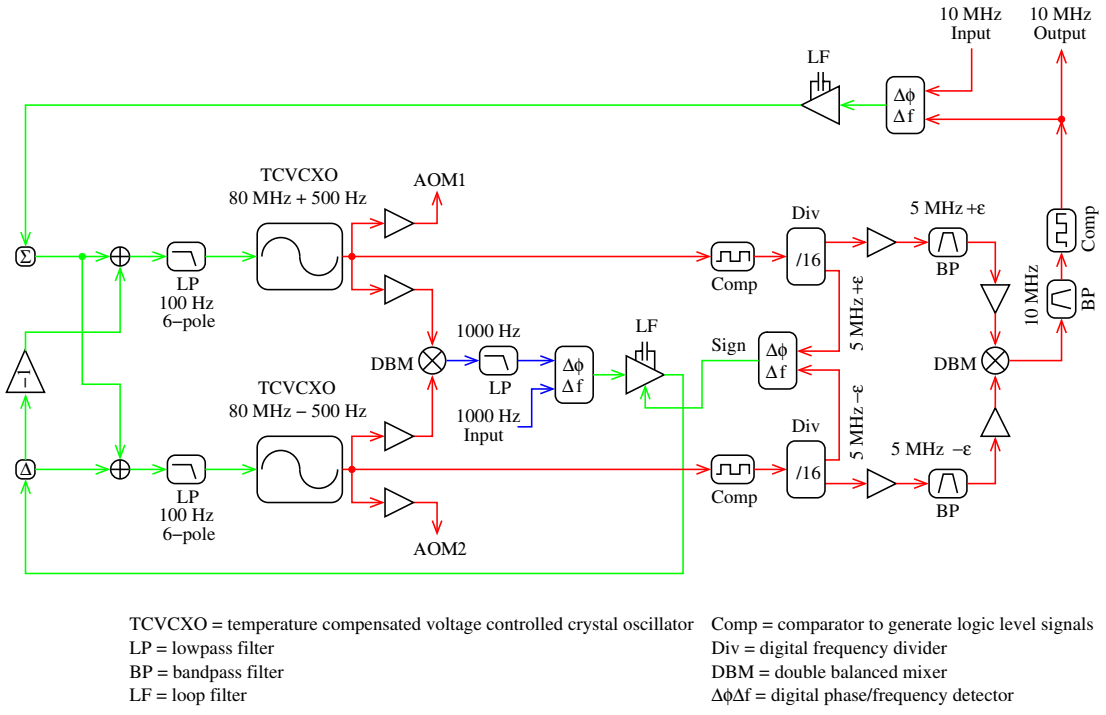

Figure 17: Block diagram of the frequency synthesizers. 1000 Hz is used in the figure as example for the heterodyne frequency, which was in reality 1623 Hz in our tests.

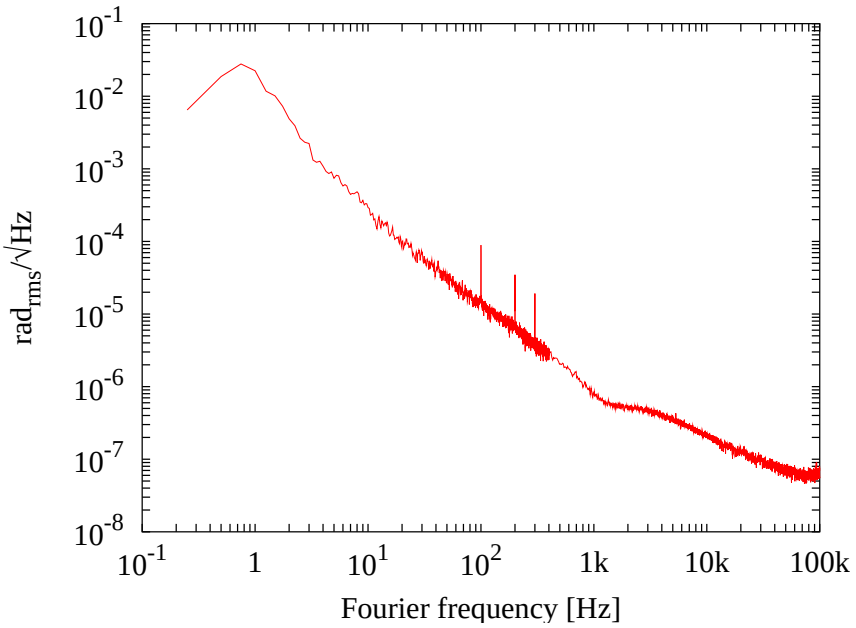

Figure 18: Measured phase noise of the frequency synthesizer. For this measurements, the both independent VCXOs were used. The PLL was modified to lock them to the same frequency with a bandwidth of $\approx 1\,\mathrm{Hz}$.

This voltage used to generated an error signal for the RF power stabilization loop by subracting a low-noise 10 V reference voltage. The servo loop is closed with a bandwidth of a few 100 kHz by attenuating the input power to the RF power module using a double-balance mixer as current-controlled attenuator. By adding another signal to the error point, the RF power can be steered away from its nominal value, thus providing an actuator (BW $> 100\,\mathrm{kHz}$) for the laser power stabilization that is based on the light levels measured on the optical bench (see Section 11 on page 81).

5.6 Phasemeter

For these experiments we have mainly used our new FPGA-based phasemeter 'PM3'. It performs the phase measurement based on a single-bin discrete Fourier transform (SBDFT). It is a breadboard that uses the same principles and algorithms that were also proposed for the EM/FM phasemeter, but can obtain better performance by using components without space qualification and not worrying about the power budget.

The photocurrent in each of its 20 equal channels is converted to a voltage in a low-noise analog front end, sent through an antialiasing filter and digitized in a dedicated 18-bit A/D converter (one per channel) at 800 kHz sampling rate. All A/D converters are triggered simultaneously.

Let the inputs from one quadrant channel 'A' be $x_i = U_A(t_i)$.

The first step, the SBDFT, comprises more than 99 % of the total computational burden. It computes

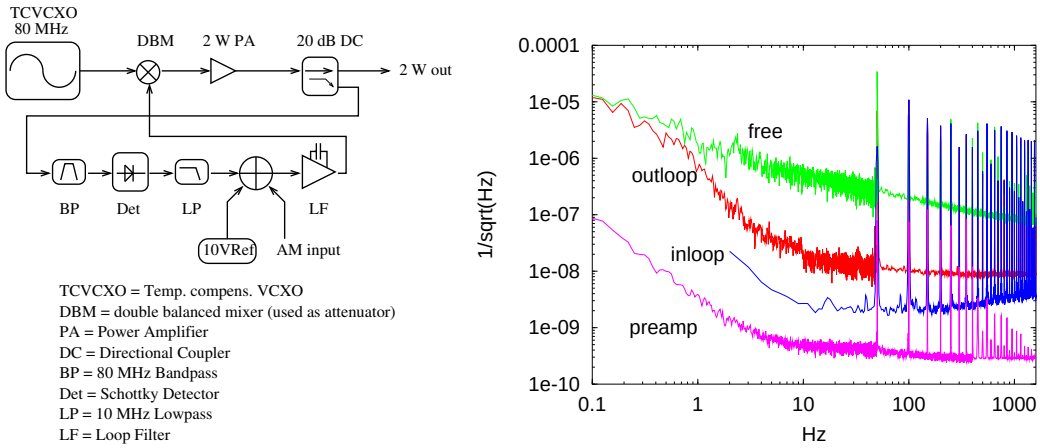

Figure 19: Block diagram of the power amplifier and amplitude control, and its measured RF amplitude noise.

$$\text{DC components:}\quad \mathrm{DC}_A, \mathrm{DC}_B, \mathrm{DC}_C, \mathrm{DC}_D \quad \text{(real)}: \quad \mathrm{DC}_A = \sum_{i=0}^{n-1} x_i, \quad \text{and}$$

$$f_{\text{het}}\ \text{components:}\quad \mathrm{F}_A, \mathrm{F}_B, \mathrm{F}_C, \mathrm{F}_D: \quad \Re(\mathrm{F}_A) = \sum_{i=0}^{n-1} x_i \cdot c_i, \quad \Im(\mathrm{F}_A) = \sum_{i=0}^{n-1} x_i \cdot s_i.$$

The constants s_i and c_i are pre-computed as $c_i = \cos\left(\frac{2\pi\, i\, k}{n}\right), s_i = \sin\left(\frac{2\pi\, i\, k}{n}\right)$. Optionally, s_i and c_i can be modified to use a time-domain window function (see Section 9.1 on page 60).

This operation is performed in a dedicated SBDFT engine (Actel APA075 FPGA with ≈ 70000 equivalent gates) per channel[5]. A block diagram is shown in Figure 21 on page 37. In this step, the data rate is reduced from 14.4 Mbit/s to 17.6 kbit/s per channel for our laboratory parameters, i.e. by a factor 800. The data are collected in a "motherboard" and sent to a PC after being buffered in a FIFO. The motherboard also generates the clocks for each front end and maintains the sine-cosine-table in a RAM (see Figure 22 on page 37).

Figure 23 on page 38 shows a photograph of the phasemeter PM3, and Figure 24 on page 38 shows the measured noise level of one phasemeter channel, compared to the average of all other channels, when a clean sine wave is applied to its input. It is clear that the noise of the phasemeter itself is no limiting factor in our measurements.

The parameters used in these experiments were:

$$\begin{aligned} f_{\text{het}} &= 10\,\text{MHz}/6160 = 1623.37\,\text{Hz}, \\ f_{\text{samp}} &= 800\,\text{kHz}, \\ n_{\text{FFT}} &= 24640, \qquad (37) \\ f_{\text{ph}} &= 32.467\,\text{Hz}, \\ k &= 50 \quad \text{(bin number)}. \qquad (38) \end{aligned}$$

[5] Since unsigned multipliers are more simple to realize in hardware than their signed counterparts, the constants c_i and s_i are given an offset to be non-negative. The offset is subtracted in the phasemeter back-end software using the measured DC components from the same segment and channel.

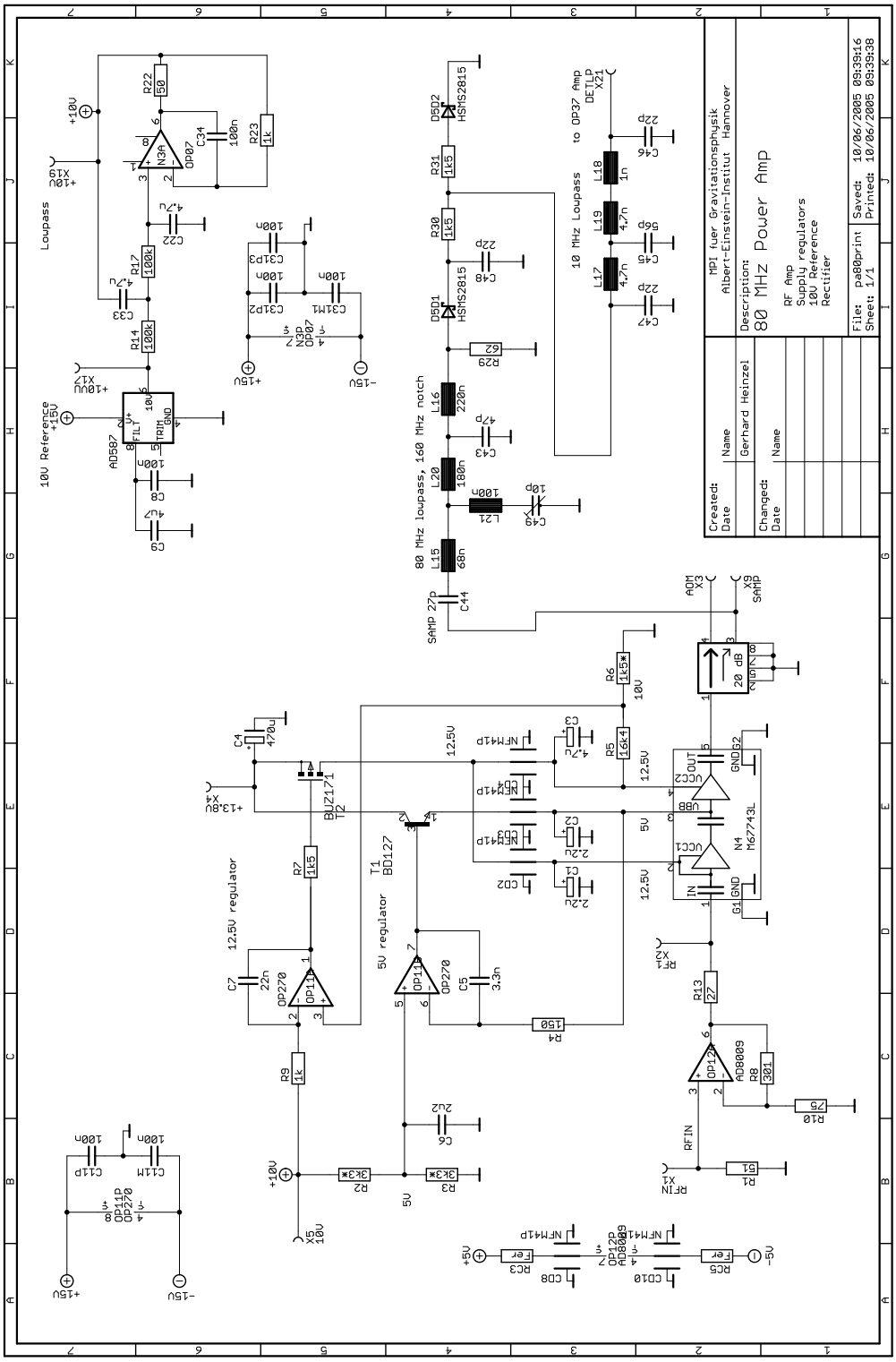

Figure 20: Circuit diagram of the power amplifier.

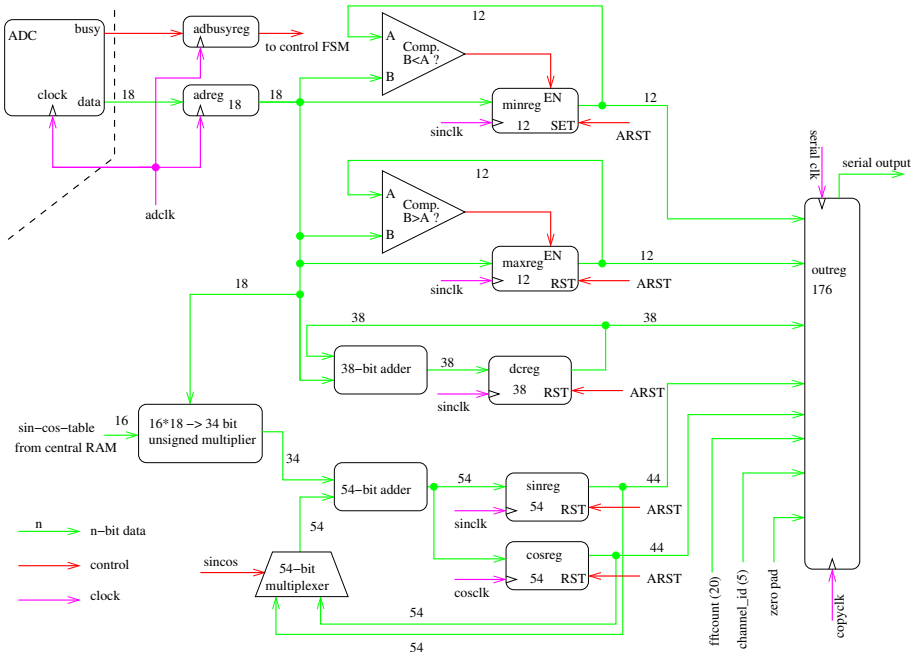

Figure 21: Simplified block diagram of a SBDFT engine implemented in an FPGA. The phasemeter contains one such FPGA per channel.

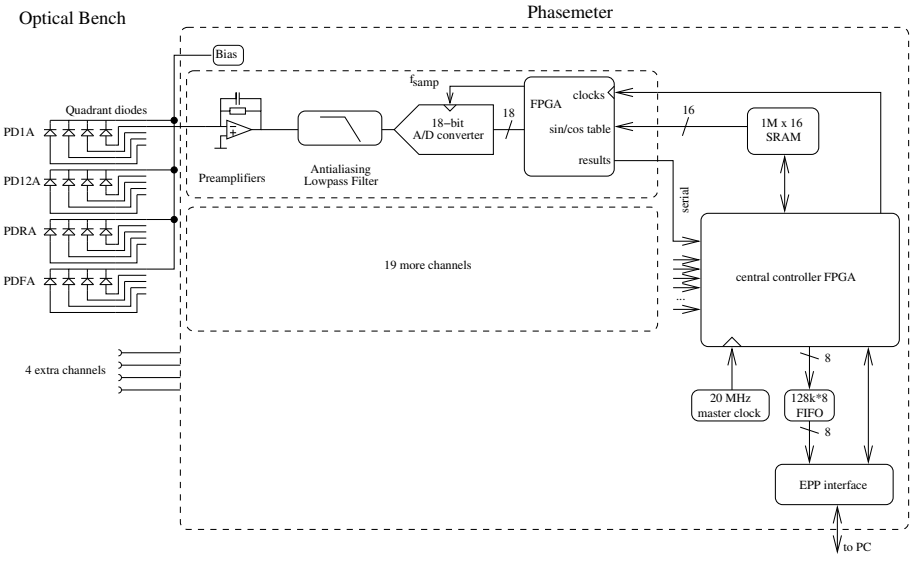

Figure 22: Simplified block diagram of the phasemeter PM3.

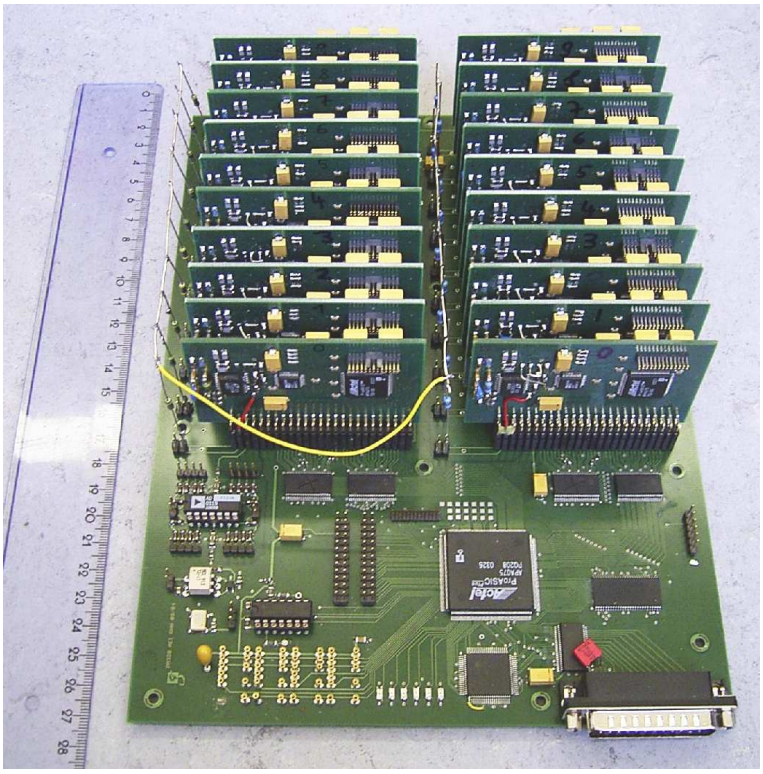

Figure 23: The phasemeter 'PM3'.

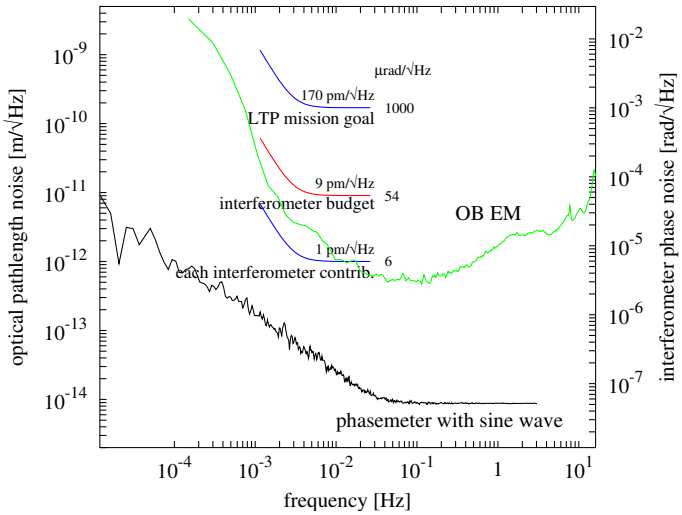

Figure 24: Performance of the phasemeter 'PM3' with a clean sine-wave as input. Also shown is the present typical noise level in the EM OB, when frequency- and OPD-stabilization are active but no other correction is applied.

The sampling clock and the heterodyne frequency are both derived from a common master oscillator (a 10 MHz crystal oscillator).

The software on the PC side is written in C under Linux, using the `gcc` complier. It communicates with the phasemeter using the parallel port (bidirectional EPP mode). During initialization, it sets various control registers inside the phasemeter FPGA and uploads the sine-cosine-table to the RAM within PM3. During the measurement, it accepts the phasemeter data (176 bits/channel × 20 channels × 32.45 samples/second), unpacks the bitstream and proceeds to process the data.

It has a graphical user interface that displays in real-time the dynamic range of all A/D channels, the alignment and contrast of four quadrant diodes and the time evolution of the x_1 and $x_1 - x_2$ longitudinal measurements. Figure 25 shows a screenshort of the user interface. In addition, all output data (raw phases, x_1 and $x_1 - x_2$, alignments, contrasts etc.) are written to a disk file in ASCII format with a data rate of $f_{\mathrm{ph}} = 32.467\,\mathrm{Hz}$ for later analysis.

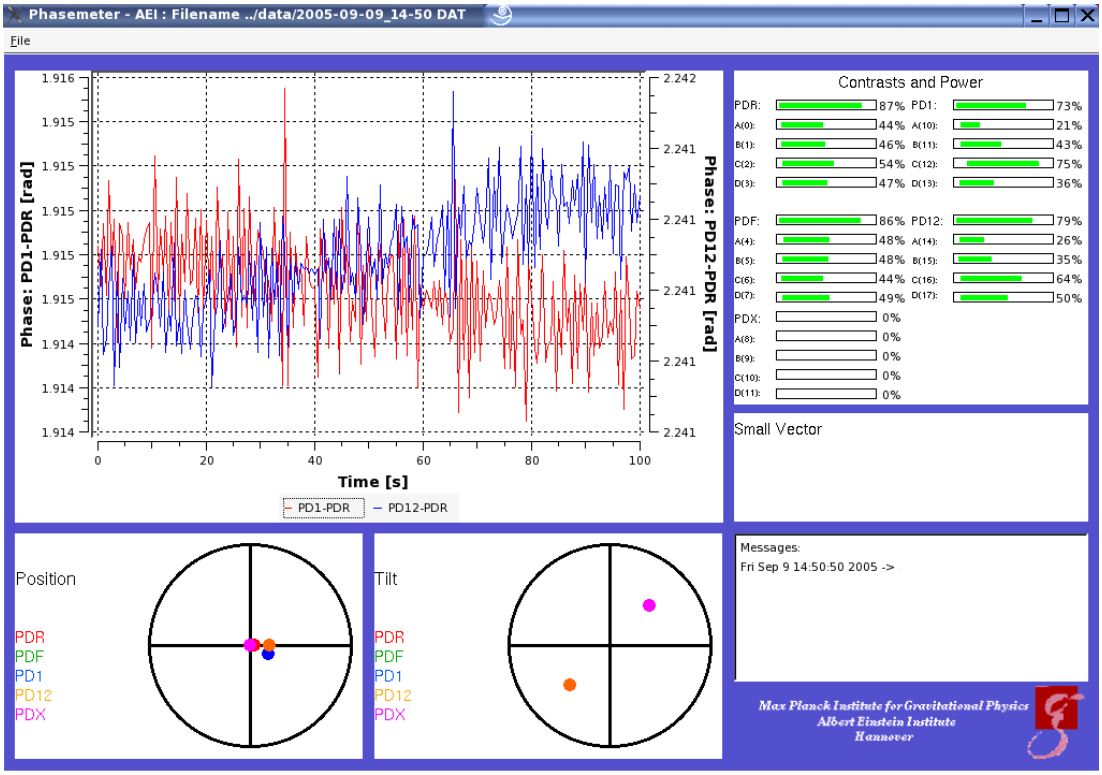

Figure 25: Photograph of the phasemeter user interface.

6 Experimental investigation of sideband-induced errors

6.1 Setup

In order to verify the calculations and, in particular, the scaling behaviour, a series of experiments was carried out in Hannover using the engineering model (EM) of the Lisa Pathfinder

Optical Bench (OB). The AOM electronics, phasemeter etc. used are described in Section 5 on page 27.

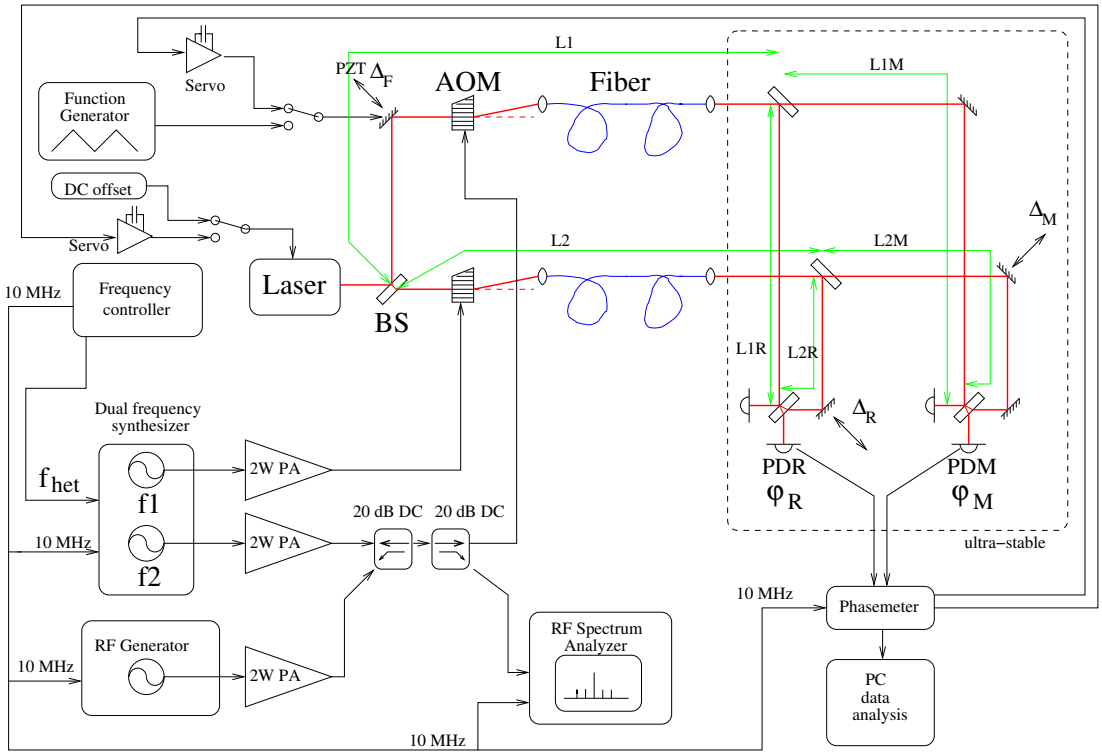

Figure 26: Overview of the test setup for the sideband measurements.

In these experiments, additional sidebands are added to the driving signal of one AOM from a synchronized RF generator (Figure 26). A 20 dB directional coupler in reverse mode is used to add the extra sideband to the nominal signal. Another 20 dB directional coupler in a back-to-back arrangement serves as sampling device for the combined spectrum, which is analyzed with a RF spectrum analyzer.

Otherwise the experiment is similar to the usual 'performance test' measurements that are performed with the OB EM: The SBDFT phasemeter is used to measure the phases of 16 (20) quadrant channels. An optional servo loop keeps the laser frequency constant by measuring $\varphi_{\mathrm{PDF}} - \varphi_{\mathrm{PDR}}$ and feeding back to the laser frequency. An offset added to the error signal of that servo loop (implemented as an analog phase shifter) allows to set variable operating points for $\varphi_{\mathrm{PDF}} - \varphi_{\mathrm{PDR}}$. For short measurements a DC voltage applied to the laser frequency control input serves the same purpose (this latter possibility is drawn in Figure 26). A Piezo in one of the fiber paths allows to control the OPD either by closing a servo loop that keeps φ_{PDR} constant with respect to the coherent phasemeter clock, or to apply a scanning signal (triangular, for example) to the OPD.

6.2 One sideband

For comparison, the typical error terms caused by first- and second-order sidebands are shown here again:

$$a_{-1}: \quad \frac{\delta\varphi}{\varepsilon} = 2\cos\left(\Delta_\mathrm{F} + \frac{\Delta_\mathrm{M} + \Delta_\mathrm{R}}{2} - \gamma\right) \cdot \sin\left(\frac{\varphi_\mathrm{M} - \varphi_\mathrm{R}}{2}\right), \tag{39}$$

$$a_{+2}: \quad \frac{\delta\varphi}{\varepsilon} = 2\cos\left(2\Delta_F + \Delta_R + \Delta_M + \gamma\right) \cdot \sin(\varphi_M - \varphi_R). \tag{40}$$

Both of them consist of two parts: The first factor is a sinusoidal function that changes as $\sin(\Delta_F)$ or $\sin(2\Delta_F)$, respectively, where Δ_F is the rapidly fluctuating optical pathlength difference between the two fiber paths. The second part depends on $(\varphi_M - \varphi_R)$ only, which represents pathlength changes on the ultra-stable optical bench (OB) and typically changes much more slowly.

In order to measure these error terms, the first factor is made to vary by large amounts in a controlled fashion, while the second factor $(\varphi_M - \varphi_R)$ should be kept constant at several values. In our experiments we have chosen the frequency interferometer (photodiodes PDF1 and PDF2) on the optical bench as 'measurement' interferometer and compared it to the reference interferometer (PDR1 and PDR2, see Figure 13 on page 30). This allows us to make use of the intentional armlength difference in the frequency interferometer in order to set $(\varphi_M - \varphi_R)$ by changing the laser frequency.

The controlled faster variation of the first factor can be achieved by two methods: changing Δ_F or changing γ. Both of these methods have been used with consistent results and will be explained now.

6.2.1 Changing Δ_F: Scanning the OPD Piezo

The most straightforward way to verify Equations (39) and (40) is to change the OPD Δ_F. This corresponds to amplifying in a controlled fashion the naturally occuring fluctuations of the OPD Δ_F, which are causing the variable noise term in the first place. To do so, a triangluar scanning signal is applied to the Piezo. Figure 27 shows a typical time series of such a scan.

While this method allows a direct verification of the calculations, and in particular to distinguish between the $\sin(\Delta_F)$ and $\sin(2\Delta_F)$ cases, it is limited in its Signal-to-noise ratio (SNR) and thus less useful for small sideband amplitudes. This is because the dynamic range of the Piezo allows only a few 10 cycles variation of the OPD Δ_F, before the direction must be reversed. Also, the naturally occuring fluctuations of the OPD Δ_F cannot be removed and add to the intended triangular scan.

6.2.2 Changing γ: sidebands with frequency offset

A better SNR can be obtained by varying γ. All theoretical results are also true for the special case of $\gamma = \omega_\mathrm{off} \cdot t$ where $\omega_\mathrm{off} = 2\pi f_\mathrm{off}$ represents a frequency offset of the sideband from its nominal frequency. We have typically chosen $f_\mathrm{off} = 5\,\mathrm{Hz}$, well within the bandwidth of the phasemeter but high enough to produce a characteristic output signal well above the noise floor. According to Equations (39) and (40), the phase error will then also be periodic with $f_\mathrm{off} = 5\,\mathrm{Hz}$ and can be measured by narrowband spectral analysis[6] of the phase data time series. Long

[6] We computed a linear spectrum of the fluctuations using improved FFT methods and using a 'flat-top' time-domain window that yields the correct peak amplitude independent of the location of the peak frequency within one frequency bin.

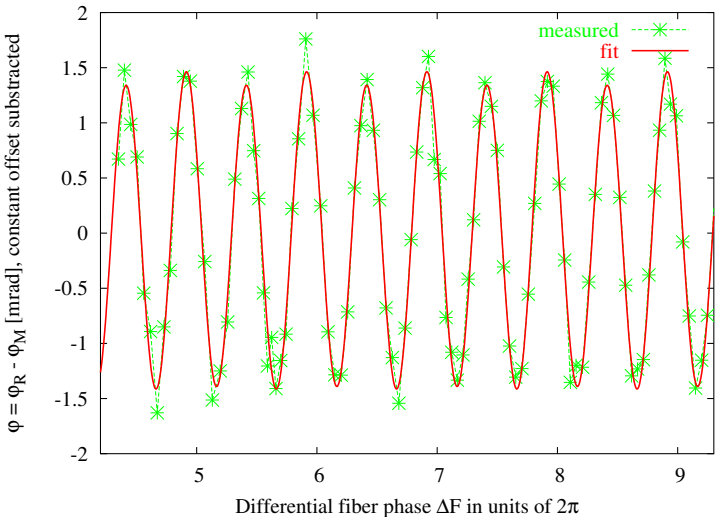

Figure 27: φ as function of Δ_F when the OPD PZT is scanned. In this measurement, the $\sin(2\Delta_F)$ component is dominant. See also Figure 4 on page 15 for a similar, older, measurement where a significant $\sin(\Delta_F)$ component is also present.

measurement times are possible because the stabilization loops for the laser frequency and, more importantly, the OPD can be used. Figure 28 on the next page shows the experimental setup.

Figure 29 on the following page and Figure 30 on page 44 show extracts from typical[7] time series that confirm the $\sin\left(\frac{\varphi_M-\varphi_R}{2}\right)$ and $\sin\left(\varphi_M-\varphi_R\right)$ factors in Equations (39) and (40).

We have also done measurements to quantitatively verify Equations (39) and (40). A sideband with 5 Hz frequency offset was added as described above. Its amplitude compared to the carrier was

$$\varepsilon_{\mathrm{el}} = -39.6\,\mathrm{dbc} = 0.01047. \tag{41}$$

Using the results of Figure 9 on page 26 at the typical operating point 32 dBm, we estimated[8]

$$\varepsilon_{\mathrm{opt}} = 0.0052. \tag{42}$$

From Equation (39) it follows that the amplitude (zero → peak) of the error term $\delta\varphi$ should be

$$\delta\varphi_{0\to\mathrm{pk}} = 2\,\varepsilon_{\mathrm{opt}}\,\sin\left(\frac{\varphi_M-\varphi_R}{2}\right), \tag{43}$$

and the RMS amplitude

$$\delta\varphi_{\mathrm{rms}} = \sqrt{2}\,\varepsilon_{\mathrm{opt}}\,\sin\left(\frac{\varphi_M-\varphi_R}{2}\right), \tag{44}$$

The results from these measurements were:

[7] For practical reasons, these two measurements were done using a pair of sidebands induced by AM with an offset of 5 Hz instead of a single sideband.

[8] These measurements were done before the discrepancy between $\varepsilon_{\mathrm{el}}$ and $\varepsilon_{\mathrm{opt}}$ was discovered, and hence $\varepsilon_{\mathrm{opt}}$ was not directly measured.

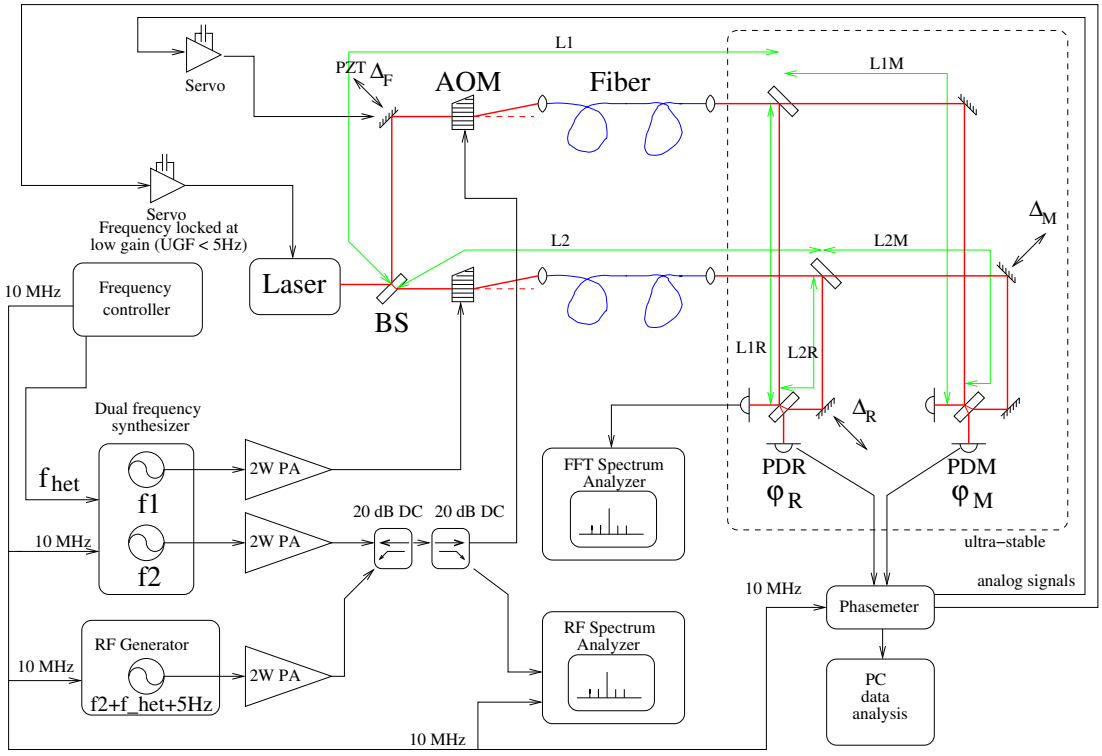

Figure 28: Experimental setup for sideband investigations using sidebands with frequency offset.

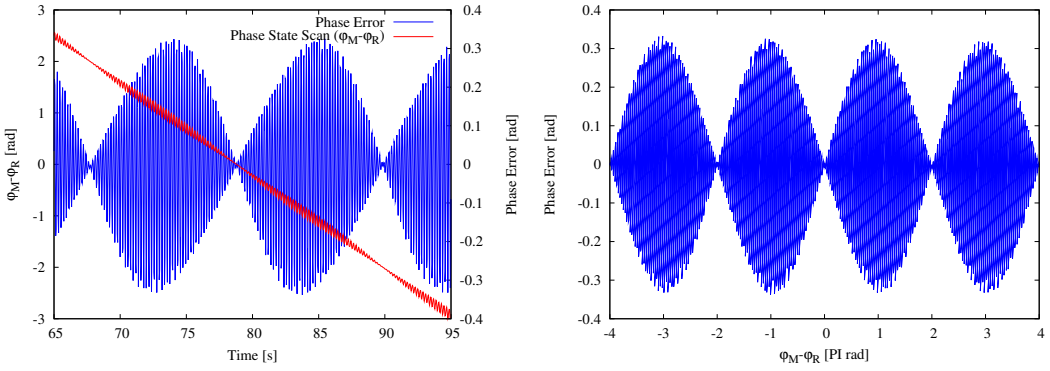

Figure 29: Phase $\varphi = \varphi_M - \varphi_R$ and its error (linear drift subtracted) when strong sidebands at an offset of $f_{\rm het}$ are added to the RF signal. This illustrates and confirms the sin $\left(\frac{\varphi_M - \varphi_R}{2}\right)$ term in Equation 39 on page 41.

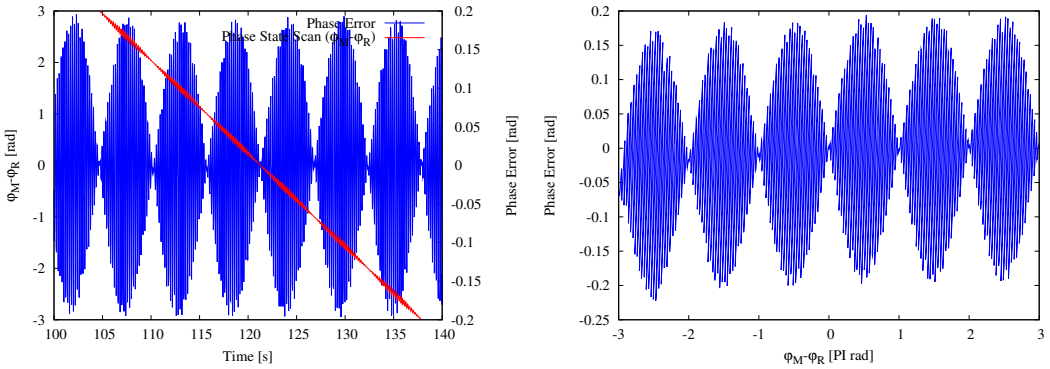

Figure 30: Phase $\varphi = \varphi_M - \varphi_R$ and its error (linear drift subtracted) when strong sidebands at an offset of $2 \times f_{\mathrm{het}}$ is added to the RF signal. This illustrates and confirms the $\sin(\varphi_{\mathrm{M}} - \varphi_{\mathrm{R}})$ term in Equation 40 on page 41.

sideband	φ [rad]	$\delta\varphi_{\mathrm{rms}}$	$\delta\varphi_{\mathrm{rms}}$(theor.)	ratio $\delta\varphi_{\mathrm{rms}}$(theor.)/$\delta\varphi_{\mathrm{rms}}$
a_{-1}	0.0155	0.0001	5.7e-5	0.58
a_{-1}	0.7858	0.0030	0.0028	0.94
a_{-1}	1.5676	0.0055	0.0052	0.95
a_{-1}	3.1354	0.0077	0.0074	0.96
a_{+1}	0.0017	8.2e-5	6.2e-6	0.08
a_{+1}	0.7906	0.0029	0.0028	0.97
a_{+1}	1.5941	0.0051	0.0052	1.03
a_{+1}	3.1417	0.0076	0.0073	0.96
a_{+2}	0.0159	0.0002	0.0001	0.5
a_{+2}	0.7990	0.0075	0.0052	0.70
a_{+2}	1.5602	0.011	0.0073	0.67
a_{+2}	3.1400	8.7e-5	1.2e-5	0.13

Figures 31 on the next page and 32 on the following page show the results for the first- and second-order sidebands, respectively.

While the results for the first-order sidebands are in good agreement with the theory, those for the second-order sidebands show a discrepancy of about 30 %, for which we have no final explanation, although qualitative experience suggests that the strong second-order sidebands produce further sidebands due to nonlinear intermodulation processes in the power amp (see Section 8 on page 52), which contributed to the measured phase error.

The data from Table 1 on page 25 was also analyzed to compare quantitatively the theoretical predictions and the measured phase error. Figures 33 on page 46 and 34 on page 46 show the results, which are in reasonable agreement with the theory. The fact that the measured phase error is a little higher than the predicted one, is possibly caused by an underestimation of $\varepsilon_{\mathrm{opt}}$ due to a suboptimal setting of the FFT analyzer.

We have also used this method (changing γ via a frequency offset) to verify the scaling behaviour discussed in Section 3.4 on page 21.

Figure 35 on page 47 shows the results for some first- and second-order sidebands. The absolute level of the curves is not well defined, because $(\varphi_M - \varphi_R)$ was not controlled or recorded during these measurements (they were done at the start of the investigations, when the theoretical

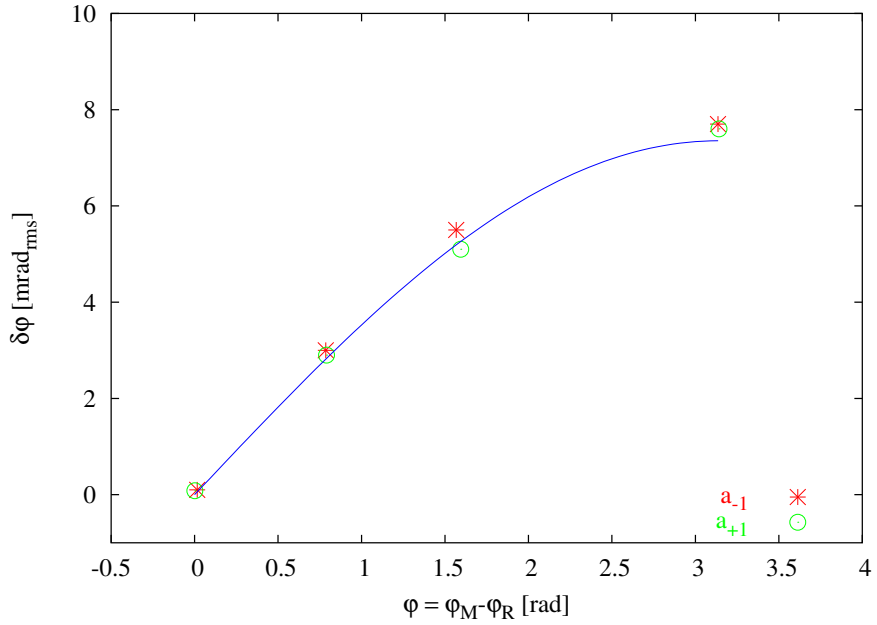

Figure 31: Measured and predicted phase error by first-order sidebands.

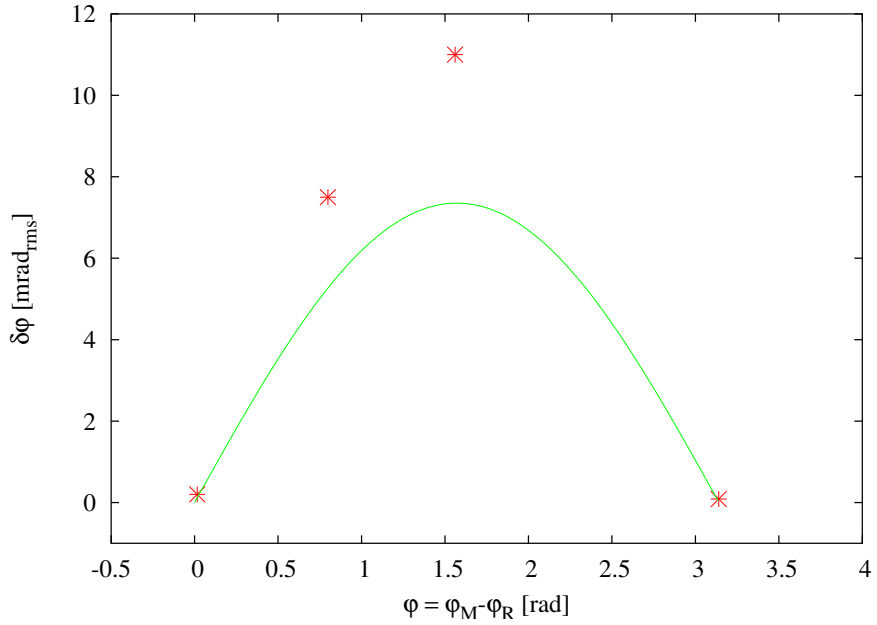

Figure 32: Measured and predicted phase error by second-order sidebands.

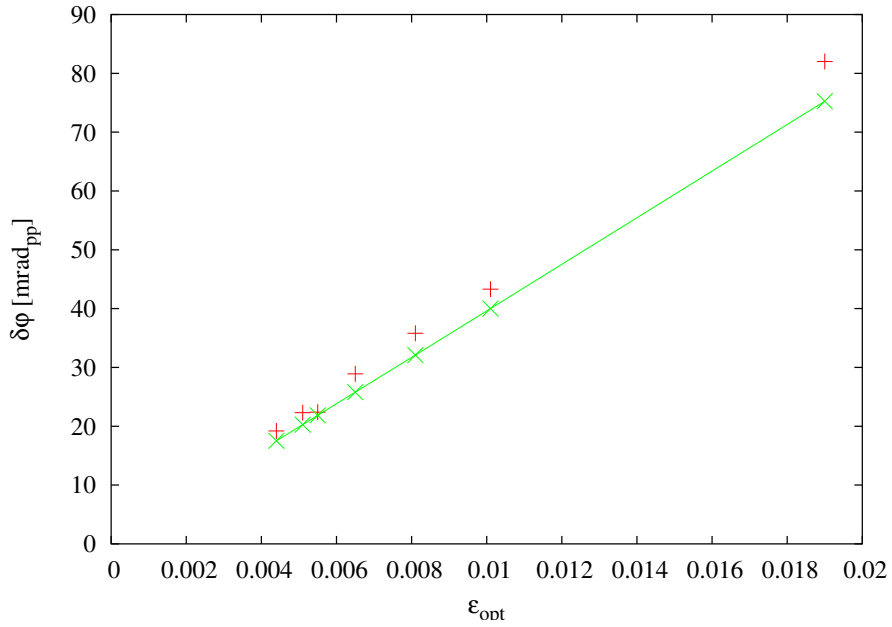

Figure 33: Measured and predicted phase error by first-order sidebands, using the data from Table 1 on page 25. The '×' symbols connected by the line are predictions from the measured $\varepsilon_{\mathrm{opt}}$, while the '+' symbols are measurements of the phase error from the phasemeter.

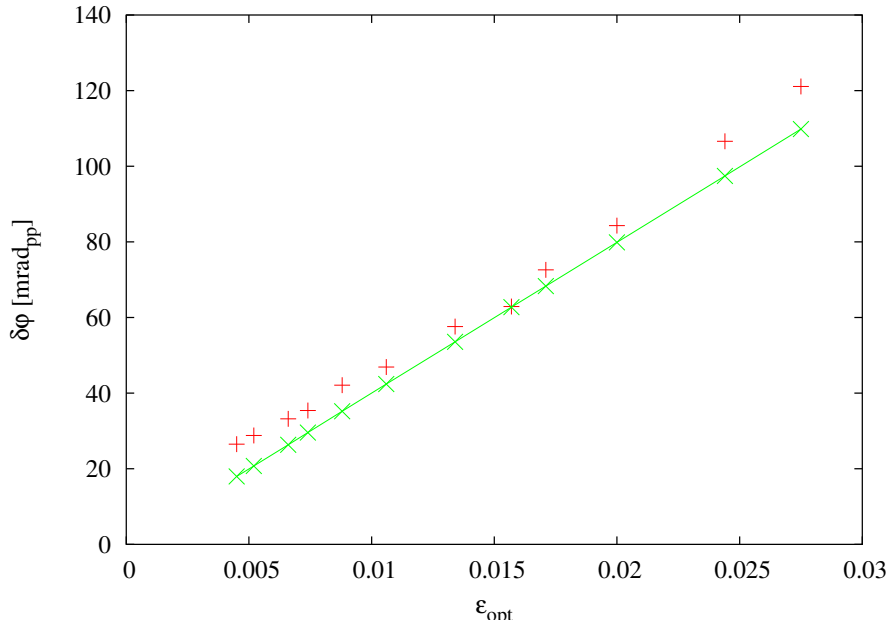

Figure 34: Measured and predicted phase error by second-order sidebands, using the data from Table 1 on page 25. The '×' symbols connected by the line are predictions from the measured $\varepsilon_{\mathrm{opt}}$, while the '+' symbols are measurements of the phase error from the phasemeter.

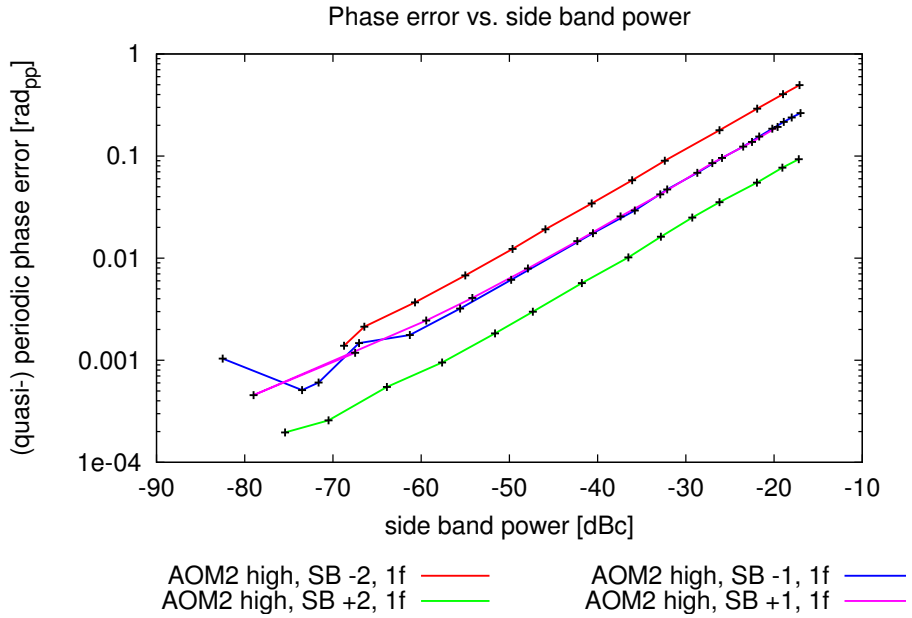

Figure 35: Measured scaling behaviour of single sideband induced phase errors.

analysis was not yet completed). During each measurement, however, $(\varphi_M - \varphi_R)$ was nearly constant. The main result is a verification of the unfavourable scaling behaviour: A reduction of the sideband amplitude by 20 dB causes a reduction of the phase error by a factor of 10.

6.3 AM

Further quantitative measurements were done by adding intentional amplitude modulation (AM) on one light beam, in order to verify the results of Section 3.2 on page 19. The light amplitude was modulated at $f_{\text{het}} + 5\,\text{Hz}$ by applying a suitable sinusoidal signal to the amplitude control input of one AOM driver. The resulting modulation index was varied over ≈ 1 decade and monitored both by measuring the sideband spectrum in the RF drive signal ('electrical') and by measuring the effective modulation on the light ('optical'). These two modulation indices differ by about a factor of 2, in accordance with the results of Section 4 on page 21. The phase error was measured by performing spectral analysis on the phasemeter output as described in Section 6.2.2 on page 41. Table 2 on the following page lists the results, and Figure 36 on the next page shows a comparison between predicted and measured phase error, which are in reasonable agreement.

6.4 FM

Another set of quantitative measurements were done by adding intentional phase/frequency modulation (PM/FM) on one light beam, in order to verify the results of Section 3.2 on page 19. Remember that those results predict that no phase error is caused by a pair of first-order sidebands which originate from PM/FM. One AOM frequency was modulated at $f_{\text{het}} + 5\,\text{Hz}$ by applying a suitable sinusoidal signal to the frequency input of the VCXO in one AOM driver

electrical			optical				phasemeter			
carrier [dBm]	SB [dBm]	m_{el}	U_{DC} [mV]	U_{DC} [$\mathrm{mV_{pp}}$]	m_{opt}	$m_{\mathrm{opt}}/m_{\mathrm{el}}$	$\varphi_M - \varphi_R$ [rad]	$\delta\varphi_{\mathrm{meas}}$ [$\mathrm{rad_{pk}}$]	$\delta\varphi_{\mathrm{calc}}$ [$\mathrm{rad_{pk}}$]	ratio
32.8	5.6	0.08730	690	107	0.03877	0.44406	-3.21085	0.08665	0.07749	0.89
32.8	4.7	0.07871	695	96	0.03453	0.43873	-3.21275	0.07913	0.06902	0.87
32.8	4.1	0.07346	650	84	0.03231	0.43982	3.06753	0.06949	0.06457	0.93
32.8	2.5	0.06110	660	72	0.02727	0.44637	3.06722	0.05964	0.05451	0.91
32.8	1.1	0.05200	655	60	0.02290	0.44037	-3.21602	0.04620	0.04577	0.99
32.8	-0.8	0.04179	655	48	0.01832	0.43844	-3.21625	0.03858	0.03662	0.95
32.7	-3.2	0.03206	650	36	0.01385	0.43182	3.06728	0.02832	0.02767	0.98
32.7	-6.6	0.02168	655	24	0.00916	0.42255	-3.21646	0.02028	0.01831	0.90
32.7	-12.8	0.01062	665	12	0.00451	0.42488	3.06672	0.00957	0.00902	0.94

Table 2: Results of AM modulation.

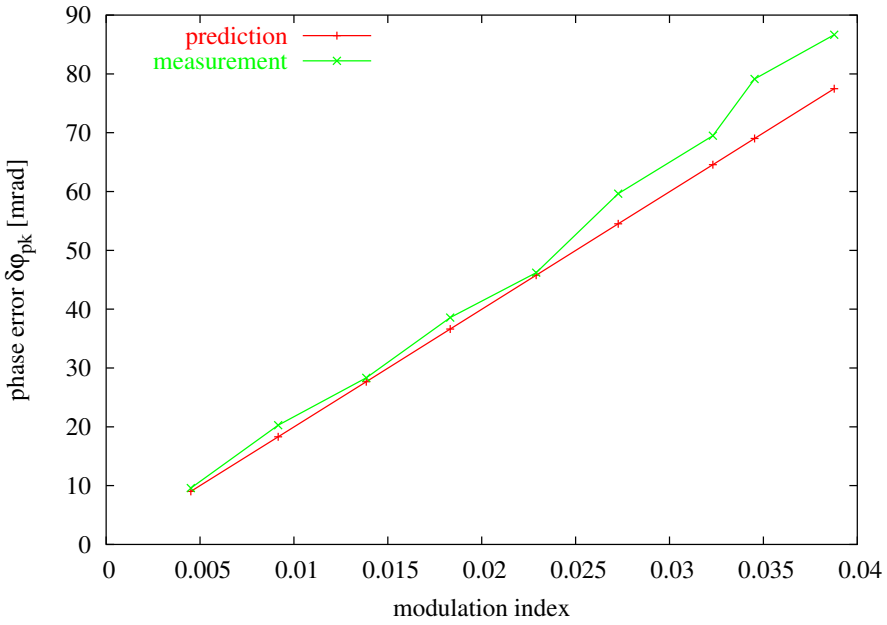

Figure 36: Comparison between prediction and measurement for AM sidebands.

in addition to the PLL feedback signal. Since the PLL has a bandwidth of only a few Hz, it does not influence this modulation.

The resulting modulation index was varied over almost one decade and monitored by measuring the sideband spectrum in the RF drive signal. The phase error was measured by performing spectral analysis on the phasemeter output as described in Section 6.2.2 on page 41. $\varphi_M - \varphi_R$ was kept very close to π rad during these measurements. Table 3 lists the results, which show that in accordance with the prediction the phase error is much smaller than would be expected if the effect of the two sidebands would not cancel.

carrier [dBm]	SB [dBm]	m_{el}	$\delta\varphi_{\mathrm{calc}}$ [$\mathrm{mrad_{pk}}$]	$\delta\varphi_{\mathrm{meas}}$ [$\mathrm{mrad_{pk}}$]	ratio
32.8	-6.0	0.0115	23.0	0.48	0.021
32.8	-2.5	0.0172	34.4	0.75	0.022
32.8	0.0	0.0229	45.8	1.00	0.022
32.8	2.0	0.0288	57.7	1.23	0.021
32.8	3.5	0.0343	68.6	1.53	0.026
32.8	5.0	0.0407	81.5	1.74	0.021
32.8	5.8	0.0447	89.3	1.94	0.022
32.8	7.8	0.0562	112.5	2.25	0.020
32.7	9.3	0.0676	135.2	2.88	0.021
32.7	10.9	0.0813	162.6	3.34	0.021

Table 3: Results of FM modulation. The column $\delta\varphi_{\mathrm{calc}}$ shows the results that would be predicted if no cancellation of the sidebands would occur.

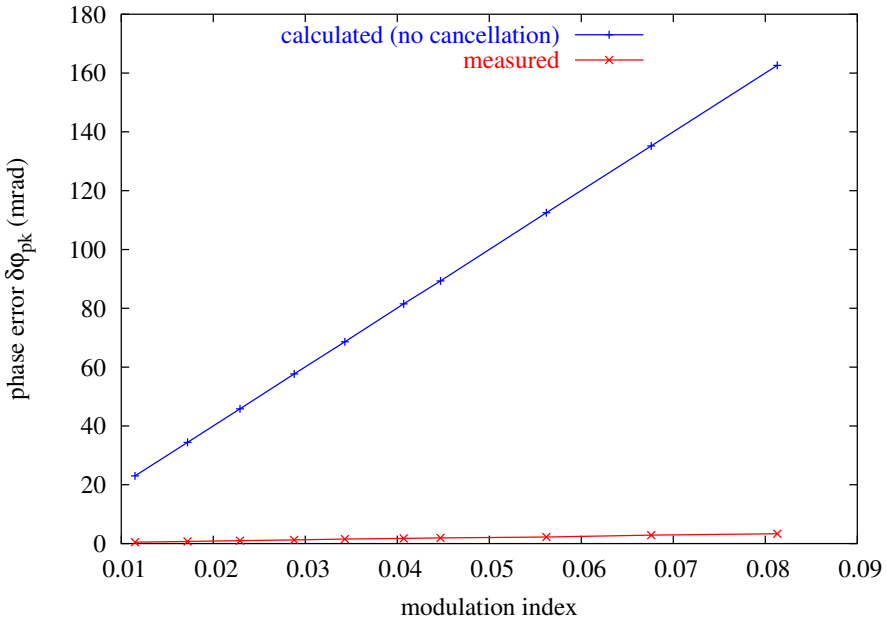

Figure 37: Comparison between prediction and measurement for FM sidebands. The prediction is actually zero phase error. For comparison, the upper curve shows the phase error that was calculated under the (wrong) assumption that the two sidebands do not cancel.

7 OPD fluctuations in laboratory environment

The sideband-induced error term is caused by a combination of sidebands and OPD fluctuations. It is hence important to know the behaviour of the OPD fluctuations, in particular for the design of the OPD actuator and its associated servo loop.

Figure 38 shows a typical time series of the fluctuations (in the Hannover lab), and Figure 39 on the following page shows typical spectra, both from the Hannover lab and the TNO lab. Measurements from Glasgow are also very similar.

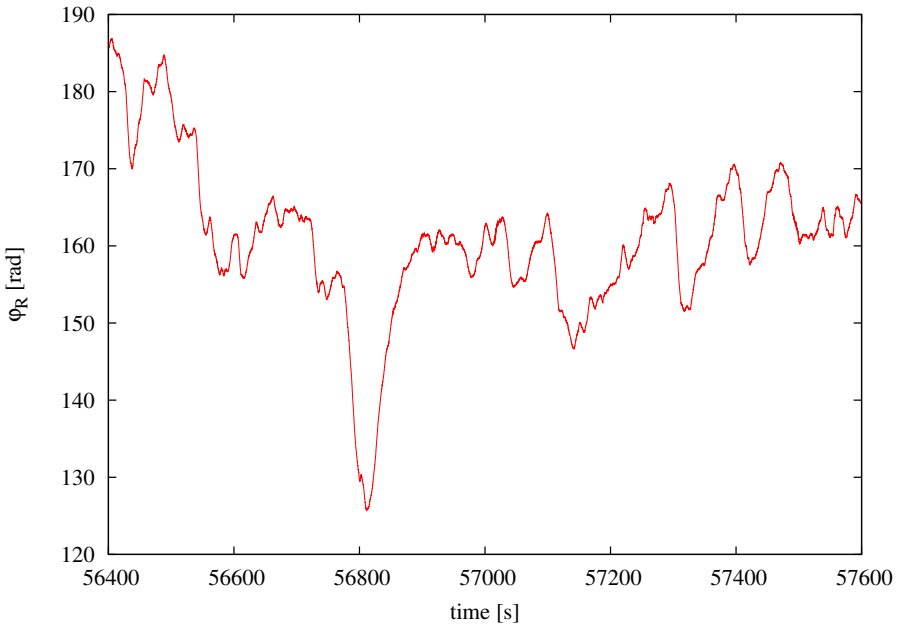

Figure 38: Typical time series of the unstabilized OPD fluctuations in the Hannover lab.

In Figure 40 on the next page, the fluctuation spectra (which are measured in radians) were first converted into equivalent displacements, assuming that they are caused by only one component such as a fiber injector or the length of a piece of fiber[9]. The displacements were then converted in velocities (expressed as μm/s) and rms-integrated from DC to the frequency that is shown as x-axis on the plot.

Figure 41 shows a typical time-series of the OPD fluctuations, also converted into an equivalent velocity. In this case the velocity was estimated by numerical differencing of the time series.

These velocities are required to design the OPD actuator. In accordance with preliminary estimations, it seems that a maximal velocity of 1 μm/s is sufficient.

Unfortunately these measurements are only of limited usefulness for the design of LTP, since in orbit the fluctuations will be very different (much smaller, we expect).

[9] A reflective component used in normal incidence would have only half of that velocity.

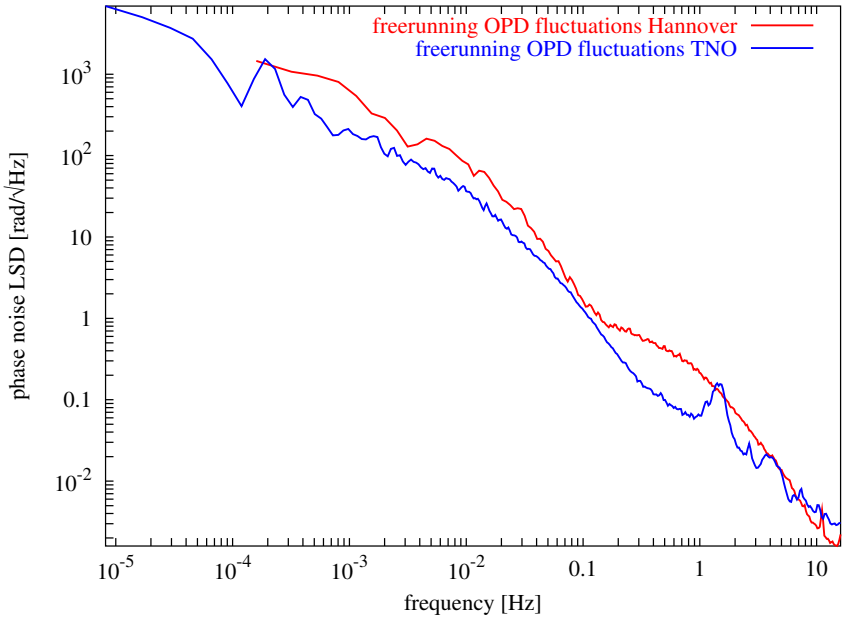

Figure 39: Typical spectra of the unstabilized OPD fluctuations in the Hannover lab and at TNO.

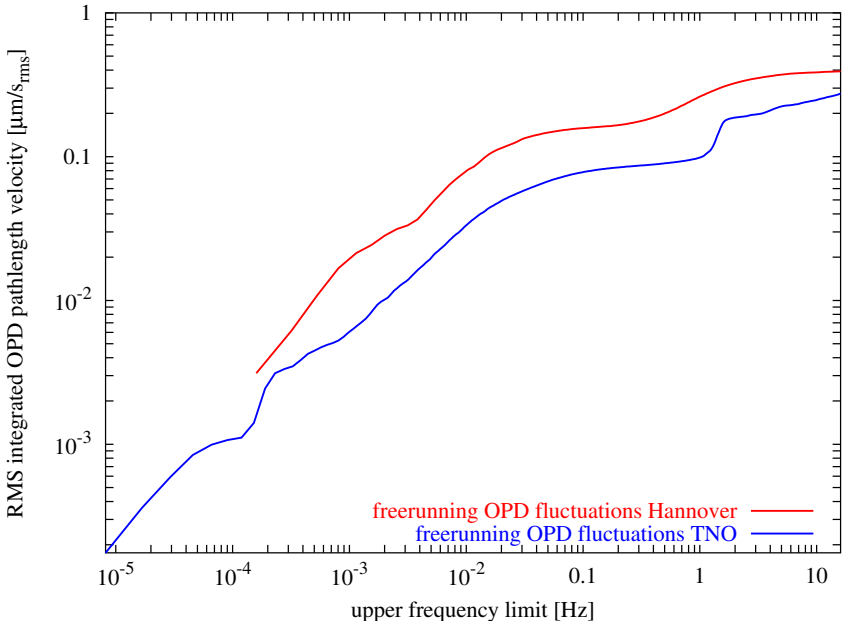

Figure 40: OPD fluctuation spectra of Figure 7 converted in velocity and rms-integrated.

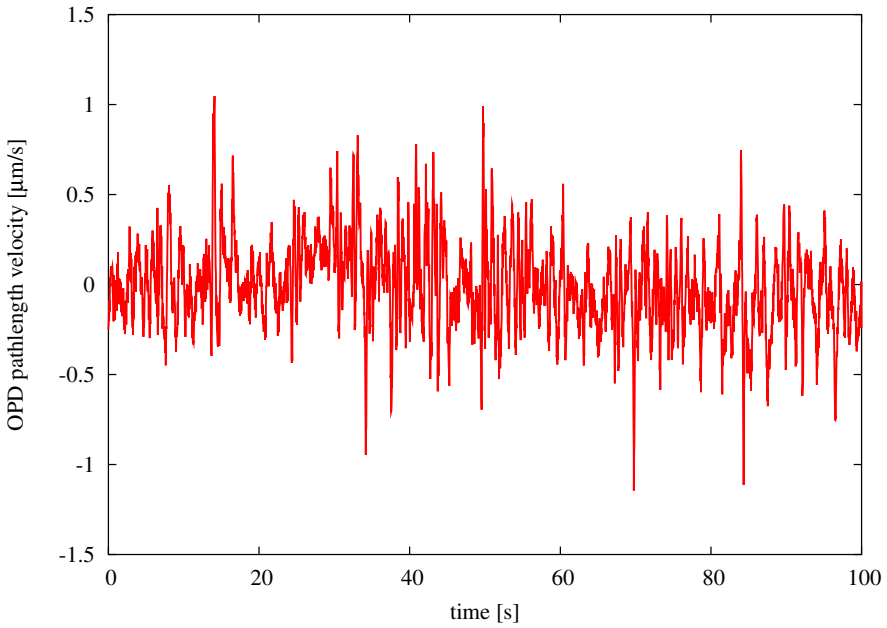

Figure 41: OPD fluctuation time series converted in velocity.

8 Origin of sidebands in our prototype

We have conducted a series of measurements of the RF spectra that drive the AOMs in order to identify the origin of the sidebands in our prototype. Please note that all electronics was built about 4 years ago, when we started to work on heterodyne interferometry and did not yet know about the sideband problems. The setup is described in Section 5 on page 27, in particular Sections 5.4 and 5.5 on page 32).

Figure 42 shows spectra measured at the output of the power amplifier under various conditions. These measurements show that the sidebands appear when the power amplifiers are switched on, indicating that they are caused by RF pickup (as opposed to crosscoupling via the PLL).

This is confirmed by the measurements of Figure 43 which were taken with both VCXO's and PA's running, but the PLL disconnected, such that the frequencies drifted to their respective limits. Even with all PLL cables removed, the symmetrical sideband structure appears.

Further measurements showed clearly that the sidebands are produced *in the power amplifier*. We have, for example, completely disconnected the VCXO and PLL and driven both 'naked' power amplifiers from commercial RF generators instead. As soon as both amplifiers are running at frequencies close to each other, they start to interact and produce sidebands. Before that, we had suspected the VCXO's to be responsible and shielded them with a copper enclosure (see Figure 44 on page 55), without any noticeable effect.

This observation is confirmed by the measurements of Figure 45 which were taken with everything running. The amount of the sidebands could be changed by physically moving the two power amplifiers, but without changing any connections.

The nature of the sidebands was investigated in another series of measurements. In Figure 46, a frequency modulation (FM) at f_{het} was added to VCXO2 while VCXO1 and both power amplifiers were also running. By adjusting the amplitude and phase of the frequency modulation,

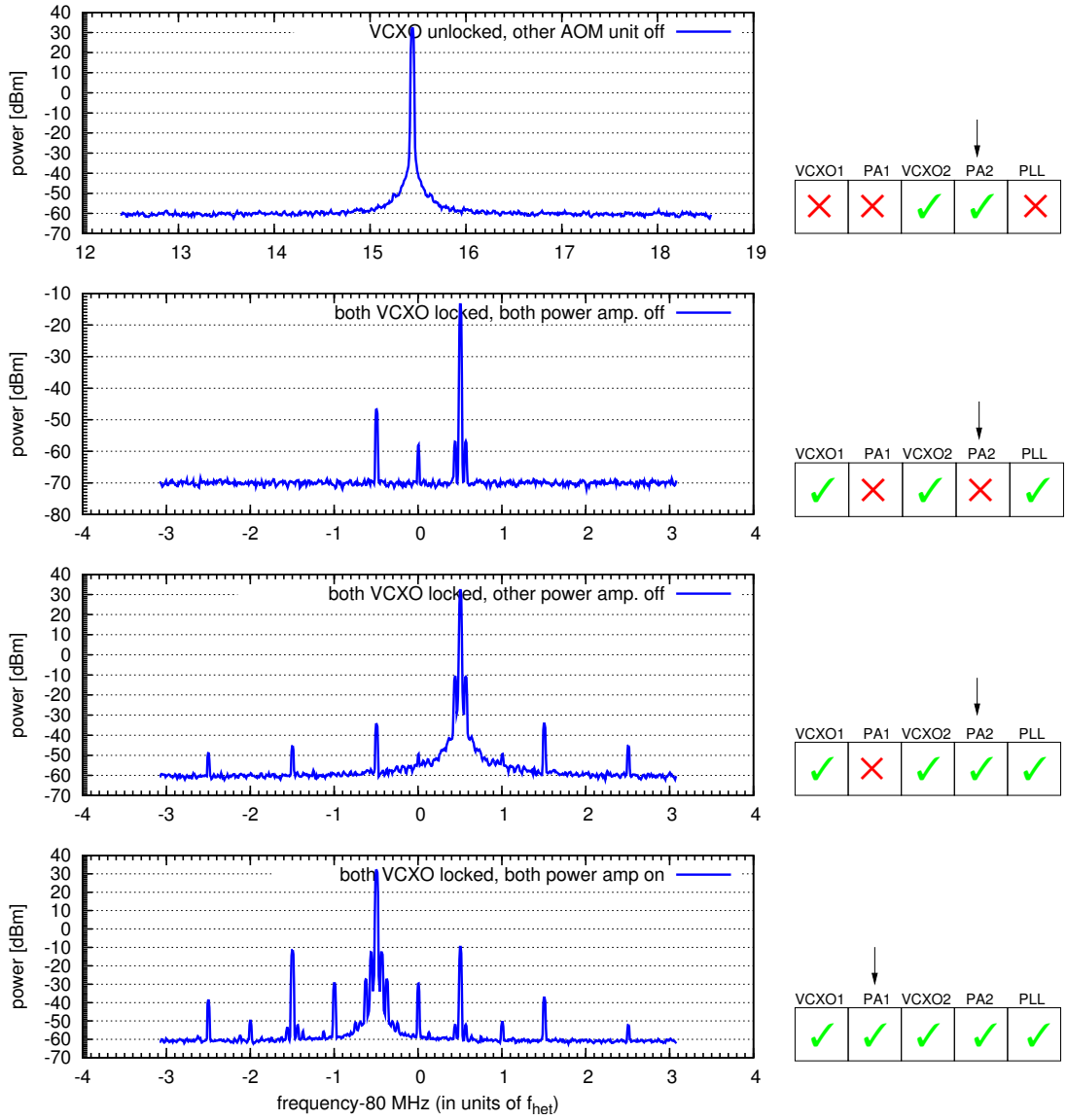

Figure 42: Spectra of AOM RF drive signal under various conditions. The arrow indicates where each measurement was done.
Top: One VCXO together with its PA has a clean spectrum without sidebands.
Second: Both VCXO's on and locked by the PLL, but both PA's off show some crosstalk of the other frequency, but no symmetrical sideband structure.
Third: When the other PA is off, but both VCXOs are running, the symmetrical sideband structure already appears.
Bottom: the symmetrical sideband structure gets stronger when the other VCXO is amplified in its PA.

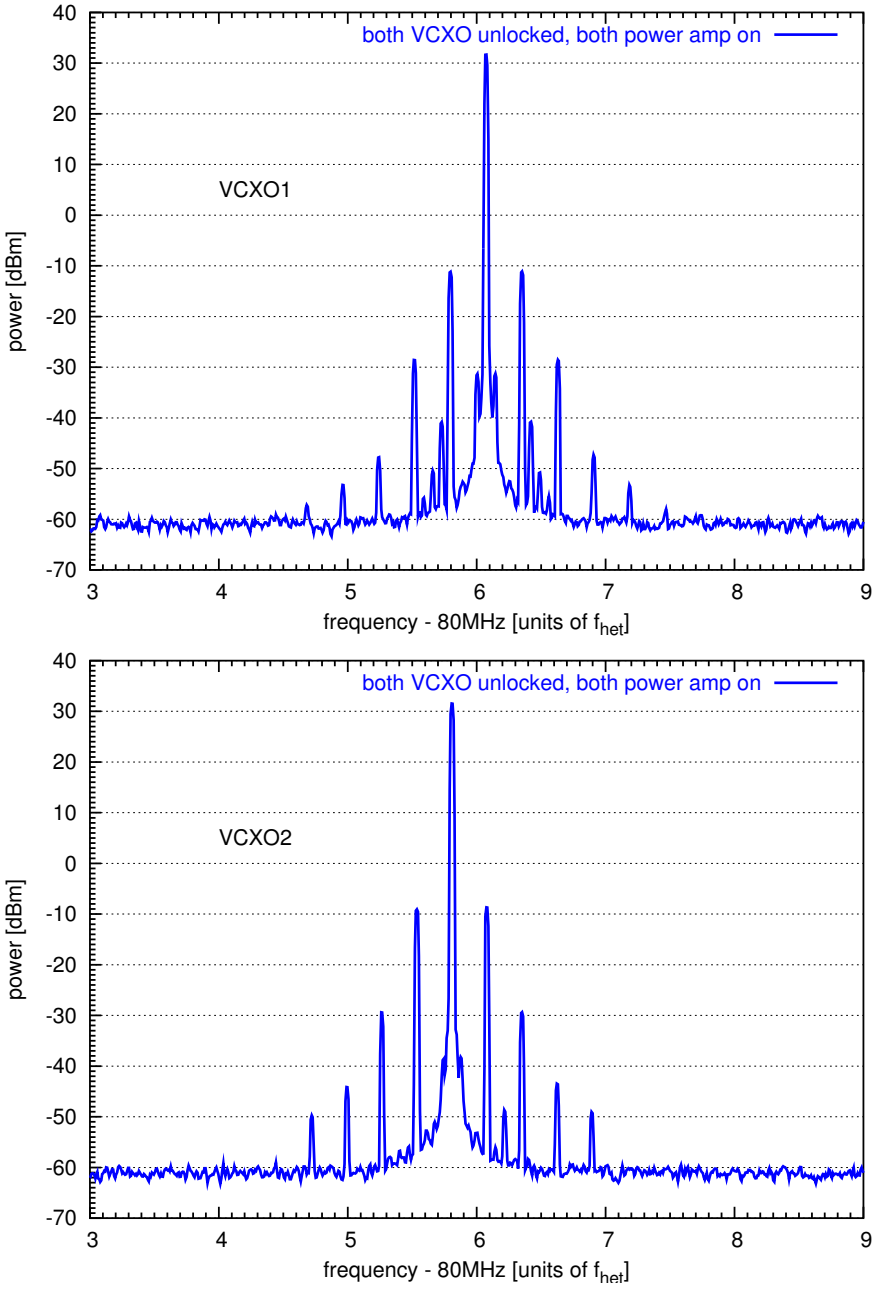

Figure 43: Spectra of AOM RF drive signal with PLL disconnected, showing that the PLL or its connections are not responsible for the sidebands.

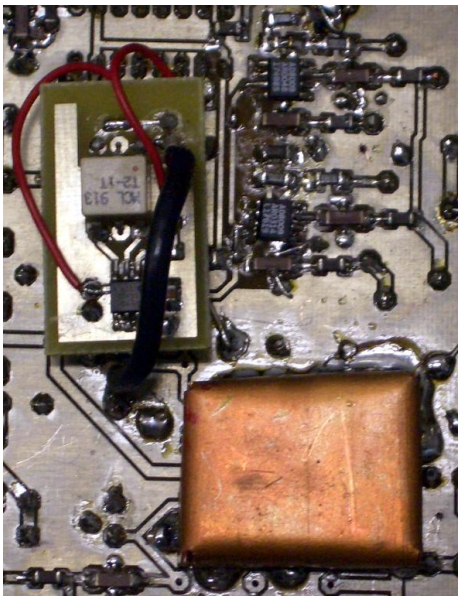

Figure 44: Copper shield covering the VCXO.

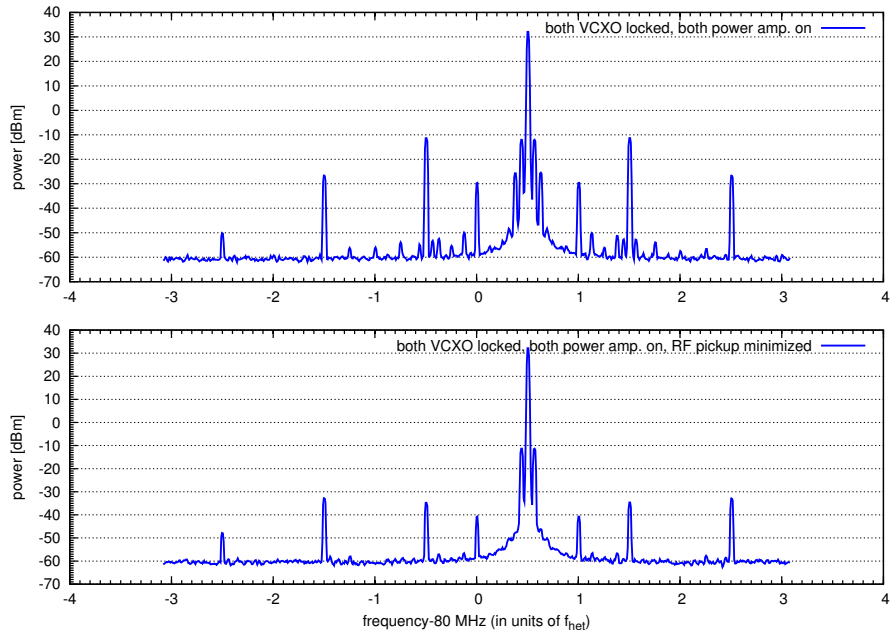

Figure 45: With the full configuration (everything on), the amount of the sidebands could be changed by physically moving the two power amplifiers, but without changing any connections.

the first-order sidebands could almost completely be cancelled. This shows that the nature of the first-order sidebands is FM/PM instead of AM. This observation is confirmed by the fact that the effect of the 1st order sidebands in the phase readout is much smaller than it should be if the sidebands were AM (see Section 3.2 on page 19). The second-order sidebands are, however, unaffected. This indicates that they are not simply the J_2 sidebands associated with a FM/PM at $f_{\rm het}$, but have another origin.

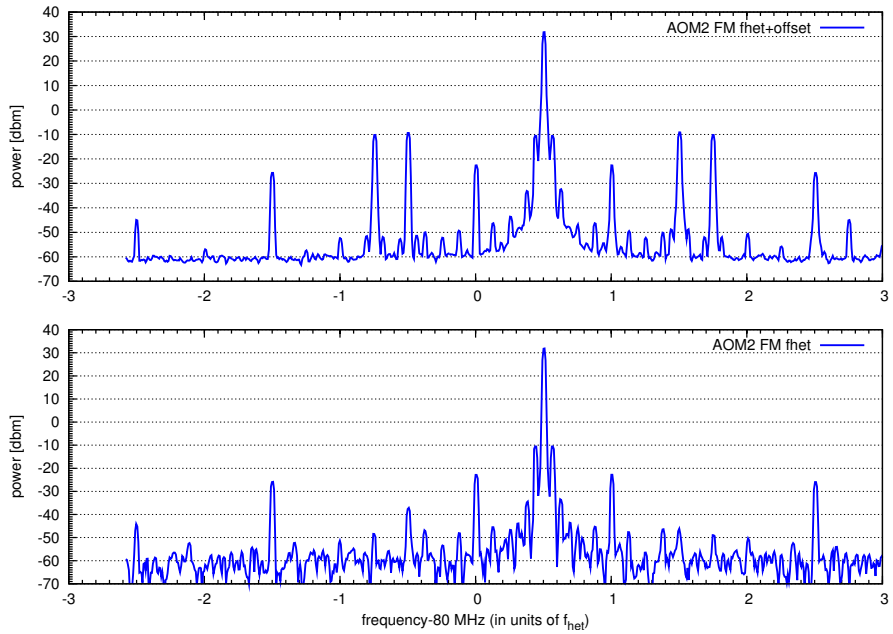

Figure 46: Spectra of AOM RF drive signal with FM added. Top: the extra sidebands induced by the FM are at a shifted frequency (to adjust their amplitude). Bottom: They are shifted to the correct frequency and cancel the naturally occuring sidebands. Note, however, that the second-order sidebands are unaffected.

In Figure 47 on the following page, an amplitude modulation (AM) at $f_{\rm het}$ was added to VCXO2 while VCXO1 and both power amplifiers were also running. When the amplitude and phase of the amplitude modulation were adjusted such as to minimize the first-order sidebands in the spectrum, only one of the first-order sidebands disappeared, while the other grew. This confirms the PM-character of the first-order sidebands. Again, the second-order sidebands are unaffected.

In Figure 48 on the next page, a frequency modulation (FM) at $f_{\rm het}$ was added to VCXO2 while VCXO1 and both power amplifiers were also running. In contrast to the previous measurement, here the amplitude and phase of the frequency modulation were adjusted such as to minimize the *second-order* sidebands in the spectrum. This should be possible if the second order sidebands were the J_2 sidebands associated with the FM/PM at $f_{\rm het}$, The results show, however, that (1) more power than is really present in the first order sidebands is needed to produce the observed level of second order sidebands and (2) even when the amplitude and phase of the FM/PM at $f_{\rm het}$ is adjusted such as to maximally suppress the second order sidebands, the second order sidebands are affected asymmetrically (one grows while the other disappears). This confirms the previous observation that they are not simply the J_2 sidebands associated with a FM/PM at $f_{\rm het}$, but have another origin.

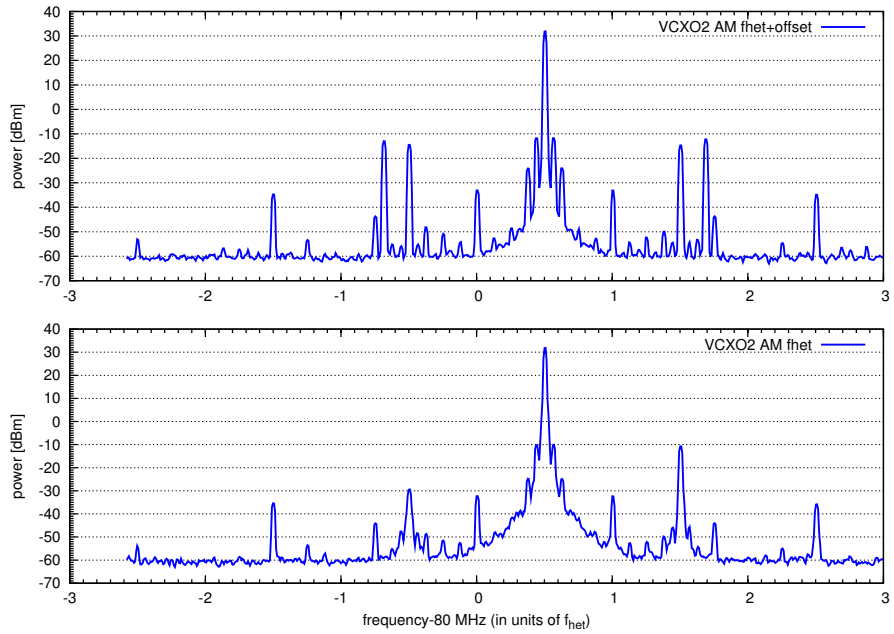

Figure 47: Spectra of AOM RF drive signal with AM added. Top: the extra sidebands induced by the AM are at a shifted frequency (to adjust their amplitude). Bottom: They are shifted to the correct frequency, but cancel only one of the naturally occuring sidebands, while the other one grows. Note, however, that the second-order sidebands are unaffected.

In Figure 49 on the following page, a frequency modulation (FM) at $2f_{\mathrm{het}}$ was added to VCXO2 while VCXO1 and both power amplifiers were also running. By adjusting amplitude and phase of the modulation, the second-order sidebands can be made to disappear. This indicates that they have PM character, although this PM is unrelated to the first-order sidebands.

It is interesting to note that in the very different experimental setup in Glasgow, sidebands were also observed, including second-order sidebands for which simple cross-coupling of 'the other' frequency provides no explanation.

Here is a description of the setup that was used in the interferometric preinvestigations in Glasgow:

The AOMs were made using TeO_2 cells by AA Opto-Electronique, model AA.MT.80/B20/A1 working at 1.064 μm. These were driven by two phase locked Agilent 8648A signal generators and Motorola CA2832C power amplifiers. The Motorola amplifiers were chosen for their low noise performance. They provide wideband linear amplification: 35.5 dB of gain from 1-200MHz with 1.6W maximum output power (ensuring they could not damage the AOMs which are rated to 2.5W rf input power).

The Motorola amps were very carefully shielded in cases, physically separated ($>$ 40 cm) and electrically isolated with RF chokes on input and output RF lines and on DC power lines.

We have used with very high quality RF cable in all the RF lines (Nexans Quickform 86, Farnell code 157260).

They power amplifiers were driven from the same power supply but had choked power lines. We did worry about the common power supply at one stage and drove the amps using separate battery packs (complete electrical isolation) but saw no change in performance.

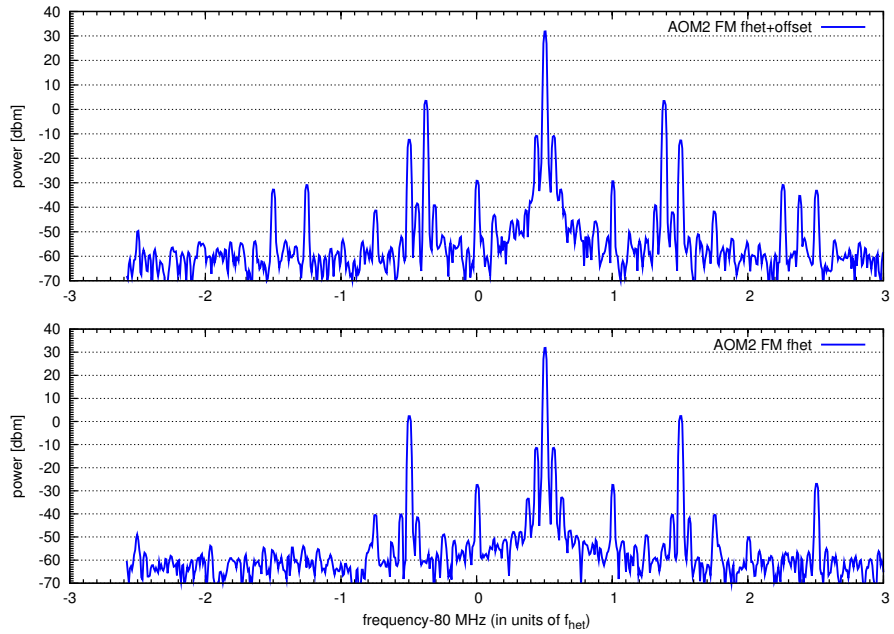

Figure 48: Spectra of AOM RF drive signal with FM added. Top: the extra sidebands induced by the FM are at a shifted frequency (to adjust their amplitude in an attempt to cancel the second-order sidebands by the J_2 components of FM at $f_{\rm het}$). Bottom: They are shifted to the correct frequency, but cancel only one of the second-order sidebands, while the other one grows.

We can summarize these findings as follows:

- The sidebands are created in the power amplifiers when these pick up RF at a frequency near (within a few kHz) of their operating frequency.
- Both first-order and second-order sidebands appear in pairs that have PM character (as opposed to AM).
- First- and second-order sidebands are not directly related; i.e. the second-order sidebands are not simply the J_2 terms associated with the first-order PM sidebands. Their amplitude is larger and they cannot be cancelled by either AM- or PM- first order sidebands.
- Since first-order PM sidebands have no effect on the phase measurement (see Section 3.2 on page 19), the second-order sidebands cause the largest error term.
- The appearance of the sidebands, in particular second-order sidebands, is no artefact of a singularily bad setup in Hannover, since they were also observed in a very different (and better shielded) setup in Glasgow.

9 Doppler-induced errors

The SBDFT method requires $f_{\rm het}$ to be exactly centered in one output bin of the DFT. Hence $f_{\rm het}$ and $f_{\rm samp}$ are coherently derived from one common master clock.

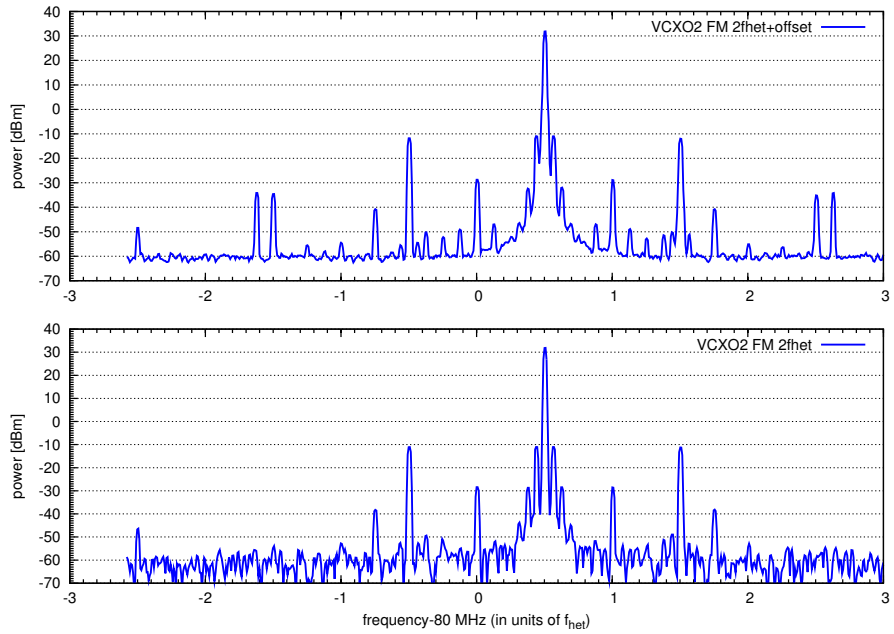

Figure 49: Spectra of AOM RF drive signal with added FM at $2f_{\rm het}$. Top: the extra sidebands induced by the FM are at a shifted frequency (to adjust their amplitude in an attempt to cancel the second-order sidebands by the J_2 components of FM at $f_{\rm het}$). Bottom: They are shifted to the correct frequency, but cancel only one of the second-order sidebands, while the other one grows.

Starting with a time series

$$x_j = \cos\left(\frac{2\,\pi\,(k+\delta)\,\left(j-\frac{n}{2}\right)}{n} - \phi\right), \tag{45}$$

where $n =$ NFFT, $k =$ bin, $\phi =$ true phase and. δ=frequency offset in bins (typically -0.5...0.5), and computing the SBDFT as

$$\mathrm{DFT} = \sum_{j=0}^{n-1} x_j\,\exp\left(2\,\pi\,\mathrm{i}\,k\,\frac{j}{n}\right), \tag{46}$$

we obtain the expected exact result for $\delta = 0$:

$$\mathrm{DFT}_0 = (-1)^k\,\frac{n}{2}\,e^{\,\mathrm{i}\,\phi}, \tag{47}$$

For $\delta \neq 0$, we get, however[10]:

$$\mathrm{DFT} = (-1)^k\,\frac{\left(e^{2\,\mathrm{i}\,\delta\,\pi}-1\right)\,\left(e^{\,\mathrm{i}\,\left(\phi+\frac{4\,(\delta+k)\,\pi}{n}\right)} - \cos(\phi) - \mathrm{i}\,\left(2\,e^{\frac{2\,\mathrm{i}\,\delta\,\pi}{n}}-1\right)\,\sin(\phi)\right)}{2\,e^{\,\mathrm{i}\,\delta\,\pi}\,\left(e^{\frac{2\,\mathrm{i}\,\delta\,\pi}{n}}-1\right)\,\left(e^{\frac{2\,\mathrm{i}\,(\delta+2\,k)\,\pi}{n}}-1\right)} \tag{48}$$

[10]The fact that there might be a problem was first pointed out by D. Summers (SEA). We use, however, different notation, formulae and remedies.

This error occurs only during fast phase shifts (such as caused by fast OPD fluctuations or fast test mass motion) and is **non accumulative**.

There are two effective remedies available:

9.1 Time-domain window function

Application of a time-domain window function to the digitized photocurrent effectively removes the error.

Figure 50 shows the worst-case phase error for several time-domain window functions (see Reference [5] for a detailed discussion of window functions). 'Worst-case' means the absolute maximum for all values of the true phase between 0 and $2\,\pi$ and all values of the doppler shift between -0.5 and $+0.5$ of the bin width.

The phasemeter SNR decreases by a few dB when a window is applied, depending on the window's effective noise bandwidth (ENBW).

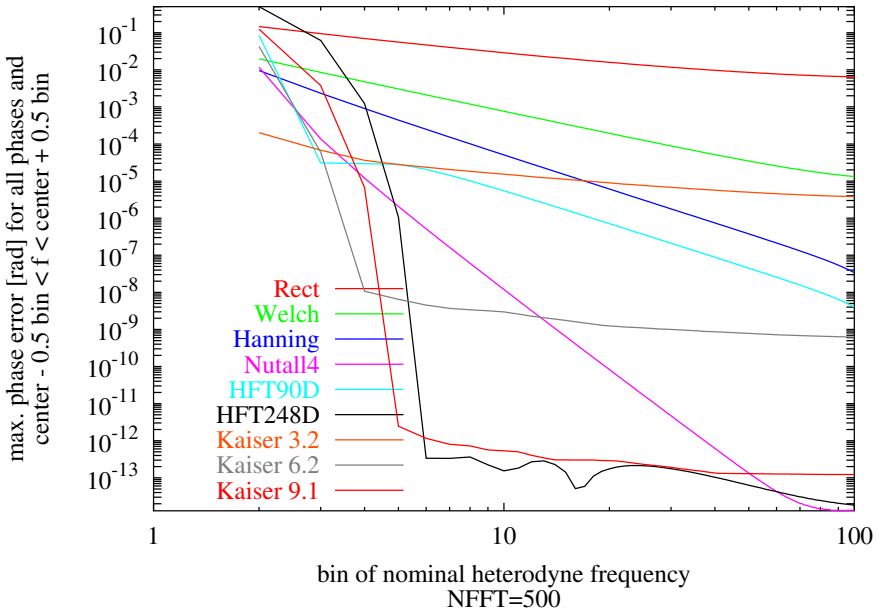

Figure 50: Worst-case Doppler-induced phase error with window functions.

9.2 Removal by subtraction

Since the error term is analytically known and depends only on the absolute value of the phase ϕ and the Doppler shift δ, both of which are directly measured (δ being the time derivative of ϕ), it can be removed by subtraction from the raw data.

This is the approach that we have taken for the case of raw data that were taken when the OPD was scanned with high velocity (Section 6.2.1 on page 41).

The procedure is as follows:

At first, a simple numerical approximation of the error term is determined. For that, the error $\Delta\phi$ is numerically computed on a grid of 50×50 points in the range $-\pi \leq \phi_{\text{true}} < \pi$ and $-0.5 \leq \delta < 0.5$. This error is saved in a table of the form

$$\phi_{\text{meas}},\ \delta,\ \Delta\phi \tag{49}$$

Figure 51 shows the result for the parameters that were used in our measurements (NFFT=24260, bin=50).

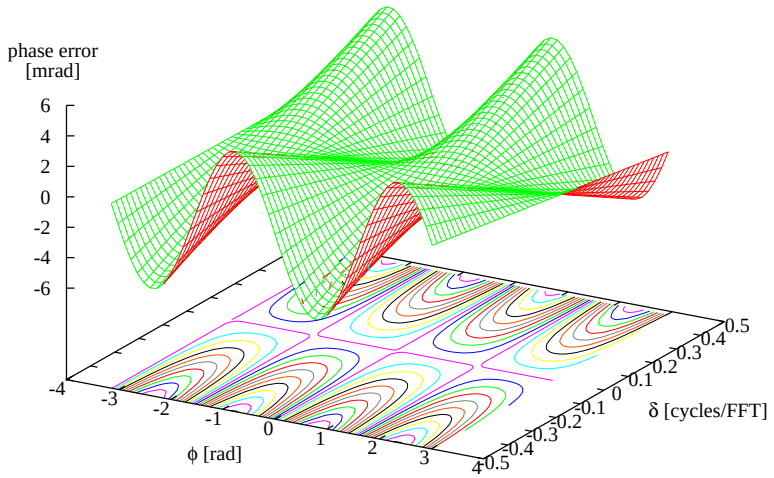

Figure 51: Doppler-induced phase error.

Next, the following simple model is fitted to these data:

$$\Delta\phi = \delta \times (a_0 + a_1 \sin(2\phi) + a_2 \cos(2\phi)), \tag{50}$$

using a_0, a_1 and a_2 as parameters. The results are:

$$\begin{aligned} a_0 &= -0.0001275 \pm 6.121 \cdot 10^{-7} = 0.4801\%, \\ a_1 &= 0.0100027 \pm 8.657 \cdot 10^{-7} = 0.008655\%, \\ a_2 &= -0.000127541 \pm 8.657 \cdot 10^{-7} = 0.6788\%. \end{aligned} \tag{51}$$

Figure 52 shows the residuals of this fit. The maximal error is reduced by a factor of more than 100 and even more for the relevant small values of δ.

This formula can now be applied to the 'raw phase' measurements from the phasemeter. Inputs to the formula are the *measured* raw phases (thanks to the way the table (49) was constructed, and the Doppler shift δ which is estimated from the raw phases as follows:

$$\delta_i = \frac{\phi_{i+1} - \phi_{i-1}}{4\pi}. \tag{52}$$

For all our purposes, this level of correction was sufficient. Indeed, a noticable effect of the Doppler correction appeared only when the OPD was scanned with high velocity (Section 6.2.1 on page 41). For 'real' mesurements with OPD stabilization, the Doppler induced noise was much smaller than other noise sources.

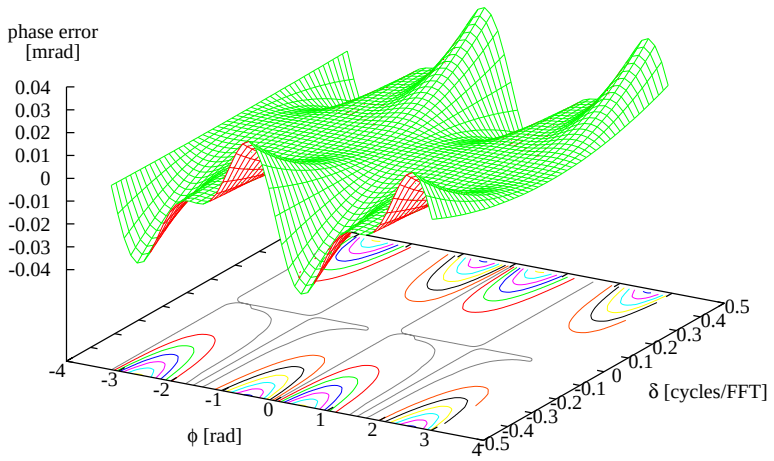

Figure 52: Residual Doppler-induced phase error after fit of a correction function.

The next level of correction uses the model

$$\Delta\phi = \delta \times (a_0 + a_1 \sin(2\phi) + a_2 \cos(2\phi)) + (\delta^2 + aa_5\delta) f_2(\phi), \tag{53}$$

with

$$f_2(\phi) = (aa_1 \sin(2\phi) + aa_2 \cos(2\phi) + aa_3 \sin(4\phi) + aa_4 \cos(4\phi)) \tag{54}$$

and the fitted parameters

```
a0  = -0.0001275   +/- 1.523e-09 (0.001195%)
a1  = 0.00999931   +/- 4.832e-09 (4.832e-05%)
a2  = -0.000127498 +/- 2.162e-09 (0.001696%)
aa1 = -0.000100011 +/- 5.573e-09 (0.005572%)
aa2 = 1.27521e-06  +/- 5.573e-09 (0.437%)
aa3 = -5.001e-05   +/- 5.573e-09 (0.01114%)
aa4 = 1.27553e-06  +/- 5.553e-09 (0.4353%)
aa5 = -0.00299281  +/- 4.321e-05 (1.444%)
```

The residuals of this fit are of only μrad amplitude, as shown in Figure 53.

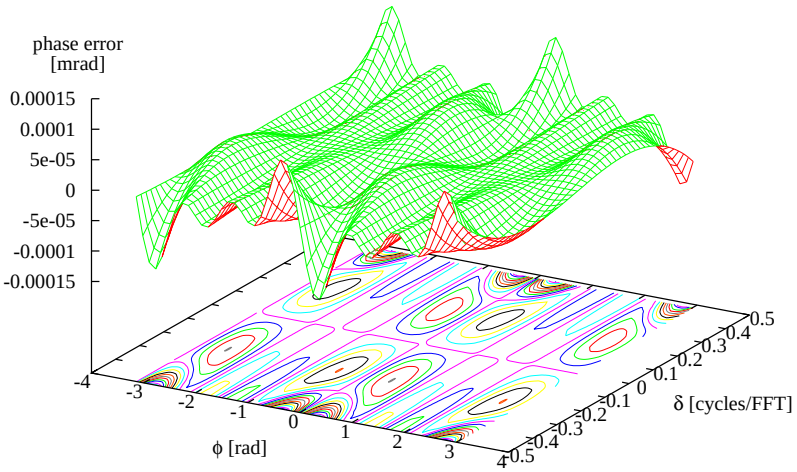

Figure 53: Residual Doppler-induced phase error after fit of a second-level correction function.

10 Mitigation

Several possibilities exist to mitigate the noise term described in this document. They will be treated one by one in this Section.

10.1 Reduce sidebands

Since it has been demonstrated that sidebands on the light cause this error to appear in the first place, the obvious remedy is to reduce these sidebands to a harmless level. The importance of reducing the sidebands has been recognized early in the study and is one of the most important outcomes of this study. The requirement specifications for the AOMU have been written accordingly.

Here is an extract from S2-ASD-RS-3007, Issue 1, 23.03.2005:

Req. AOMU-0080 / T:

Each optical output channel shall have high spectral purity as follows: For an unambiguous description, the properties of the spectrum are referred to the photocurrent produced when the optical output would be brought to interference with an perfect heterodyne optical local oscillator and converted to an electrical signal by an ideal photodiode. In this virtual electrical signal, all sidebands shown in Figure 4.1 shall be suppressed by at least -100 dBc (i.e. 10-5 in electrical amplitude). This includes in particular the frequency of the other channel. The single sideband noise floor shall be smaller than -120 dBc/Hz (i.e. 10-6/sqrt(Hz) in electrical amplitude) for frequency offsets between 500Hz and 5kHz from the carrier (see Figure 4.2). Note that this requirement covers both electrical and optical crosstalk effects.

Remarks:

The diagram 4.1 shows the desired output frequency in each beam (large arrow) and the unwanted sidebands (small arrows). The frequencies "80MHz" and "1kHz" are NOT fixed but are intended to represent the basic AOM driving frequency and the heterodyne frequency, respectively. f0 represents the laser frequency (many THz). Each of the small sidebands must be suppressed to a very high level (-100dBc/Hz). The noise floor in between the sidebands shall be < -120 *dBc/Hz (i.e. 10-6/sqrt(Hz)) for frequency offsets (from the carrier) between 500 Hz and 5 kHz (see fig. 4.2). "type A" sidebands are most likely to occur within one AOM by coupling of the un-diffracted (zeroorder) light and light of diffraction order -1 into the fiber coupler. "type B" sidebands could, for example, be generated by electrical crosstalk between the two RF frequencies (either in the RF driver or in the AOMs themselves), by AM or FM at the relevant frequencies (n*fhet) of the AOM driving signal, or by optical crosstalk between the two beams.*

The Figures "4.1" and "4.2" mentioned in the requirement are reproduced here in Figure 54 on the next page. Note that although one of the y-axes is labelled "RF power to AOM", the wording of the requirement refers to optical sidebands. According to Section 4 on page 21, it is no harm if the same requirement is applied to electrial sidebands instead, since these will produce optical sidebands typically a little smaller, but not larger, than their electrical counterparts.

10.2 OPD stabilization

The "free beam" implementation of the OPD stabilization has already been verified on the EM of the LTP interferometer and laboratory prototypes. This Section presents an actuator for an alternative implementation in which the absence of a free beam ensures the compatibility with an eventually fibre-coupled Modulation Bench of the LTP. The components were also selected with space qualifiability in mind.

10.2.1 Requirements on the actuator

The requirements to be fullfilled derive from the tests performed with the "free-beam" configuration and can be listed as follows:

- **Efficiency:** it must be possible to change the optical pathlength by about 30 μm.
- **Bandwidth:** The requirement calls for 20 Hz actuator bandwidth. This is sufficient for a loop bandwidth of a few Hz, which will be actually limited by phasemeter delays.
- **Spurious effects:** it is also important to investigate whether any other property of the laser beam apart from the optical pathlength is modified by the actuator. Although we could measure such effects with our very sensitive equipment, the effects are small and of no practical impact.

10.2.2 Description of the actuator

The actuator consists of a single mode, polarization maintaining **optical fibre** glued (using two components epoxy glue) around a PZT. The **ceramic ring PZT** is a cylinder of about 10 cm external diameter, 9 cm internal diameter and 3 cm height. It has an internal capacitance of 22 nF. The control voltage is applied to each electrode of the PZT via a 50 kΩ resistance using

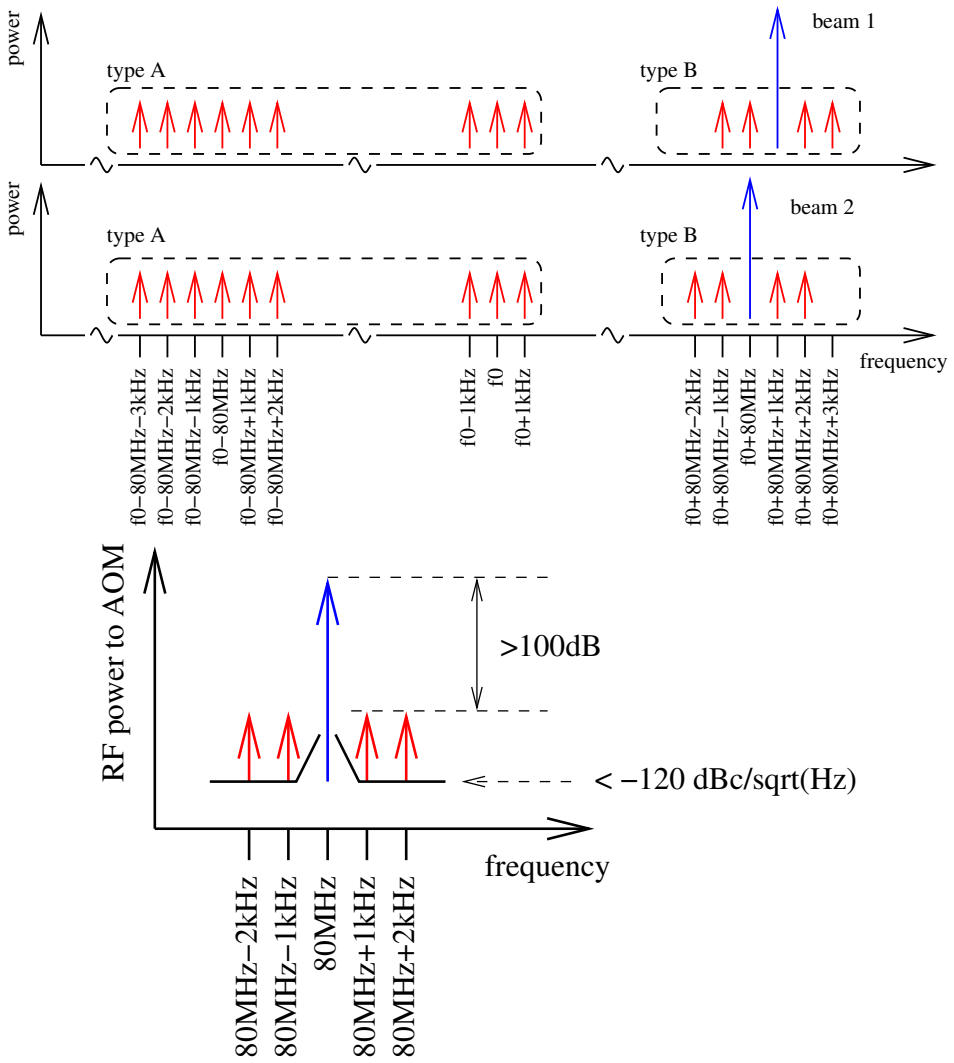

Figure 54: Figures from AOMU requirement specification.

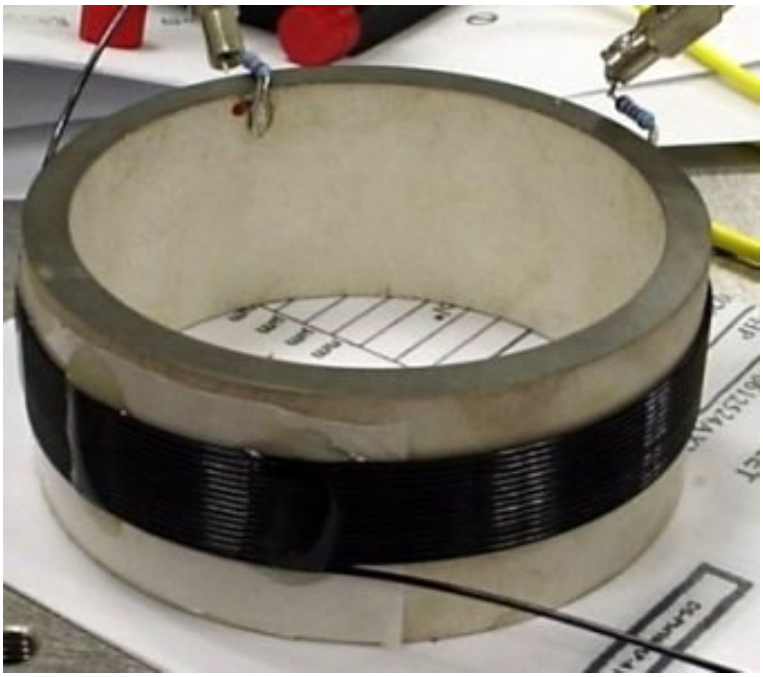

a driver with a dynamical range of ±400 V. Stress induced by the PZT on the fibre changes the optical pathlength undergone by the light.

10.2.3 Test bench 1: Efficiency and bandwidth

A homodyne Mach-Zehnder interferometer was built to test the efficiency of the actuator. The signal measured by a photodiode placed at one output port of such an interferometer is

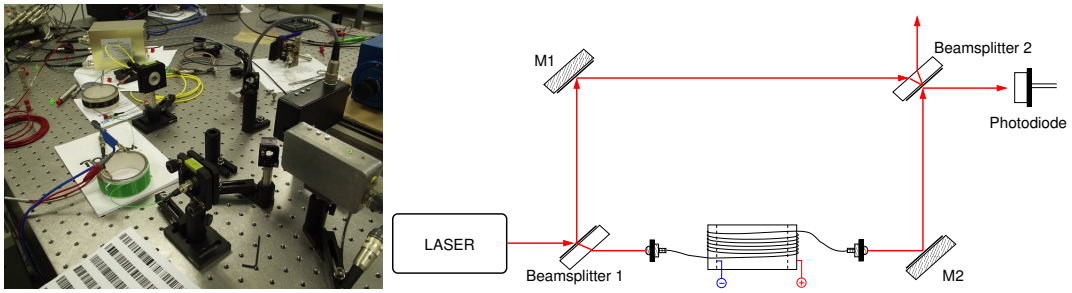

Figure 55: Table top homodyne interferometer to measure the efficiency and bandwidth of the actuator.

proportional to the light intensity and can be written as:

$$V_{PD} = A\left(1 + c \cdot \cos\left(\frac{2\pi\Delta s}{\lambda}\right)\right) \tag{55}$$

where c is the contrast of the interference, Δs the optical pathlength difference between the two arms of the interferometer and λ the wavelength of the laser, 1064 nm in our case. By applying a ramp to the PZT placed in one arm of the interferometer one can change the pathlength of the fibre. For each 1064 nm pathlength difference the intensity at the output of the interferometer will go through one full cycle (fringe).

Figure 56 shows the result of such a measurement from which the efficiency of our actuator can be estimated as η=0.17 μm/V_{PZT}. In order to test the reproducibility of the results, three different devices were built using PZTs with identical properties. The fibres were also identical but one of them was 4 m long and the other two 7 m. The glue used was also always the same but in different quantities, the shorter fibre being only glued with three strip-like contact surfaces and the longer fibres with more homogenous glue distributions. Nevertheless, all the three actuators behaved very similarly and showed a very comparable efficiency per meter of fibre. Using the whole range of the driver, the 4 m long fibre accomplishes about 24 μm and the 7 m long about 43 μm pathlength change.

To measure the bandwidth of the actuator the homodyne interferometer was locked to mid-fringe. This stabilization works in the same way as the OPD except that no heterodyne phase detection has to be done, which simplifies the test bench. It keeps the interferometer output in the linear region of the sinus function in Equation 55 on the preceding page. This allows the injection of perturbation signals to measure the transfer function of the actuator, as described in Figure 57 on the next page. The transfer function is measured as the quotient between the error signal V_{error} and the feedback signal V_{feedback} plus the perturbation V_{source}. Although this measurement configuration shows a poor signal to noise ratio at low frequencies, it delivers directly the transfer function and is thus more reliable than only dividing by the injected perturbation. Figure 58 on the preceding page shows the measured transfer function together with a fit that has been done to the data. This fit allows the quantification of the main characteristics of the function, which in this case are a simple pole at about 130 Hz and a complex pole at 15 kHz with a quality factor Q of 356. The first pole accounts for the low pass behavior and has its origin in the RC combination of the internal capacitance of the PZT (22 nF) and the series resistor used to apply the voltage (50 kΩ). The corner frequency of this RC element is 144 Hz, very similar to the fitted 130 Hz. This means that this first pole is no fundamental limitation for the bandwidth of the actuator, which is anyway already sufficient for the requirements of the OPD stabilization. The complex pole accounts for the mechanical resonance of the PZT. This is far enough from the interesting frequency range, so that its influence in the stabilization can be easily suppressed by a proper servo design which lets the

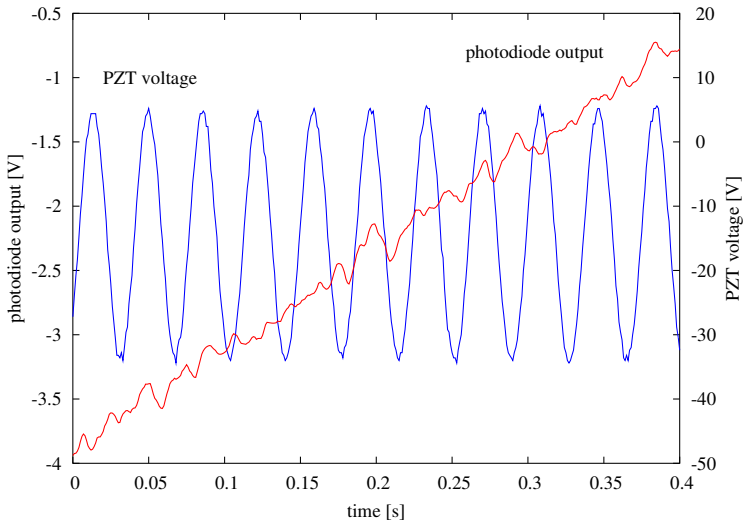

Figure 56: Efficiency of the cylindrical PZT actuator. Each fringe corresponds to $\lambda = 1064$ nm change in the pathlength.

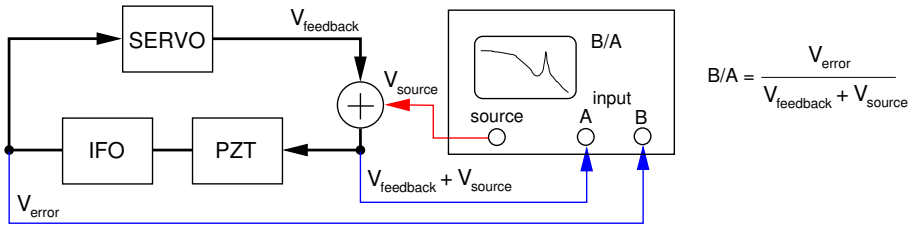

Figure 57: Experimental procedure for the measurement of the transfer function.

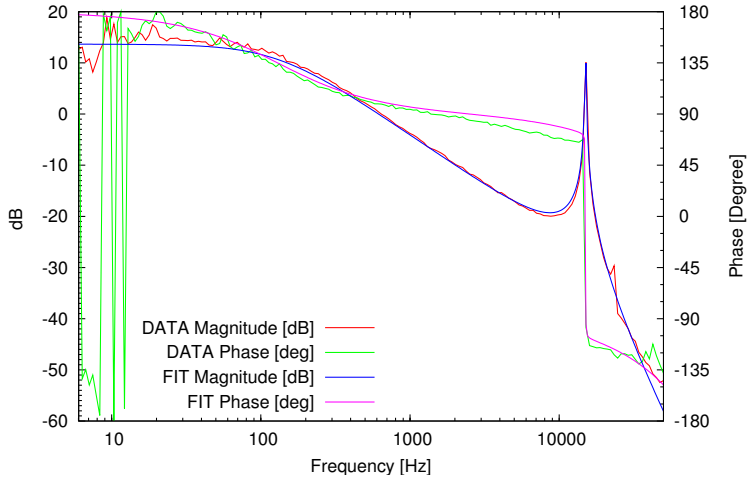

Figure 58: Transfer function of the cylindrical PZT actuator. The low pass behavior is given by the combination of 22 nF internal capacitance of the PZT and the 50 kΩ serial resistance used to apply the voltage.

gain roll off strongly after the unity gain frequency.

10.2.4 Test bench 2: Unwanted effects

Intrinsic amplitude modulation For this measurement laser light of constant power is coupled into the fibre and measured with a photodiode at the output without any other devices. The PZT voltage is modulated to check for a possible variation of the fibre transmission, which was not measurable.

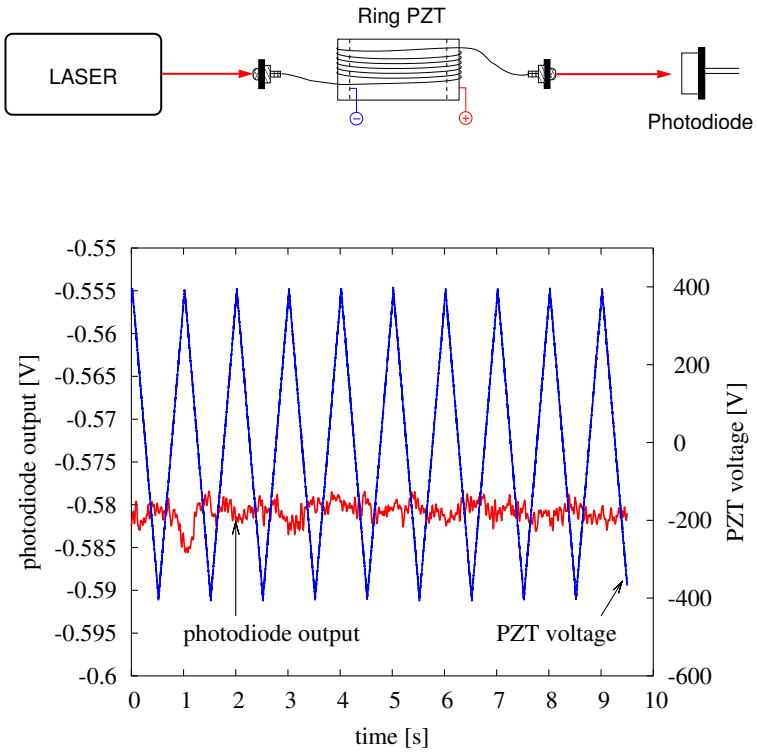

Figure 59: Transmittance of the fibre against control voltage applied to the PZT. No measurable influence.

Rotation of the polarization plane and elliplical polarization The question to be answered now is whether the stress induced in the fibre by the PZT changes the polarization of the propagating light. The direct consequence of a change in the polarization would be an amplitude modulation on the light injected into the optical bench due to the polarizers present just after the fibre injectors. This amplitude modulation can be then corrected by the amplitude stabilization which is already foreseen but a quantification of the effect needs to be done. For this purpose, the experimental setup shown in Figure 60 was implemented. The laser beam goes through a Polarising Beam Splitter (PBS) before it is coupled into the actuated fiber. Another PBS is placed at the output, which can be rotated by means of a stepper motor. The angle of rotation can also be very precisely measured and each time the second PBS rotates by 180 degrees a minimum in the transmitted light occurs, whose value has to be zero in the ideal case of linearly polarized outcoming light.

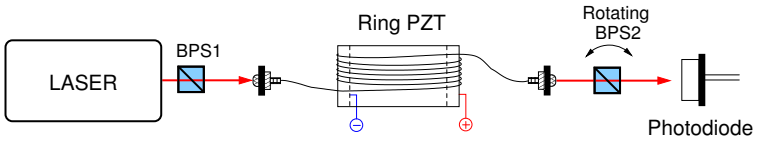

Figure 60: Experimental set-up for detection of changes in the polarization state of propagating light. PBS2 rotates while the control voltage at the PZT is modulated.

By measuring the angle of occurrence of these minima and their extinction ratio at different control voltages, as shown in Figure 61, we can derive the influence of the actuator on the polarization state of the light: if the polarization plane changes, the angle at which the minimum takes place will also change and appearance of circular polarization will make the minima different from zero.

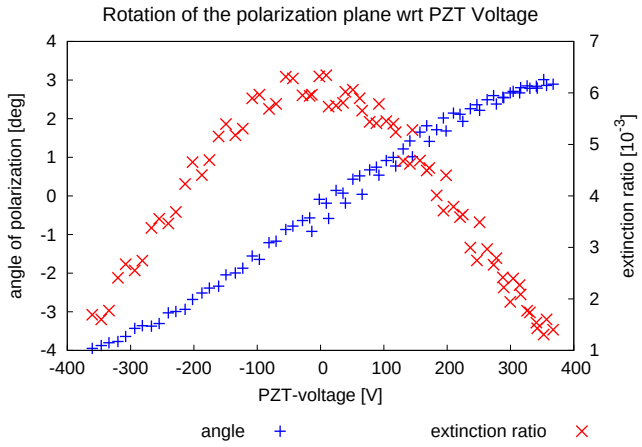

Figure 61: Rotation of the polarization plane and appearance of circular polarization at different control voltages.

There is a rotation of the polarization plane of about 7 degrees along the 800 V dynamical range of the driver. This would mean a change of 1.5 % in the intensity injected in the LTP optical bench, which could be easily compensated by the amplitude stabilization. It has to be observed, that using one of the 7 m long fibres in each arm, the requirement of 30 μm pathlength change would be fullfilled with less than half of the dynamical range of the used driver.

On the other hand, there is a strange behavior of the extinction ratio, which seems to be better when voltage is applied than when not, contrarily to our expectations.

An explanation for this can be found in the construction properties of the used fibres, which are worth being investigated due to their similarity to the ones planned for the LTP.

The principle of function of the polarization maintaining optical fibres is based on the birefringence shown by the core of the fibre. The two axes of propagation of the core have their origin in the stress inducing structures to be found in the cladding, and as can be seen in the section of a fibre shown in Figure 62, linear polarized light coupled into the slow axis of the fibre maintains its polarization and is also less sensitive to environmental stress.

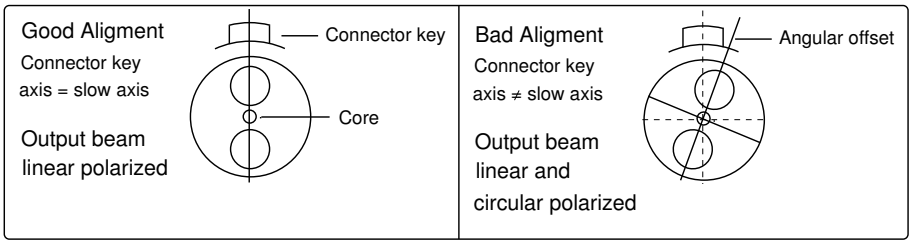

Figure 62: Alignment of a polarization maintaining fibre. Light coupled into the slow axis of the fibre propagates optimally. [Image from Schäfter-Kirchhoff].

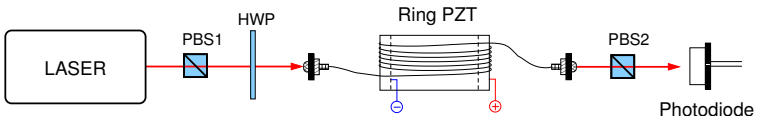

Figure 63: Experimental set-up to study the misaligning of the polarization plane of incoming light and the slow axes of the fibre. Maintaining a fixed alignment configuration, variations in the transmittance of the fibre are monitored while the control voltage is modulated.

The experimental set-up shown in Figure 63 on the preceding page was used to study the effect of an offset angle between the polarization plane of the incoming light and the slow axes of the fibre. It includes a Half Wave Platte (HWP) after the first polarizer, which makes it possible to change the incoming polarization plane without changing the transmitted amplitude or the beam position (which would change the coupling efficiency), as a PBS would do.

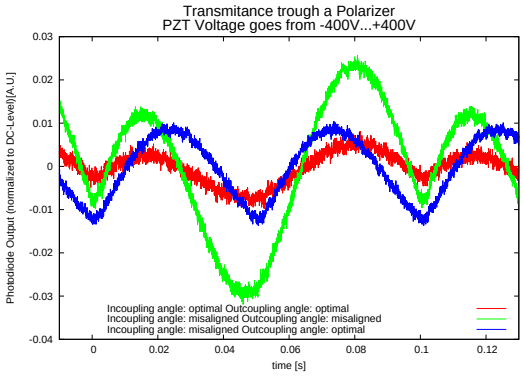

Figure 64: Normalized changes in the transmittance of the fibre as the control voltage is modulated for three different configurations of PBS1 and PBS2.

Figure 64 shows the fluctuations in the transmittance of the fibre, calculated as the changes in the output of the photodiode normalized to the mean intensity.

- The first curve shows the optimal configuration in which the transmittance variations are minimal. The HWP makes the incoming polarization plane parallel to the slow axes of the fibre and PBS2 is aligned with the outcoming polarization.

- For the second curve, the HWP is slightly rotated so that the angular offset described in Figure 62 on the previous page appears and the fluctuations increase.
- For the third curve PBS2 is optimized so that the fluctuations are again minimal, but due to the persistent misalignment of the HWP, they are not as small as in the first curve.

The exact location of the minima with respect to the control voltage also change in the different configurations, which explains the strange behavior observed in Figure 61 on page 70.

As a conclusion it can be said the observed effects, which have been measured under worse conditions than the ones expected for the LTP, could be easily compensated by the amplitude stabilization present on the optical bench.

Additionally, we have experimentally confirmed that when coupling a laser beam into polarization maintaining fibres special care must be taken in aligning the polarization plane of the light parallel to the slow axes of the fibre. A proper alignment ensures polarization conservation and reduces the influence of mechanical stress in the beam propagation.

In our experiments, we have used both the cylindrical PZT described above and a linear PZT, with equal results. The servo loop to stabilize the OPD fluctuations is described in Section 12 on page 84, since it is built very similar to the frequency stabilization servo loop.

10.3 Remove by calculation

The total error due to all sidebands can be written in general form as

$$\begin{aligned}\delta\varphi = &\left\{\alpha_1 \sin\left(\frac{\varphi_\mathrm{M}+\varphi_\mathrm{R}}{2}\right) + \alpha_2 \cos\left(\frac{\varphi_\mathrm{M}+\varphi_\mathrm{R}}{2}\right)\right\} \cdot \sin\left(\frac{\varphi_\mathrm{M}-\varphi_\mathrm{R}}{2}\right) \\ &+ \{\alpha_3 \sin(\varphi_\mathrm{M}+\varphi_\mathrm{R}) + \alpha_4 \cos(\varphi_\mathrm{M}+\varphi_\mathrm{R})\} \cdot \sin(\varphi_\mathrm{M}-\varphi_\mathrm{R}) \end{aligned} \tag{56}$$

with real constants $\alpha_1 \ldots \alpha_4$, which depend on the amplitudes and phases of the disturbing sidebands. If these constants can be determined for a measurement run, the error depends only on the two variables φ_M and φ_R, both of which are primary observables and are recorded. Hence one expects to be able to compute the error and subtract it from the data to obtain an improved data stream with less noise.

We have performed this procedure and have indeed reduced the noise. We do not, however, advocate this procedure as baseline for reasons that will be clear at the end of this section.

The problem lies in determining the coefficients $\alpha_1 \ldots \alpha_4$, which needs to be done with reasonable precision in order to achieve a useful noise reduction. For the purpose of this discussion, the phasemeter output consists of only two variables: φ_M and φ_R, which are given by

$$\begin{aligned}\varphi_R &= \Delta_F + \Delta_R, \\ \varphi_M &= \Delta_F + \Delta_M. \end{aligned} \tag{57}$$

The main interferometer output that represents the pathlength variation on the OB to be measured is given by:

$$\varphi = \varphi_R - \varphi_M. \tag{58}$$

Typically, $\varphi_R - \varphi_M$ varies only slowly. In a typical laboratory measurement, its variation is caused by thermal or other slow drifts and spans several radians. In orbit, $\varphi_R - \varphi_M$ represents the real motion of the test masses with respect to the optical bench or each other, and no

assumptions can be made in general about its behaviour, other than the variations will be slow[11].

The 'raw phases' φ_{M} and φ_{R}, on the other hand, vary rapidly thanks to Δ_F.

We can write the main output as

$$\varphi(t) = \varphi_R(t) - \varphi_M(t) = \varphi_{\mathrm{real}}(t) + \delta\varphi(\alpha_1 \ldots \alpha_4, \varphi_R, \varphi_M). \tag{59}$$

In order to obtain a reliable estimation of the coefficients $\alpha_1 \ldots \alpha_4$, a data set is necessary that covers a significant fraction of the two-dimensional parameter space given by

$$\begin{aligned} 0 <& \Delta_F < 2\pi, \\ 0 <& \varphi = \varphi_R - \varphi_M < 2\pi. \end{aligned} \tag{60}$$

We have developed fitting algorithms both in the time domain and in the frequency domain. They will be discussed in the next sections.

10.3.1 Time domain fitting

Starting from Equations (59) and (56 on the previous page), the principle is to fit this model to the measured data, which consists of φ_R, φ_M (and $\varphi = \varphi_R - \varphi_M$). The model is linear in the unknown coefficients $\alpha_1 \ldots \alpha_4$, which helps. However, the 'base functions' are not mutually orthogonal, and nothing is known a priori about $\varphi_{\mathrm{real}}(t)$. Hence a fit can only succeed if it includes all terms in Equations (59) and (56).

Keeping in mind that the error term which we want to fit is of only mrad magnitude, while we need $\approx 2\pi$ rad variation of the phases (Equation 60 on page 73), we need to model $\varphi_{\mathrm{real}}(t)$ to better than mrad precision for the fit to be successful.

Using data sets measured during the test campaign at TNO, we have hence developed a two-stage segmented fit procedure that works as follows:

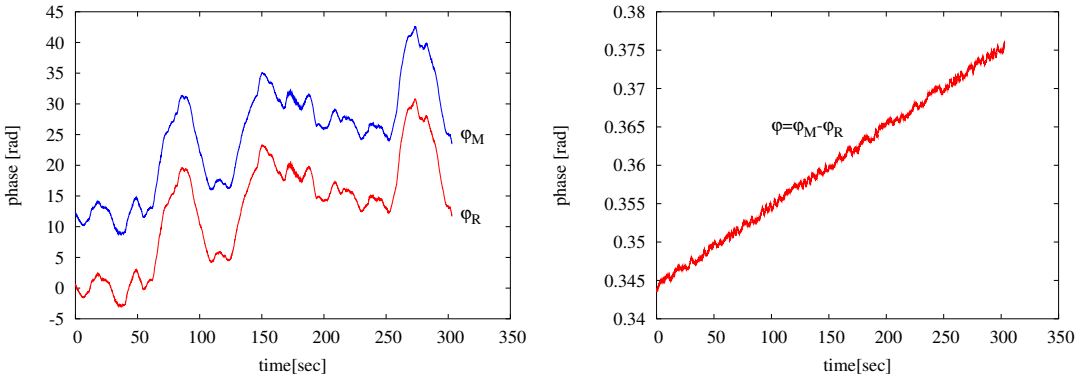

The error term that we want to decompose is much smaller than the natural fluctuation of $\varphi = \varphi_R - \varphi_M$.

[11] The purpose of the LTP interferometer is to monitor the test masses in a variety of operational modes. In some modes, the interferometer signal will be used as error signal for the DFACS controller and will thus be kept nearly constant, while in other modes the test masses are allowed to drift.

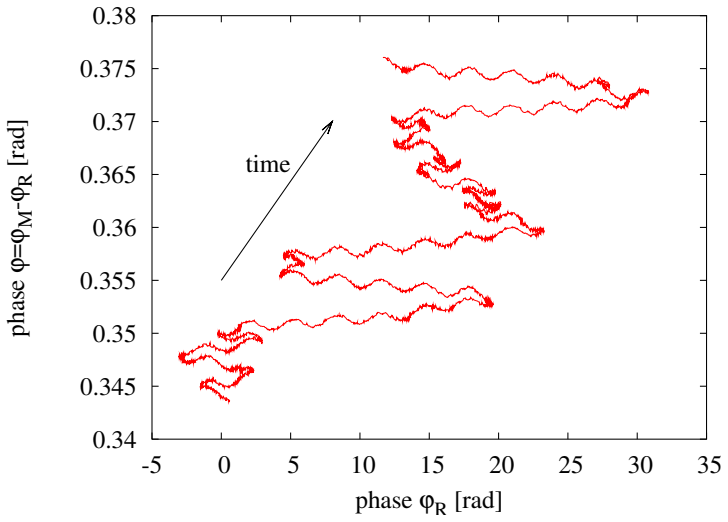

In this plot of $\varphi = \varphi_R - \varphi_M$ against φ_R the $\sin(2\Delta_F)$ term can be clearly seen. However, the natural fluctuation of $\varphi = \varphi_R - \varphi_M$ is still dominant and has no simple φ_R dependence.

The data is be split into segments of a few thousand points (a few minutes).

The requirements on the size of each segment are:

- The segment must be **long enough** such that φ_R (or Δ_F) varies by at least 2π.
- The segment must be **short enough** such that $\varphi(t) = \varphi_R - \varphi_M$ is nearly constant and can be described by a simple model (e.g. a polynomial in t). The deviation from the model must be smaller than the error term we want to decompose.

Each segment is fitted to the model:

$$\begin{aligned} &\varphi = a_0 + a_1 \cdot t + a_2 \cdot t^2 + \quad \text{natural evolution of} \varphi \\ &\quad b_0 \sin(\varphi_R + \varphi_M) + b_1 \cos(\varphi_R + \varphi_M) + \quad \text{second-order error term} \\ &\quad c_0 \sin((\varphi_R + \varphi_M)/2) + c_1 \cos((\varphi_R + \varphi_M)/2). \quad \text{first-order error term} \end{aligned} \tag{61}$$

The model is linear and the fit can hence be performed with deterministic algorithms (inversion of the design matrix by Cholesky decomposition in 80-bit "long double" arithmetic). This requires ≈ 100 FLOPS per data point.

Typical result from one segment are shown in Figure 65.

In the previous steps, we have obtained many estimates of

$$b_0 = \alpha_1 \cdot \sin\left(\frac{\varphi_\mathrm{M} - \varphi_\mathrm{R}}{2}\right)$$

$$b_1 = \alpha_2 \cdot \sin\left(\frac{\varphi_\mathrm{M} - \varphi_\mathrm{R}}{2}\right)$$

$$c_0 = \alpha_3 \cdot \sin\left(\varphi_\mathrm{M} - \varphi_\mathrm{R}\right) \tag{62}$$

$$c_1 = \alpha_4 \cdot \sin\left(\varphi_\mathrm{M} - \varphi_\mathrm{R}\right) \tag{63}$$

for segments with nearly constant $\varphi_\mathrm{M} - \varphi_\mathrm{R}$.

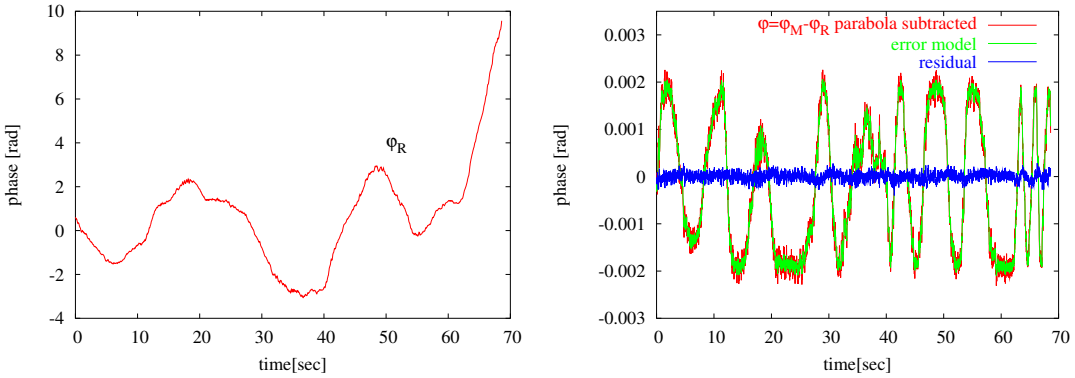

Figure 65: Typical result from the first step of the time-domain fitting algorithm.

If the complete time series is long enough to cover a variation $> 2\pi$ of $\varphi_M - \varphi_R$, these many estimates can be fitted once more to obtain $\alpha_1 \ldots \alpha_4$:

Figure 66 on the next page shows a typical result from that second fit procedure .

Finally, the error can be subtracted from the complete time series. The results from the early TNO data are shown in Figures 67 on the following page and 68.

We have also tried to apply this correction algorithm to further improve data that were taken with the OPD stabilization working. For this measurement, the sequence was as follows:

1. First, the OPD was scanned by several fringes with a rate of a few fringes per second. Simultaneously, a heater on the mirror mount was activated such that φ slowly varied over more than one fringe.
2. Then, without changing anything else, the OPD scan was stopped and the OPD stabilization activated instead. This measurement was kept running over night.
3. The next morning, OPD scan and heating was repeated.
4. From the first and last segments, the coefficients were obtained using the time-domain fitting algorithm as described above.
5. A quiet segment from the middle of the night was chosen, where the effect of the heating was gone and the environmental noise in the lab was low.
6. The coefficients found from the fit were used to compute and subtract the remaining error in the time domain.

The parameters obtained from the fit were:

```
a1 = 7.11203e-05   +/- 2.811e-06  (3.953%)
b1 = 1.0977e-06    +/- 2.604e-06  (237.2%)
c1 = 3.16995e-06   +/- 1.913e-06  (60.34%)

a2 = -0.00141993   +/- 2.349e-06  (0.1655%)
b2 = -4.46629e-06  +/- 2.176e-06  (48.72%)
c2 = 2.36105e-06   +/- 1.598e-06  (67.67%)
```

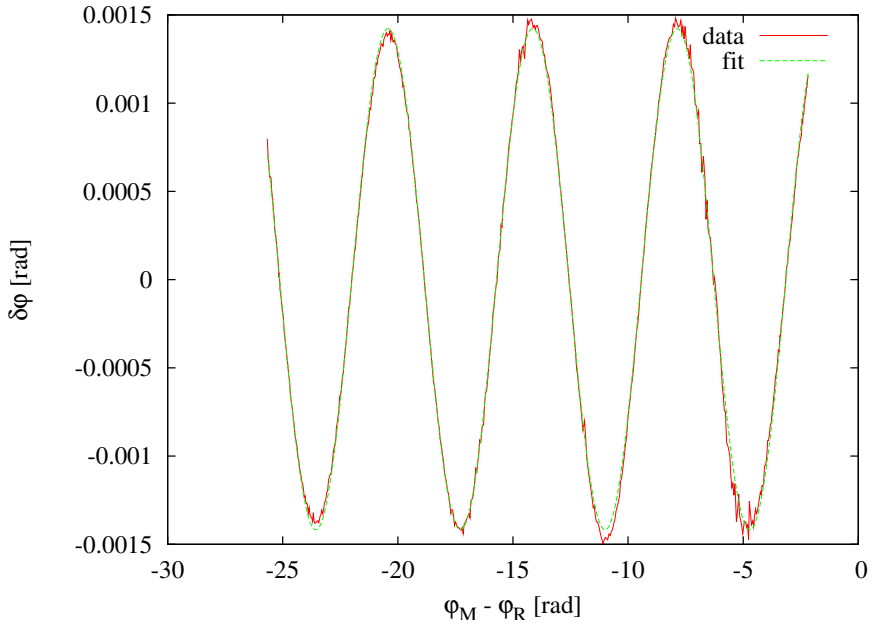

Figure 66: Result from the second step of the time-domain fitting algorithm. In this case, α_3 was determined from many measurements of $c_0 = \alpha_3 \cdot \sin(\varphi_M - \varphi_R)$, which were derived from the first step of the fitting algorithm.

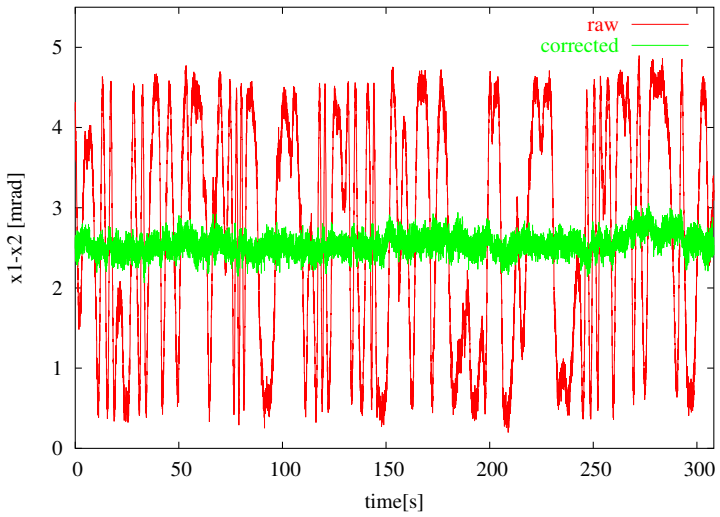

Figure 67: TNO data with error term subtracted.

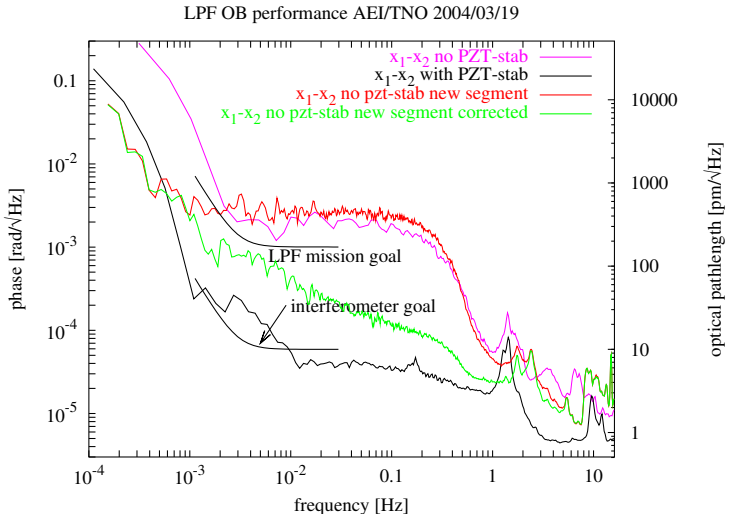

Figure 68: Spectrum of TNO data with error term subtracted. See also Figure 69 on the next page.

```
a3 = -0.000141441   +/- 2.414e-06   (1.707%)
b3 = -6.63734e-06   +/- 2.489e-06   (37.51%)
c3 = -3.17421e-06   +/- 1.738e-06   (54.76%)

a4 = -5.48522e-05   +/- 1.919e-06   (3.499%)
b4 = -1.40612e-05   +/- 1.973e-06   (14.03%)
c4 = 2.38268e-06    +/- 1.38e-06    (57.92%)
```

They are expressed in radians and correspond to the following components of the error term: `a1`, `a2`, `a3` and `a4` are the required parameters $\alpha_1, \alpha_2, \alpha_3$ and α_4.

`b1`, `b2`, `b3` and `b4` were experimentally included in the fit to determine possible contributions of the form

$$\left\{\beta_1 \sin\left(\frac{\varphi_\mathrm{M}+\varphi_\mathrm{R}}{2}\right) + \beta_2 \cos\left(\frac{\varphi_\mathrm{M}+\varphi_\mathrm{R}}{2}\right)\right\} \cdot \cos\left(\frac{\varphi_\mathrm{M}-\varphi_\mathrm{R}}{2}\right) + \left\{\beta_3 \sin(\varphi_\mathrm{M}+\varphi_\mathrm{R}) + \beta_4 \cos(\varphi_\mathrm{M}+\varphi_\mathrm{R})\right\} \cdot \cos(\varphi_\mathrm{M}-\varphi_\mathrm{R}), \tag{64}$$

which have no theoretical justification from the calculations presented in Section 3 on page 14. The result from the fit shows that they have indeed only negligible amplitudes.

`c1`, `c2`, `c3` and `c4` were experimentally included in the fit to determine possible contributions of the form

$$\left\{\gamma_1 \sin\left(\frac{\varphi_\mathrm{M}+\varphi_\mathrm{R}}{2}\right) + \gamma_2 \cos\left(\frac{\varphi_\mathrm{M}+\varphi_\mathrm{R}}{2}\right)\right\} + \left\{\gamma_3 \sin(\varphi_\mathrm{M}+\varphi_\mathrm{R}) + \gamma_4 \cos(\varphi_\mathrm{M}+\varphi_\mathrm{R})\right\}, \tag{65}$$

which neither have a theoretical justification from the calculations presented in Section 3 on page 14. The result from the fit shows that they have indeed only negligible amplitudes, too.

Using the parameters thus found, the error term was computed in the time domain and subtracted from the φ measurement.

Figure 69 on the preceding page shows a typical result of such a subtraction, indicating that when the OPD stabilization is active the sideband-error is already reduced well below the noise from other sources, such that the fit does not improve the noise any further.

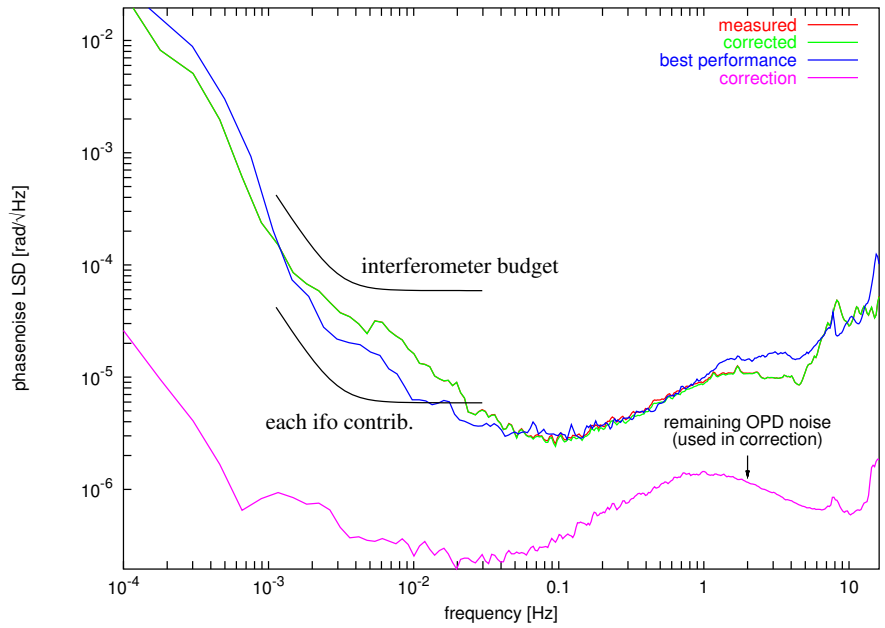

Figure 69: Spectrum of x_1 measurements with OPD stabilization working. From top to bottom (at 10^{-2} Hz): The measurement that was corrected, (indistinguishable) the corrected spectrum, the best spectrum, and the spectrum of the correction that was applied.

We can summarize the time-domain fitting procedure as follows:

- When the OPD is not stabilized, fitting and subtracting the error term removes a part of the noise, but the remaining noise level is still higher than with OPD stabilization.
- This confirms the findings of many previous experiments: It is always better to remove a noise term than to subtract it from the data. The latter rarely achieves more than a factor 10 in noise reduction.
- The algorithm to determine the noise coefficients requires both the raw data and considerable computational power and is hence impractical for LTP.
- It cannot be predicted whether the requirements on the segment length and phase excursions in one segment would be met in orbit. In the worst case the OPD fluctuations would be large enough to spoil the noise but not sufficient for a fit of the noise coefficients.
- The requirements could be met with an OPD actuator; but if we have the acuator, we have a better way of using it!
- When the OPD is stabilized, the remaining error caused by modelled sidebands is smaller than other noise sources, and in any case much smaller than the interferometry requirement, such that the complicated fitting procedure is not worth the effort.

10.3.2 Frequeny-domain fitting

We have also developed a novel algorithm to determine the unknown coefficients in the frequency domain.

The time series of the main data stream φ as well as those of the signals with which correlations are sought, are subjected to a single long FFT. A time-domain window can optionally be applied to reduce spectral leakage.

A linear fit (see Section C on page 98) is then performed in the frequency domain (using the complex Fourier coefficients), aiming at minimizing the weighted RMS spectrum *in the frequency range of interest*. Some possibilities to choose weights include uniform weighting (emphasizing those spectral components with the largest absoulte value) or "relative weighting", where one sets $w_i = 1/|y_i|^2$. The effect is that the relative error in all data points contributes equally to the χ^2 function, independent of the absolute value of the data point. With this approach, the difference between 10 and 11 counts as much as the difference between 0.01 and 0.011, or, in other words, a quotient expressed in dB counts always the same, independent of the absolute value of the data point.

The resulting coefficients are then applied *in the time domain* to subtract corresponding fractions of each signal from the main data stream φ.

This method has to be used with care. We were surprised to find enormous "improvements in the noise" (Figure 70) for some parameters.

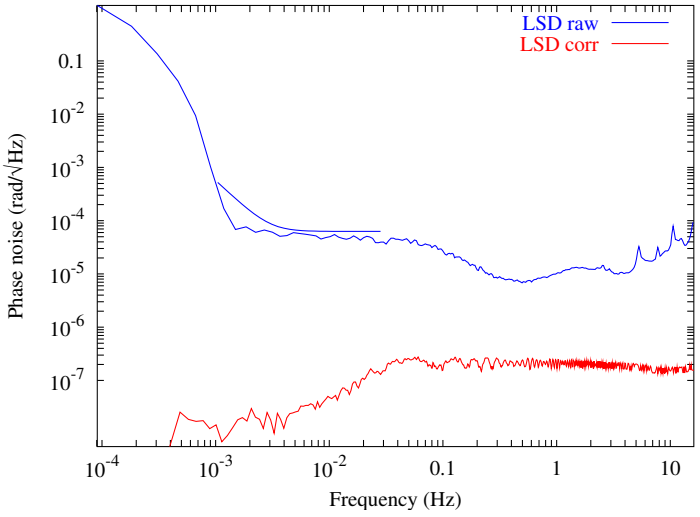

Figure 70: Frequency-domain fit when only a small range of $0 \ldots 2\pi$ is spanned by φ. The result is **not a meaningful noise curve!**

We soon found out the reason: when the data stream φ spans only a small range of $0 \ldots 2\pi$, it is possible to construct linear combinations from the base functions (56 on page 72) that look like $\varphi = \varphi_{\mathrm{M}} - \varphi_{\mathrm{R}}$ in that range. Subtracting that linear combination effectively subtracts the signal, producing meaningless results.

This is illustrated in Figure 71 on page 80.

Figure 72 on the previous page shows the noise curves of the x_1 interferometer and the remaining contribution of the second-order sidebands. The parameters of the frequency-domain

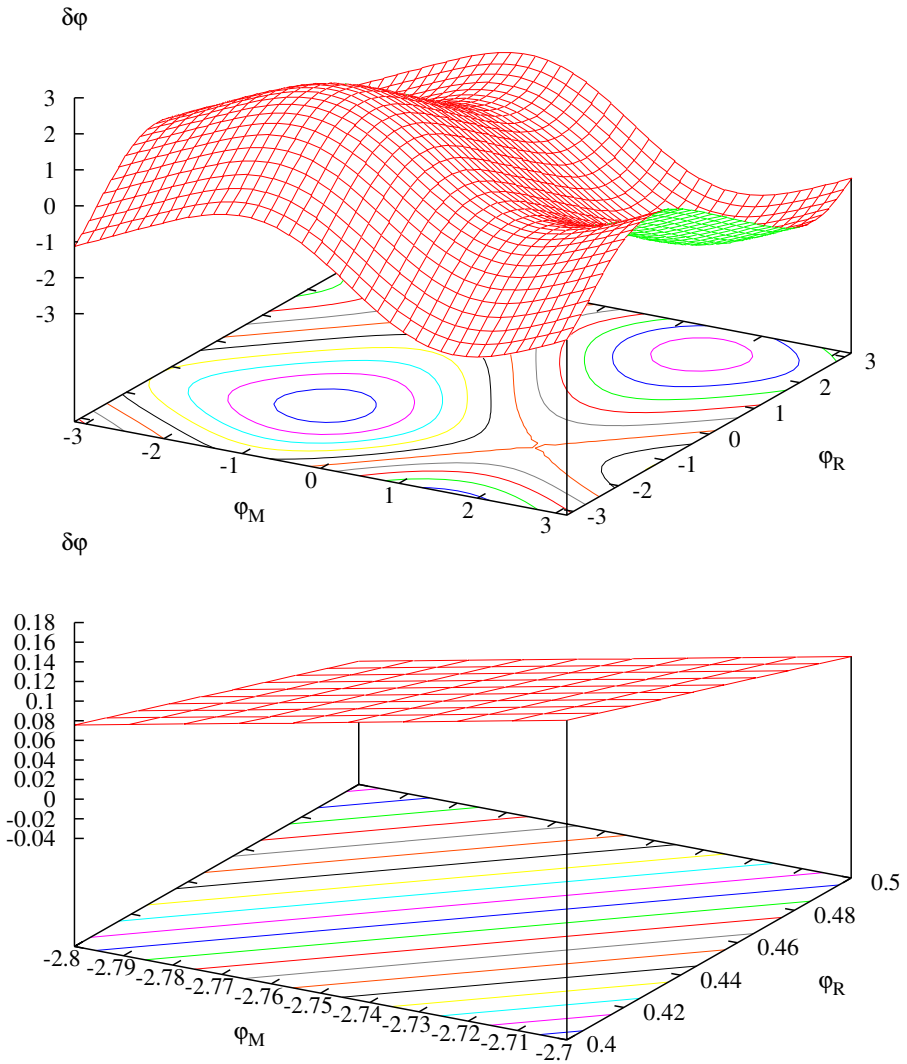

Figure 71: Linear combination of base functions that results from the frequency-domain fit when only a small fraction of the parameter space $(\varphi_{\mathrm{M}}, \varphi_{\mathrm{R}})$ is spanned in the data that is used for estimation of the parameters. The resulting linear combination has an unrealistic large magnitude of several radians when viewed in its full range. In the small range that is scanned in the data, however, the linear combination is constructed such that it looks like $\varphi = \varphi_{\mathrm{M}} - \varphi_{\mathrm{R}}$, because this combination best reduces the RMS spectrum of φ. Subtracting that linear combination effectively subtracts the signal, producing meaningless results.

fit were: frequency range 1...50 mHz, Kaiser window with 120 dB sidelobe suppression and relative weigthing. The resulting form of the correction term was:

$$\delta\varphi = -0.007533 \cdot \sin(\varphi_M + \varphi_R)\sin(\varphi_M - \varphi_R) - 0.002523 \cdot \cos(\varphi_M + \varphi_R)\sin(\varphi_M - \varphi_R). \quad (66)$$

This confirms that the remaining contribution of the second-order sidebands (with OPD stabilization) is not a significant noise source.

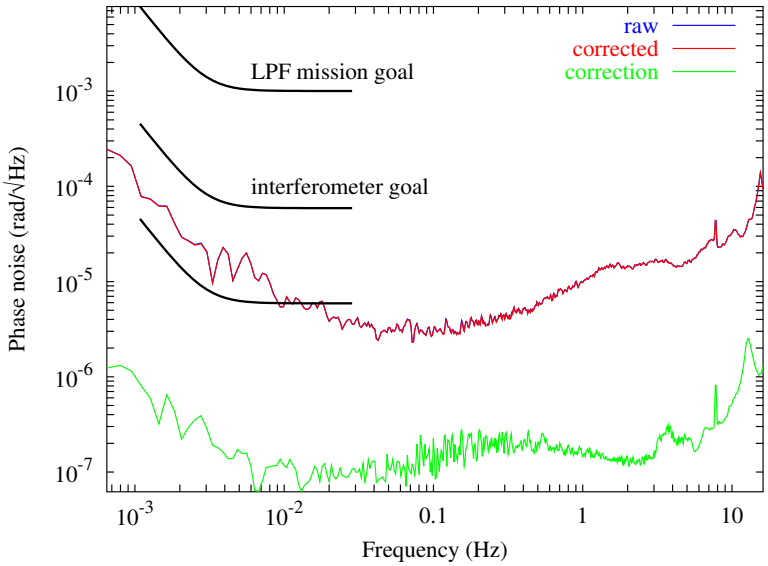

Figure 72: Noise curves of the x_1 interferometer with contribution of second-order sidebands. From top to bottom: uncorrected direct measurement, "corrected" measurement, and correction.

The same method was also used to look for correlations with other parameters such as remaining frequency noise or alignment fluctuations.

10.4 Special operating point

The form of the error term suggests that the error disappears for the special operating points $\varphi_M - \varphi_R = n \cdot 2\pi$. Although it would in theory be possible to force the DFACS system to run at only such operating points, such a strategy would strongly reduce the flexibility of operating modes for the mission and furthermore be in contradiction to the fundamental design principle of the interferometer, namely to be a diagnostic tool that monitors the test masses under a wide variety of operating modes and states. Therefore this possibility is not considered any further.

11 Laser amplitude noise

Laser amplitude noise disturbs the measurement in two ways: In the measurement band (1 mHz...30 mHz), laser power fluctuations[12] correspond to fluctuations of the radiation pressure on the free-floating test mass and would thus produce a real force noise. Since this effect

[12]Following a suboptimal but widely used practice, the terms 'laser amplitude fluctuations' and 'laser power fluctuations' are used interchangeably, although power and amplitude differ by a square root operation and that

is addressed in the laser power stability requirements and furthermore has no effect in our laboratory, where the test masses were represented by fixed mirrors, we do not consider this effect any more in this document.

The second effect concerns laser power fluctuations at Fourier frequencies around the heterodyne frequency f_{het}. As was shown in Section 3.2 on page 19, a coherent amplitude modulation at f_{het} fully shows up in the phase measurement. The same is true for noncoherent noise around f_{het}, which will show up as noise in the phase measurement. Hence the laser power needs to be stabilized at Fourier frequencies around f_{het}. The required stability is moderate: a relative stability of the order of $10^{-6}/\sqrt{\mathrm{Hz}}$ is sufficient.

Laser power stabilization is achieved independently for each of the two beams be measuring their intensity with a single-element photodiode on the optical bench (PDA1 and PDA2, respectively) and actuating on the amplitude contrl input of the respective AOM driver.

While we originally had built a laser power stabilization that was active between DC and about 50 kHz, problems with the dynamic range in long-term measurements[13] made us abandon its use for while.

In order to reduce the remaining noise after the sideband/OPD-related noise was practically removed, we built another laser power stabilization system that is active only around $f_{\mathrm{het}} \approx 1.6\,\mathrm{kHz}$ but has no gain at DC and thus is unaffected by any long-term drifts in the laser power. Figures 73 and 74 on the following page show the open-loop gain of the servo loops for the two beams. They achieve a gain of $30 \ldots 40\,\mathrm{dB}$ at f_{het}. Figure 75 on the previous page shows a circuit diagram of one of the two identical servos, which are basically bandpass filters centered at f_{het}.

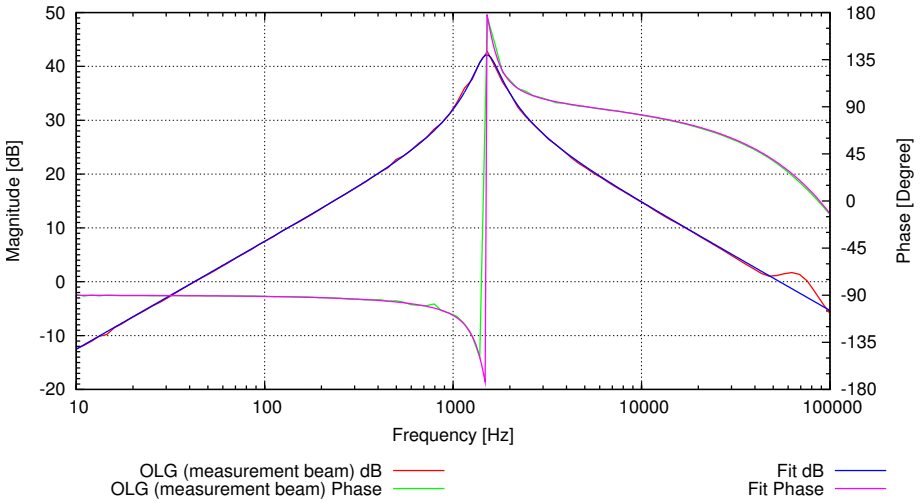

Figure 73: Open-loop gain of the amplitude stabilization in the first beam. The fit of the measured data to a model uncovered a delay of 2.84 μs (mainly due to acoustic delay in the AOM). The pole is at 1.51 kHz and has a Q of 3.57.

Figure 76 on the following page shows the measured noise spectra of the 'PDA2' photodiode (which is used as sensor for the stabilization of the second beam), both when then stabilization was on and off. Since these signals are used for feedback in the servo, they are called 'in-loop'

difference is a frequent source of difficulties. Nevertheless, the same two terms are also often used for 'laser noise', 'laser stabilization' and related expressions. Most often, when they are used to distiguish e.g. laser power stabilization and laser *frequency* stabilization, no harm is done.

[13] In LTP, a slow digital loop running in the DMU will take care of long-term drifts.

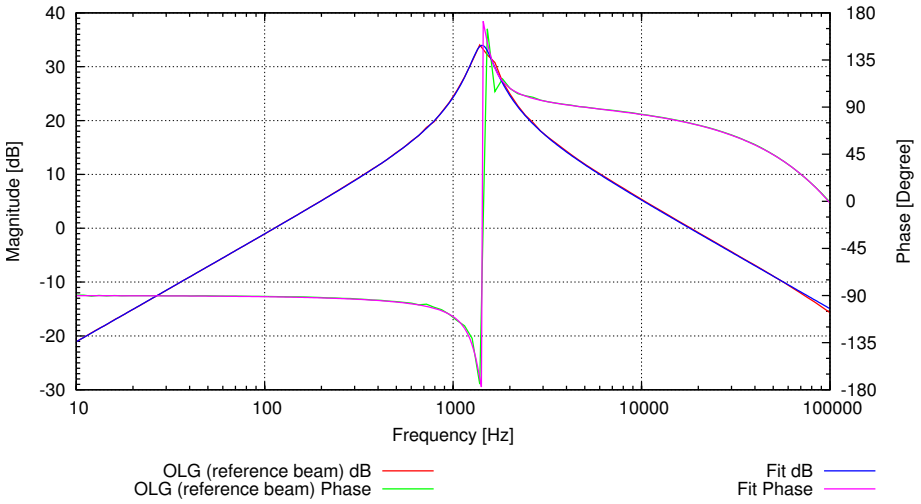

Figure 74: Open-loop gain of the amplitude stabilization in the second beam. The fit of the measured data to a model uncovered a delay of 2.55 μs (mainly due to acoustic delay in the AOM). The pole is at 1.42 kHz and has a Q of 3.97.

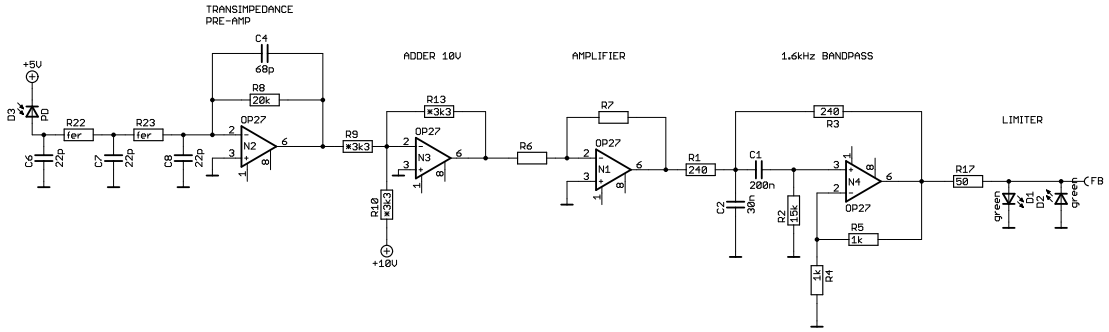

Figure 75: Circuit diagram of one laser power stabilization servo.

signals in our usual terminology. Their being small indicates that the servo works as designed, but not necessarily that the signal to be stabilized is stable in absolute terms. In particular, any noise on this signal would be impressed on the quantity to be stabilized.

A more honest (but, unfortunately, usually also worse) measurement of the performance of a servo loop is obtained when another, independent, sensor for the quantity to be stabilized is evaluated. Such a measurement is called a 'out-of-loop' measurement in our usual terminology[14]. The lower half of Figure 76 on the next page shows such a measurement where the PDF photodiode was used. This demonstrates that in the interesting frequency range between 1 kHz and 2 kHz both a significant real noise reduction and a final noise level below $10^{-6}/\sqrt{\text{Hz}}$ are reached.

The same measurements for the other channel (PDA1) are shown in Figure 77 on the preceding page. In this case, the 'in-loop' signal behaves as is expected from a working loop, but the 'out-of-loop' measurement shows that no real noise reduction is achieved. The reason is the abnormally high dark noise of photodiode PDA1, which is also shown in the top part of Figure 77. This particular photodiode had shown a failure early in the testing program (see also Reference [6]). Later it had seemed to resume normal operation, but the results here show that permanent damage remains.

12 Laser frequency noise

In almost all sensitive interferometers, the laser frequency noise must be stabilized because it produces spurious phase noise at the output as soon as there is a pathlength difference.

The conversion factor from laser frequency fluctuations $\delta\omega = \delta\nu \times (2\,\pi)$ [rad/s] into phase fluctuations $\delta\varphi$ [rad] is given by the differential time delay $\Delta\tau = \Delta s/c$, where Δs is the optical pathlength difference between the two interfering beams (see, e.g., [14] for a derivation).

Using a budget of $\delta\varphi < 6\,\mu\text{rad}/\sqrt{\text{Hz}}$ between 3 mHz and 30 mHz, the frequency stability requirement becomes

$$\widetilde{\delta\nu} = \frac{c}{2\pi\,\Delta l}\,\widetilde{\delta\varphi} = 28\,\frac{\text{kHz}}{\sqrt{\text{Hz}}}\Big/\left[\frac{\Delta l}{1\,\text{cm}}\right]. \tag{67}$$

For the actual pathlength differences in LTP, a worst-case nominal value of 1 cm is assumed, which consists of

- alignment tolerances of the optical bench during its manufacturing,
- mechanical tolerances of the connection between optical bench and inertial sensor housing,
- mechanical tolerances within the inertial sensor,
- uncertainty of the absolute position of the free-floating test mass in various operational modes.

Note that a static pathlength difference between the optical fibers that connect the AOMU and the optical bench (Δ_F in Figure 3 on page 14) does not directly produce spurious phase noise, since its effect is common-mode to the measurement interferometer in question and the reference interferometer and cancels in the subtraction $\varphi = \varphi_R - \varphi_M$. Such a static pathlength difference should, nevertheless, be minimized since (1) such cancellations are never perfect and

[14] In the special case that both sensors are built identically and their noise is independent, such a measurement shows a $\sqrt{2}$ higher noise level than the intrinsic 'real' noise level, if the sensor noise is dominant.

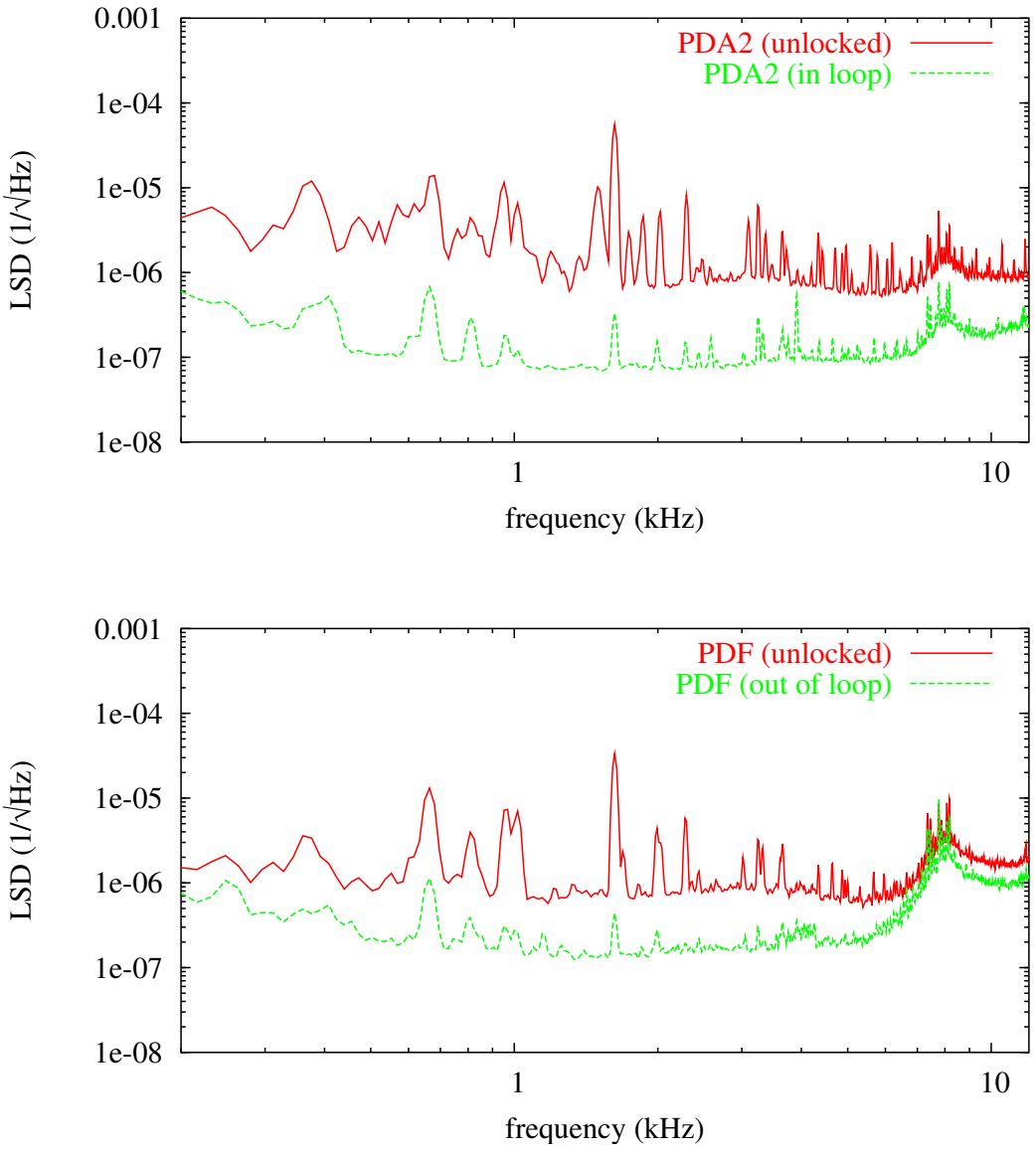

Figure 76: Noise spectra of the laser power stabilization of the second beam.

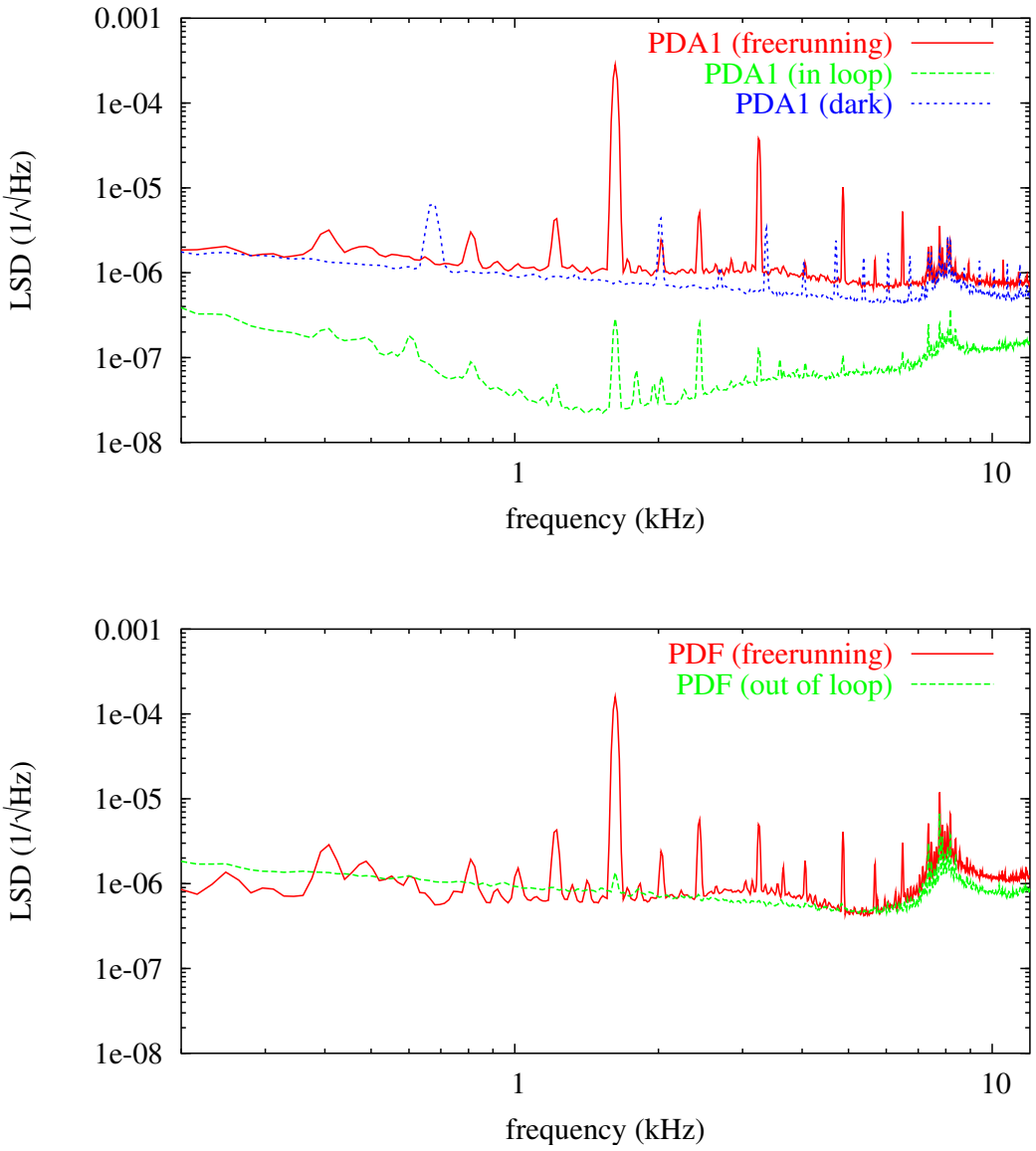

Figure 77: Noise spectra of the laser power stabilization of the first beam.

(2) any such mismatch would still produce phase noise in the 'raw' measurements φ_R and φ_M, causing another noise in the phase measurement due to the 'Doppler' effect (see Section 9 on page 58), which does not cancel.

For sensing the laser frequency fluctuations, the optical bench includes a dedicated interferometer with an intentional armlength difference of 38 cm (see Figure 13 on page 30) which uses photodiodes PDF1 and PDF2. Laser frequency fluctuations appear amplified in the signal $\varphi_R - \varphi_F$, i.e. by comparing the phase of PDF with that of PDR.

In the optical bench EM, we have measured the pathlength differences in the x_1 and $x_1 - x_2$ interferometers by modulating the laser frequency at a few Hz and observing the modulation in the phasemeter outputs $\varphi_{\mathrm{PD1}} - \varphi_{\mathrm{PDR}}$, $\varphi_{\mathrm{PD12}} - \varphi_{\mathrm{PDR}}$ and $\varphi_{\mathrm{PDF}} - \varphi_{\mathrm{PDR}}$, where they appear scaled with the armlength differences of the x_1 , $x_1 - x_2$ and frequency interferometer, respectively. The measured ratios of the modulation peak height were

$$\begin{aligned} \frac{\varphi_{\mathrm{PDF}} - \varphi_{\mathrm{PDR}}}{\varphi_{\mathrm{PD1}} - \varphi_{\mathrm{PDR}}} &= 48.91, \\ \frac{\varphi_{\mathrm{PDF}} - \varphi_{\mathrm{PDR}}}{\varphi_{\mathrm{PD12}} - \varphi_{\mathrm{PDR}}} &= 26.61. \end{aligned} \tag{68}$$

Using the known armlength difference of 38 cm in the frequency interferometer, we can compute the armlength differences in the other two interferometers as

$$\begin{aligned} \Delta s_1 &= \frac{38\,\mathrm{cm}}{48.91} = 7.8\,\mathrm{mm}, \\ \Delta s_{12} &= \frac{38\,\mathrm{cm}}{26.61} = 14.3\,\mathrm{mm}. \end{aligned} \tag{69}$$

These pathlength differences are mainly caused by the absence of the optical windows. The optical paths were designed with optical windows in place. In our experiments, however, we are not using them. Hence we have to move each of the two end mirrors inwards to align the interferometer due to a parallel shift of the beam that would be caused by the window but is absent. In the CAD models, that shift was computed to be 1.58 mm. The missing optical pathlength is about twice that value (due to the reflection), plus a contribution from the missing refractive index of the optical window (2.29 mm per pass in the model). For Δs_1, we would thus expect $2 \cdot (2.29 + 1.58)\,\mathrm{mm} = 7.74\,\mathrm{mm}$, and twice that value for Δs_{12}, which is in reasonable agreement with the measurements.

Figure 78 shows the measured frequency noise of the freerunning Tesat laser (which is typical for Nd:YAG lasers), together with the requirement for the stabilized condition. It can be seen that a loop gain of about 100 at 3 mHz is necessary.

In LTP, this will be a digital servo loop running in the DMU (at 100 Hz update rate) with a loop bandwidth of about 3...5 Hz. In our lab, we used an analog servo with comparable bandwidth for that purpose, since the computer that we use for the phasemeter back-end does not have real-time capabilities. Figure 79 on page 89 shows a circuit diagram of this servo. It consists of two identical input channels that take the analog signals from PDR and PDF, respectively. After bandpass filtering centered at 1.6 kHz, both signals are amplified to a level of $10\,\mathrm{V_{pk}}$ and mutiplied an an analog multiplier that acts as phase detector. Its output is lowpass filtered to remove the 3.2 kHz component and fed to the servo amplifier (one integrator acting on the laser PZT and second integrator acting on the laser temperature as slower outer loop). A very similar circuit was used for the OPD stabilization, using PDR and the electrical heterodyne frequency from the PLL as input signals, and feeding back to the OPD piezo.

Figure 80 and Figure 81 show the noise curves of the x_1 interferometer and the remaining contribution of the laser frequency noise. In Figure 80, the frequency noise contribution was

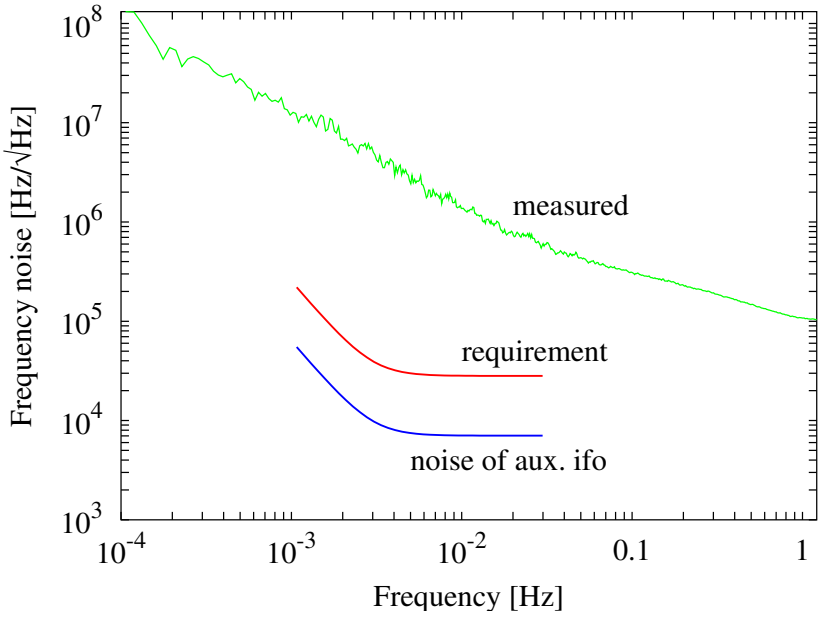

Figure 78: Measured frequency noise of the TESAT laser head (top curve). The middle curve is the frequency noise requirement (to be achieved by frequency stabilization using the signal from the auxiliary interferometer), and the lower curve shows the predicted noise level of that interferometer.

estimated using the factor 0.022 that was obtained from the direct measurement of the coupling factor described above; whereas in Figure 81, a frequency-domain fit as described in Section 10.3.2 was used. The fitting parameters were: frequency range 1…50 mHz, Kaiser window with 120 dB sidelobe suppression and relative weigthing. The coupling factor that minimizes the RMS spectral power under these conditions was 0.0016.

13 Error by beam jitter

Early measurements (e.g. in Glasgow) had shown that the noise level in the interferometer is reduced when the quadrant diodes are replaced by single-element diodes. It was assumed that this could be traced to the inhomogeneous sensitivity of the quadrant diodes, in particular their insensitive slits across the center, in conjunction with beam jitter and a inhomogeneous shape of the phasefront.

Unfortunately it was never possible to make a direct and fair comparison betwen single-element diodes and quadrants. In Glasgow, the single-element diodes were mounted more stably than the quadrant diodes. Furthermore, both diodes used different preamplifiers and associated electronics.

For the OB EM, on the other hand, quadrant diodes are rigidly mounted on the base plate and cannot be exchanged without the risk of destroying the bench.

Attempts to observe such effects in table-top setups failed due to the high intrinsic noise level of such setups, which is higher than the small effects under investigation.

Measurements with our special wavefront measurement device (Appendix E on page 107) have

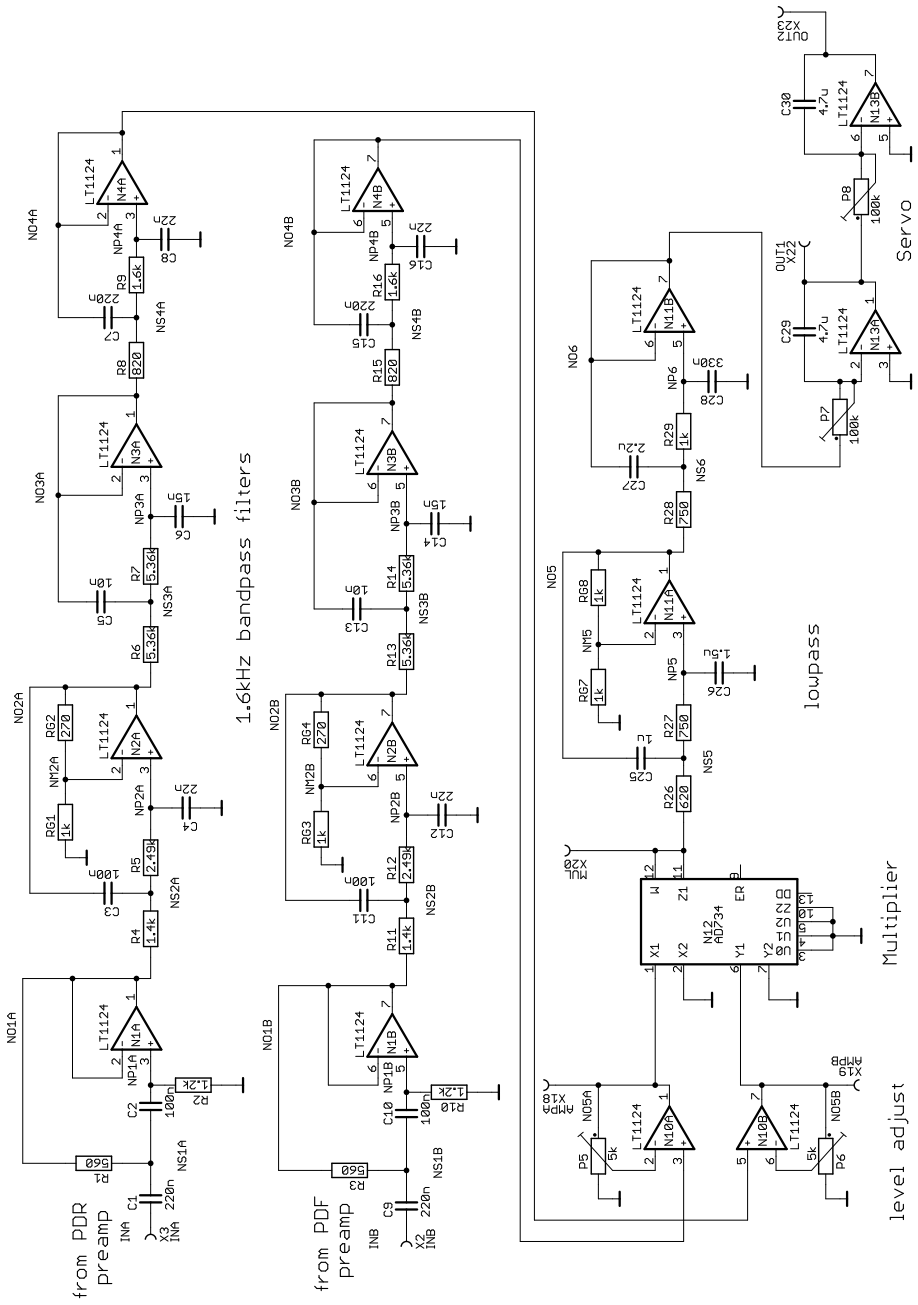

Figure 79: Circuit diagram of the analog servo for frequency stabilization.

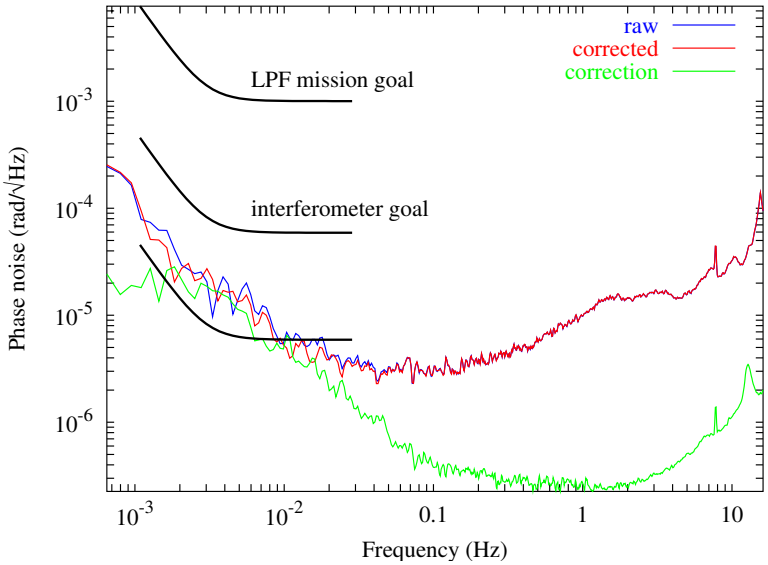

Figure 80: Noise curves of the x_1 interferometer with frequency noise contribution. From top to bottom: uncorrected direct measurement, "corrected" measurement, and correction. The correction was the PDR-PDF measurement, multiplied with 0.022, the factor obtained from the direct coupling measurement.

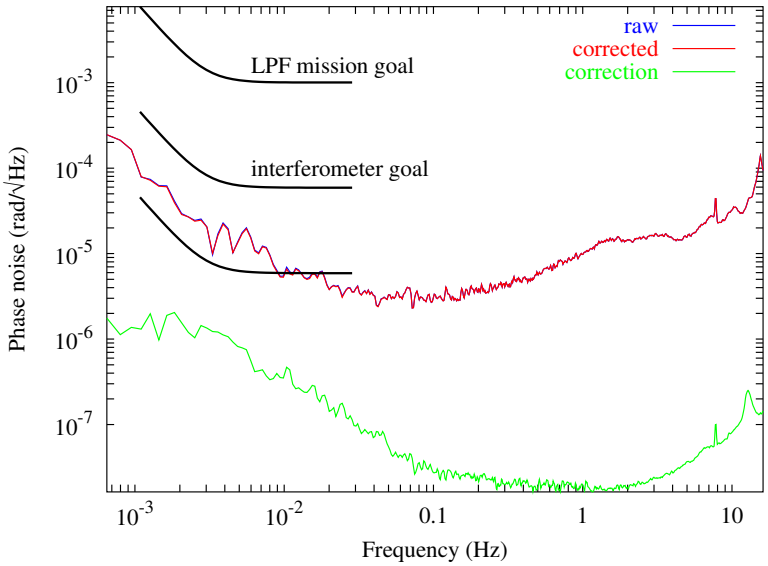

Figure 81: Noise curves of the x_1 interferometer with frequency noise contribution. From top to bottom: uncorrected direct measurement, "corrected" measurement, and correction. The correction was the PDR-PDF measurement, multiplied with 0.0016, the factor that minimizes the weighted RMS between 1 mHz and 50 mHz.

shown that the phasefront in the OB EM is indeed inhomogeneous (see Figure 9 in Appendix E). We have thus proposed to use that device in the production of the FM to ensure phasefronts that are better matched.

Appendix F on page 116 summarizes numerical simulations on this effect.

13.1 Correlation measurements

With the existing hardware and data, the only thing that we could do was to analyze the data for correlations between the longitudinal signal φ and the alignment signals, that are measured at the same time.

We have done this with several procedures and for several data sets, and have, in general, obtained no measurable correlation.

The very 'best' result is shown in Figure 82. Here the frequency-domain method (Section 10.3.2 on page 79) was employed on our good reference data set. The frequency range used to obtain the calibration coefficients was 2 mHz... 100 mHz, the time-domain window was a Kaiser window with $\alpha = 5.019$ (120 dB PSLL), the Fourier components were weighted with the reciprocal of their squared magnitude (corresponding to a "relative" or "logarithmic" weighting), and 12 parameters were used for the fit: DWS and DC alignment signals in two dimensions for three photodiodes (PDR, PD1 and PD12).

The coefficients thus found were used to subtract a corresponding fraction of the respective alignment signals from φ in the time series.

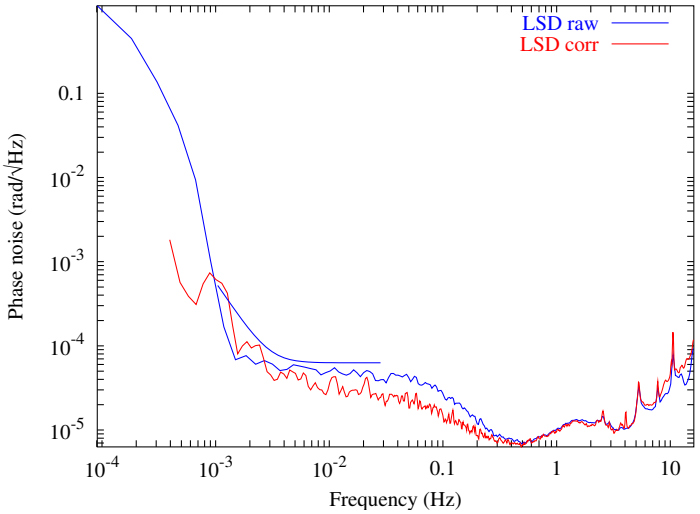

Figure 82: Spectrum with alignment correlations subtracted.

These results should, however, be treated with care as

- They can only be obtained when including the DC alignment signals, whereas we expect the DWS alignment signals to be a better representation of misalignments.
- In the OB EM we do not really expect any beam jitter, as everything is rigidly mounted (see also Figure 84 on the preceding page).

- The results are not very reproducible and depend strongly on fine-tuning the fitting procedure.

A more trustworthy result was obtained when only the DWS signals were included in the fit ($3 \times 2 = 6$ signals from PDR, PD1 and PDF, fitted to optimize the frequency range from 1 mHz to 50 mHz). Figure 83 shows that in this case, the contribution of beam-jitter correlated noise is negligible.

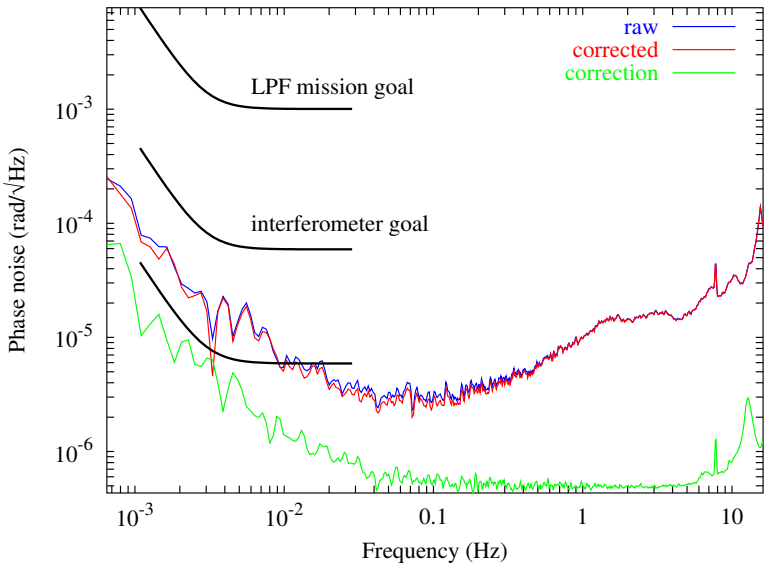

Figure 83: Noise curves of the x_1 interferometer with contribution of alignment-related noise as measured by the DWS signals. From top to bottom: uncorrected direct measurement, "corrected" measurement, and correction.

Figure 84 on the previous page shows the measured spectra of the alignment fluctuations, which shows that (1) they are below the $10\,\mathrm{nrad}/\sqrt{\mathrm{Hz}}$ requirement (except for one signal with large static misalignment) and (2) they are indeed rather small.

We conclude that with the present setup we cannot find any real correlation between alignment signals and longitudinal noise. Considering that the beam shapes are not well matched in the EM, but will be hopefully be better matched in the FM (e.g. by using the real-time wavefront measurement device), and that even with the EM we have now obtained noise levels below the requirement specification at all frequencies in the measurement band, we do not consider this noise source to be a significant problem for LTP. Our earlier worries that beam jitter in conjunction with quadrant diodes might lead to significant noise luckily thus turned out to be unfounded.

A Modulated light and sidebands

Amplitude- and phase-modulation are important cases when *sidebands* occur next to a carrier. Commonly used relationships and formulae are presented here for reference.

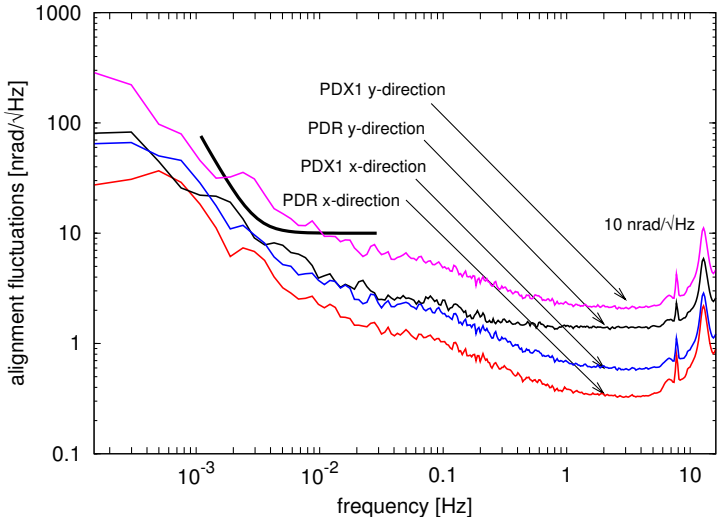

Figure 84: Spectrum of alignment fluctuations, referred to test mass tilt.

A.1 Phase modulation

We write the electrical field of the unmodulated laser beam at a fixed point in space in the scalar representation

$$E(t) = E_0 \exp(\,\mathrm{i}\,\omega_0 t)\,. \tag{70}$$

Phase modulation with the angular frequency $\omega_\mathrm{m} = 2\pi\, f_\mathrm{m}$ and the modulation depth ('modulation index') m yields

$$\begin{aligned} E_\mathrm{m}(t) &= E_0 \exp[\,\mathrm{i}\,(\omega_0 t + m\cos\omega_\mathrm{m} t)] \\ &= E_0 \exp(\,\mathrm{i}\,\omega_0 t)\exp(\,\mathrm{i}\,m\cos\omega_\mathrm{m} t). \end{aligned} \tag{71}$$

Using the identity [3, Vol. 2, No. 8.511]

$$\exp(\,\mathrm{i}\;m\cos\alpha) = \sum_{k=-\infty}^{\infty} \mathrm{i}^{\,k} J_k(m)\exp(\,\mathrm{i}\;k\,\alpha) = J_0(m) + 2\sum_{k=1}^{\infty} \mathrm{i}^{\,k} J_k(m)\cos(k\,\alpha) \tag{72}$$

we find for the amplitude of the modulated light

$$E_\mathrm{m}(t) = E_0 \exp(\,\mathrm{i}\,\omega_0 t) \sum_{k=-\infty}^{\infty} \mathrm{i}^{\,k} J_k(m)\exp(\,\mathrm{i}\;k\omega_\mathrm{m} t). \tag{73}$$

Here the $J_k(x)$ are the Bessel functions of the first kind of order k. The first terms of their

Taylor series are:

$$
\begin{aligned}
J_0(x) &= 1 - \frac{x^2}{4} + \mathcal{O}(x^4) \\
J_1(x) &= \frac{x}{2} - \frac{x^3}{16} + \mathcal{O}(x^5) \\
J_2(x) &= \frac{x^2}{8} + \mathcal{O}(x^4)
\end{aligned}
$$

$$
J_k(x) = \frac{1}{k!}\left(\frac{x}{2}\right)^k + \mathcal{O}(x^{k+2}). \tag{74}
$$

Furthermore we have

$$
J_{-k}(x) = (-1)^k J_k(x). \tag{75}
$$

Sometimes the higher orders are needed, but often a small modulation index $m < 1$ can be assumed and we need to consider only the first terms:

$$
\begin{aligned}
E_{\mathrm{m}}(t) &\approx E_0 \exp(\,\mathrm{i}\,\omega_0 t) \\
&\quad \times \Big(J_0(m) + \,\mathrm{i}\, J_1(m) \exp[\,\mathrm{i}\,\omega_{\mathrm{m}} t] + \,\mathrm{i}\, J_1(m) \exp[-\,\mathrm{i}\,\omega_{\mathrm{m}} t] \Big) \\
&\approx E_0 \exp(\,\mathrm{i}\,\omega_0 t)\,(J_0(m) + 2\ \mathrm{i}\ J_1(m) \cos\omega_{\mathrm{m}} t) \\
&\approx E_0 \exp(\,\mathrm{i}\,\omega_0 t)\,(1 + \,\mathrm{i}\ m \cos\omega_{\mathrm{m}} t)\,.
\end{aligned} \tag{76}
$$

We see from the first equation that the phase modulation has created two *sidebands* with a frequency offset of $\pm\omega_{\mathrm{m}}$ against the carrier and with a phase shift of $\mathrm{i} \triangleq 90°$ each. Their amplitude is $J_1(m) \approx m/2$, i.e. they contain a fraction $m^2/4$ each of the original (unmodulated) carrier power. The remaining carrier has the amplitude $J_0(m) \approx 1 - m^2/4$, corresponding to $1 - m^2/2$ of the original power.

Note that if we start with an (essentially equivalent) modulation signal given by $\sin\omega_{\mathrm{m}} t$ instead of $\cos\omega_{\mathrm{m}} t$, we have to apply a slightly more complicated identity:

$$
\begin{aligned}
&\exp(\,\mathrm{i}\ m \sin\alpha) = \\
&\qquad J_0(m) + 2\ \mathrm{i}\ \sum_{k=0}^{\infty} J_{2k+1}(m) \sin((2k+1)\,\alpha) + 2 \sum_{k=1}^{\infty} J_{2k}(m) \cos(2k\,\alpha).
\end{aligned} \tag{77}
$$

The modulated field with only the first sidebands now becomes:

$$
\begin{aligned}
E'_{\mathrm{m}}(t) &\approx E_0 \exp(\,\mathrm{i}\,\omega_0 t) \\
&\quad \times \Big(J_0(m) - J_1(m) \exp[\,\mathrm{i}\,\omega_{\mathrm{m}} t] + J_1(m) \exp[-\,\mathrm{i}\,\omega_{\mathrm{m}} t] \Big) \\
&\approx E_0 \exp(\,\mathrm{i}\,\omega_0 t)\,(J_0(m) + 2\ \mathrm{i}\ J_1(m) \sin\omega_{\mathrm{m}} t) \\
&\approx E_0 \exp(\,\mathrm{i}\,\omega_0 t)\,(1 + \,\mathrm{i}\ m \sin\omega_{\mathrm{m}} t)\,.
\end{aligned} \tag{78}
$$

Note the missing factor 'i' in the first equation and the different signs as compared to Equation 76. We usually prefer Equation 76 on the previous page over Equation 78 on page 94 because the former is more symmetrical and easier to remember.

A.2 Amplitude modulation

A small *amplitude* modulation, on the other hand, yields spectra given by

$$E_0 \exp(\mathrm{i}\,\omega_0 t)\,(1 + m\cos\omega_\mathrm{m} t) = E_0 \exp(\mathrm{i}\,\omega_0 t)\left(1 + \frac{m}{2}\exp[\mathrm{i}\,\omega_\mathrm{m} t] + \frac{m}{2}\exp[-\mathrm{i}\,\omega_\mathrm{m} t]\right) \quad (79)$$

for a modulation with $\cos\omega_\mathrm{m} t$ and

$$E_0 \exp(\mathrm{i}\,\omega_0 t)\,(1 + m\sin\omega_\mathrm{m} t) = E_0 \exp(\mathrm{i}\,\omega_0 t)\left(1 - \mathrm{i}\,\frac{m}{2}\exp[\mathrm{i}\,\omega_\mathrm{m} t] + \mathrm{i}\,\frac{m}{2}\exp[-\mathrm{i}\,\omega_\mathrm{m} t]\right) \quad (80)$$

for a modulation with $\sin\omega_\mathrm{m} t$. This can easily be understood and remembered with the help of phasor diagrams. Amplitude modulation with an arbitrary phase γ can be written as

$$E_0 \exp(\mathrm{i}\,\omega_0 t)\,(1 + m\cos(\omega_\mathrm{m} t + \gamma)) = E_0 \exp(\mathrm{i}\,\omega_0 t)\left(1 + \frac{m}{2}\exp[\mathrm{i}\,\omega_\mathrm{m} t + \gamma] + \frac{m}{2}\exp[-\mathrm{i}\,\omega_\mathrm{m} t - \gamma]\right) \quad (81)$$

A.3 Frequency modulation

When looking at laser noise, we also have to consider a frequency modulation of the light field. A sinusoidal frequency modulation at the frequency ω_m with the modulation depth $\Delta\omega$ can be expressed by

$$\begin{aligned} E(t) &= E_0 \exp(\mathrm{i}\,\varphi(t)), \\ \varphi(t) &= \int (\omega_0 + \Delta\omega \sin\omega_\mathrm{m} t)dt. \end{aligned} \quad (82)$$

Note that one might be tempted to write

$$\varphi(t) = (\omega_0 + \Delta\omega \sin\omega_\mathrm{m} t)t, \quad \textbf{(wrong)} \quad (83)$$

but this yields wrong results[15]. From Equation (82 on the previous page) it follows immediately that

$$\begin{aligned} \varphi(t) &= \omega_0 t - \frac{\Delta\omega}{\omega_\mathrm{m}}\cos\omega_\mathrm{m} t, \\ E(t) &= E_0 \exp(\mathrm{i}\,\omega_0 t)\exp\left(-\mathrm{i}\,\frac{\Delta\omega}{\omega_\mathrm{m}}\cos\omega_\mathrm{m} t\right). \end{aligned} \quad (84)$$

Hence a sinusoidal frequency modulation behaves like a phase modulation of the same frequency with the modulation index

$$m_\mathrm{FM} = \frac{\Delta\omega}{\omega_\mathrm{m}}. \quad (85)$$

In communications theory (see e.g. Reference [2]), one distinguishes between *narrowband* FM, which is characterized by $m \ll 1$ and its opposite, *wideband* FM.

[15] The frequency, given by $d\varphi/dt$, would become

$$\omega = \omega_0 + \Delta\omega \sin\omega_\mathrm{m} t + \Delta\omega\,\omega_\mathrm{m}\, t\, \cos\omega_\mathrm{m} t,$$

and the last term, which is proportional to t, is wrong.

The spectrum of a narrowband FM signal contains (apart from the carrier) mainly the first upper and lower modulation sidebands, separated from the carrier by ω_{m}. It is described by Equations (76 on page 94) and (85 on page 95).

A wideband FM signal, on the other hand, contains many spectral components at multiples of ω_{m} from the carrier. As an example, Figure 85 on page 96 shows the spectrum of a 100 kHz carrier, modulated at 1 kHz ($\omega_{\mathrm{m}} = 2\pi \cdot 1\,\mathrm{kHz}$) with a modulation depth of $\Delta\omega = 2\pi \cdot 10\,\mathrm{kHz}$, i.e. $m_{\mathrm{FM}} = 10$.

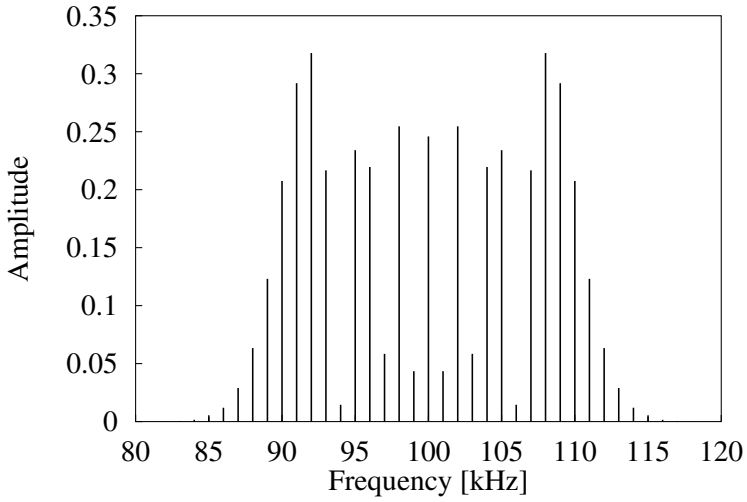

Figure 85: Spectrum of a frequency modulated signal with $m_{\mathrm{FM}} = 10$. The phase of each component is one out of 1, i, -1 or $-\mathrm{i}$, but the figure shows only the absolute values.

B Mathematica code

```
<<clear.m
(* demod.m: Auxiliary functions to describe demodulation
   The modulation frequency must be called 'wm',
   and the time 't'. *)

(* The Power in a beam with amplitude x, i.e. |x|^2 *)
power[x_]:=ComplexExpand[x Conjugate[x],TargetFunctions->{Re,Im}];

(* Extract only terms swinging at the mod. frequency *)
sinrule[1]:={
Sin[a_.+(m_/;(Abs[m]!=1))t wm]->0,
Cos[a_.+(m_/;(Abs[m]!=1))t wm]->0
};

(* Rules to extract terms at a multiple of the modulation frequency *)
sinrule[n_]:={
Sin[a_.+(m_/;(Abs[m]!=n))t wm]->0,
Cos[a_.+(m_/;(Abs[m]!=n))t wm]->0,
```

```
Sin[a_.+t wm]->0,
Cos[a_.+t wm]->0,
Sin[a_.-t wm]->0,
Cos[a_.-t wm]->0
};

(* Compute components of 'a' at 'n' times the mod. frequency *)
s[a_,n_] := Select[ExpandAll[TrigReduce[a]],!FreeQ[#,t]&]/.sinrule[n];

(* Compute DC component of 'a' *)
s[a_,0] := Select[ExpandAll[TrigReduce[a]],FreeQ[#,t]&];

(* Complex amplitude at wm *)
camp[a_] := Module [
{sinamp, cosamp, tm},
tm=2 Pi/wm;
sinamp=Simplify[Integrate[a Sin[wm t], {t, 0, tm}]/tm];
cosamp=Simplify[Integrate[a Cos[wm t], {t, 0, tm}]/tm];
cosamp+I sinamp
]

(* wm component of power *)
wmpow[a_] := Module [
{p},
p = power[a];
Simplify[s[p,1]]
]

(* Taylor series around eps=0 *)
errterm0[x_,n_] := FullSimplify[Normal[Series[x,{eps,0,n}]]];

(* phase approximated by imaginary part *)
errterm[x_,n_] := FullSimplify[ComplexExpand[Im[errterm0[x,n]]]/eps];

(* Rule to replace Delta by Phi *)
phirule = {dr -> phir - df, dm -> phim - df}

(* The two beams *)
beam1=Exp[I waom t] +
 am2 Exp[I (waom-2*wm) t] + am1 Exp[I (waom-wm) t] +
 ap1 Exp[I (waom+wm) t] + ap2 Exp[I (waom+2*wm) t]
beam2=Exp[I (waom+wm) t] +
 bm2 Exp[I (waom-wm) t] + bm1 Exp[I (waom) t] +
 bp1 Exp[I (waom+2*wm) t] + bp2 Exp[I (waom+3*wm) t]

(* interfering amplitudes in 2 interferometers *)
amfull = beam1 Exp[-I (dm+df)] + beam2
arfull = beam1 Exp[-I (dr+df)] + beam2

(* Reference case with zero sidebands *)
rule0={am2 -> 0, am1 -> 0, ap1 -> 0, ap2 -> 0,
       bm2 -> 0, bm1 -> 0, bp1 -> 0, bp2 -> 0} ;
```

```
am = Simplify[amfull /. rule0];
ar = Simplify[arfull /. rule0];
c0=Simplify[camp[wmpow[am]]/ camp[wmpow[ar]]]

(* One first-order sideband *)
rule1={am2 -> 0, am1 -> eps Exp[-I gamma1], ap1 -> 0, ap2 -> 0,
       bm2 -> 0, bm1 -> 0, bp1 -> 0, bp2 -> 0} ;
am = Simplify[amfull /. rule1];
ar = Simplify[arfull /. rule1];
c1=Simplify[camp[wmpow[am]]/ camp[wmpow[ar]]];
diff1=eps1 errterm[c1/c0,1] /. phirule;

(* AM *)
rule5={am2 -> 0, am1 -> eps/2, ap1 -> eps/2, ap2 -> 0,
       bm2 -> 0, bm1 -> 0, bp1 -> 0, bp2 -> 0} ;
am = Simplify[amfull /. rule5];
ar = Simplify[arfull /. rule5];
c5=Simplify[camp[wmpow[am]]/ camp[wmpow[ar]]];
diff5=errterm[c5/c0,1] /. phirule

(* One second order sideband*)
rule9={am2 -> 0, am1 -> 0, ap1 -> 0, ap2 -> 0,
       bm2 -> eps Exp[-I gamma], bm1 -> 0, bp1 -> 0, bp2 -> 0} ;
am = Simplify[amfull /. rule9];
ar = Simplify[arfull /. rule9];
c9=Simplify[camp[wmpow[am]]/ camp[wmpow[ar]]];
diff9=errterm[c9/c0,1] /. phirule
```

C Linear fitting

A set of data $y_i, \{i = 0, \ldots, N-1\}$ is to be modelled by linear functions

$$y_i^{\text{model}} = p_0 f_0(\vec{x}_i) + \cdots + p_{n-1} f_{n-1}(\vec{x}_i), \tag{86}$$

where $p_0 \ldots p_{n-1}$ are the unknown coefficients and $f_0 \ldots f_{n-1}$ the base functions that depend on a set of independent variables $\vec{x}$. In our application, typically the function to be modelled is $y = \delta\varphi$, and the independent variables are φ_R, φ_M, the time t or alignment signals. A typical base function might be $f(\varphi_R, \varphi_M) = \sin((\varphi_R + \varphi_M)/2)$.

Following standard procedure[4], the rms deviation between measured data and model,

$$\chi^2 = \sum_{i=0}^{N-1} |y_i^{\text{model}} - y_i^{\text{meas}}|^2, \tag{87}$$

is minimized. In a linear model as we have here, there is a unique solution explicitely available by solving the linear set of normal equations:

$$A\vec{p} = \vec{b} \tag{88}$$

with the elements of the matrix $A = (a_{ij})$ and the right hand side $\vec{b} = (b_j)$ are given by

$$a_{jk} = a_{kj} = \sum_{i=0}^{N-1} f_j(\vec{x}_i) \cdot f_k(\vec{x}_i),$$
$$b_j = \sum_{i=0}^{N-1} f_j(\vec{x}_i) \cdot y_i^{\text{meas}}. \tag{89}$$
$$\tag{90}$$

Since the matrix A is symmetric and positive definite, Equation 88 on page 98 can be solved by Cholesky decomposition. More advanced methods, such as singular value decomposition, exist but were not necessary for this application.

While up to here the described method is textbook standard, the method can be generalized for the case that the data y_i^{meas} and the base functions $f_0 \dots f_{n-1}$ are complex. The elements of the matrix $A = (a_{ij})$ and the right hand side $\vec{b} = (b_j)$ then become

$$\begin{aligned} a_{jk} = a_{kj} &= \sum_{i=0}^{N-1} \Re\{f_j(\vec{x}_i) \cdot f_k(\vec{x}_i)^*\} \\ &= \sum_{i=0}^{N-1} \Re\{f_j(\vec{x}_i)\} \cdot \Re\{f_k(\vec{x}_i)\} + \Im\{f_j(\vec{x}_i)\} \cdot \Im\{f_k(\vec{x}_i)\}, \end{aligned} \tag{91}$$

$$\begin{aligned} b_j &= \sum_{i=0}^{N-1} \Re\{f_j(\vec{x}_i) \cdot (y_i^{\text{meas}})^*\} \\ &= \sum_{i=0}^{N-1} \Re\{f_j(\vec{x}_i)\} \cdot \Re\{y_i^{\text{meas}}\} + \Im\{f_j(\vec{x}_i)\} \cdot \Im\{y_i^{\text{meas}}\}. \end{aligned} \tag{92}$$

The following C code performs the linear fit for real data and also produces error estimates for the parameters under the assumption that the model is adequate and the remaining errors have a normal distribution.

```
/* Linear fit of data set x[] and y[]
to model functions F0...F6 using Cholesky-
decomposition, including error estimates.
Gerhard Heinzel AEI 02/2005
*/

#define NPARMS 7
#define F0(t,x,y) (1)
#define F1(t,x,y) (t)
#define F2(t,x,y) (t*t)
#define F3(t,x,y) (sin (x + y))
#define F4(t,x,y) (cos (x + y))
#define F5(t,x,y) (sin ((x+y)/2))
#define F6(t,x,y) (cos ((x+y)/2))

#define C_SIZE(n) (((n+1)*(n+2))/2)
#define C_DIAG(i) ((i*(i+3))/2)
#define C_INDEX(i,j) ((i*(i+1))/2+j)
#define C_INDEX2(i,j) ((i>=j) ? C_INDEX(i,j) : C_INDEX(j,i))
```

```
void
choleski_fit (int n, double *x, double *y, double *p, double *err, double *rms)
{
  int i, j, k;
  double f[NPARMS];
  long double a[C_SIZE (NPARMS)], l[C_SIZE (NPARMS)], inv[C_SIZE (NPARMS)];
  long double b[NPARMS];
  long double t, sum, chi2;
  long double sum1, sum2;

  for (i = 0; i < NPARMS; i++)
    b[i] = 0;
  for (i = 0; i < C_SIZE (NPARMS); i++)
    a[i] = 0;
  sum1 = sum2 = 0;
  for (j = 0; j < n; j++)
    {
      t = (long double) j / (long double) n;
      sum1 += x[j];
      sum2 += y[j];
      f[0] = F0 (t, x[j], y[j]);
      f[1] = F1 (t, x[j], y[j]);
      f[2] = F2 (t, x[j], y[j]);
      f[3] = F3 (t, x[j], y[j]);
      f[4] = F4 (t, x[j], y[j]);
      f[5] = F5 (t, x[j], y[j]);
      f[6] = F6 (t, x[j], y[j]);
      for (i = 0; i < NPARMS; i++)
        {
          b[i] += (x[j] - y[j]) * f[i];
          for (k = 0; k <= i; k++)
            a[C_INDEX (i, k)] += f[i] * f[k];
        }
    }

/* Cholesky-Decomp */
  for (i = 0; i < NPARMS; i++)
    {
      sum = 0;
      for (k = 0; k < i; k++)
        sum += l[C_INDEX (i, k)] * l[C_INDEX (i, k)];
      sum = a[C_DIAG (i)] - sum;
      assert (sum > 0);
      l[C_DIAG (i)] = sqrtl (sum);
      for (j = i + 1; j < NPARMS; j++)
        {
          sum = 0;
          for (k = 0; k < i; k++)
            sum += l[C_INDEX (i, k)] * l[C_INDEX (j, k)];
          l[C_INDEX (j, i)] = (a[C_INDEX (j, i)] - sum) / l[C_DIAG (i)];
        }
```

```
    }

/* Invert L */
  memcpy (inv, l, C_SIZE (NPARMS) * sizeof (long double));
  for (i = 0; i < NPARMS; i++)
    {
      inv[C_DIAG (i)] = 1. / l[C_DIAG (i)];
      for (j = i + 1; j < NPARMS; j++)
        {
          sum = 0;
          for (k = i; k < j; k++)
            sum -= inv[C_INDEX (j, k)] * inv[C_INDEX (k, i)];
          inv[C_INDEX (j, i)] = sum / l[C_DIAG (j)];
        }
    }

  /* substitute to solve for b */
  for (i = 0; i < NPARMS; i++)
    {
      sum = b[i];
      for (k = i - 1; k >= 0; k--)
        sum -= b[k] * l[C_INDEX (i, k)];
      b[i] = sum / l[C_DIAG (i)];
    }
  for (i = NPARMS - 1; i >= 0; i--)
    {
      sum = b[i];
      for (k = i + 1; k < NPARMS; k++)
        sum -= b[k] * l[C_INDEX (k, i)];
      b[i] = sum / l[C_DIAG (i)];
    }

  /* get chi^2 */
  chi2 = 0;
  for (j = 0; j < n; j++)
    {
      double t = (double) j / (double) n;
      sum =
        b[0] * F0 (t, x[j], y[j]) +
        b[1] * F1 (t, x[j], y[j]) +
        b[2] * F2 (t, x[j], y[j]) +
        b[3] * F3 (t, x[j], y[j]) +
        b[4] * F4 (t, x[j], y[j]) +
        b[5] * F5 (t, x[j], y[j]) +
        b[6] * F6 (t, x[j], y[j]) - (x[j] - y[j]);
      chi2 += sum * sum;
    }
  *rms = sqrt (chi2 / n);
  /* copy resulting parameters */
  for (i = 0; i < NPARMS; i++)
    p[i] = b[i];
```

```
  /* get parameter errors */
  for (i = 0; i < NPARMS; i++)
    {
      sum = 0;
      for (k = i; k < NPARMS; k++)
        sum += inv[C_INDEX (k, i)] * inv[C_INDEX (k, i)];
      err[i] = sqrtl (chi2 * sum / (n - NPARMS));
    }
}
```

D Datasheet of RF amplifier module

MITSUBISHI RF POWER MODULE

M67743L

68-81MHz, 12.5V, 7W, FM PORTABLE RADIO

OUTLINE DRAWING Dimensions in mm

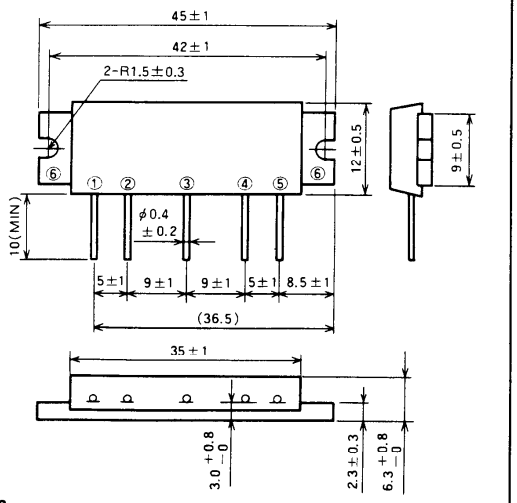

H13

BLOCK DIAGRAM

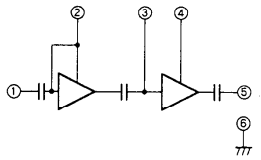

PIN :
①Pin : RF INPUT
②Vcc1 : 1st. DC SUPPLY
③VBB : BASE BIAS SUPPLY
④Vcc2 : 2nd. DC SUPPLY
⑤Po : RF OUTPUT
⑥GND : FIN

ABSOLUTE MAXIMUM RATINGS (Tc = 25℃ unless otherwise noted)

Symbol	Parameter	Conditions	Ratings	Unit
Vcc	Supply voltage		15	V
VBB	Base bias		5.5	V
Icc	Total current		4	A
Pin(max)	Input power	ZG = ZL = 50 Ω, Vcc1 ≦ 12.5V	40	mW
Po(max)	Output power	ZG = ZL = 50 Ω	10	W
Tc(OP)	Operation case temperature		− 30 to 110	℃
Tstg	Storage temperature		− 40 to 110	℃

Note. Above parameters are guaranteed independently.

ELECTRICAL CHARACTERISTICS (Tc = 25℃ unless otherwise noted)

Symbol	Parameter	Test conditions	Limits		Unit
			Min	Max	
f	Frequency range	Pin = 30mW VBB = 5V Vcc = 12.5V ZG = ZL = 50 Ω	68	81	MHz
Po	Output power		7		W
ηT	Total efficiency		38		%
2fo	2nd. harmonic			− 18	dBc
3fo	3rd. harmonic			− 25	dBc
ρin	Input VSWR			4.0	−
−	Load VSWR tolerance	Vcc = 13.2V, VBB = 5V Po = 7W (Pin : controlled) Load VSWR=20:1(All phase), 2sec. ZG = 50 Ω	No degradation or destroy		−

Note. Above parameters, ratings, limits and conditions are subject to change.

NOV. '97

MITSUBISHI ELECTRIC

TYPICAL PERFORMANCE DATA

OUTPUT POWER, TOTAL EFFICIENCY, ρ in VS. FREQUENCY CHARACTERISTICS

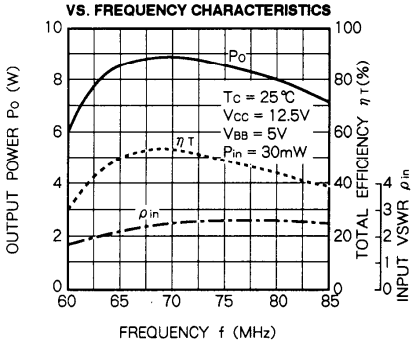

2nd, 3rd HARMONIC VS. FREQUENCY CHARACTERISTICS

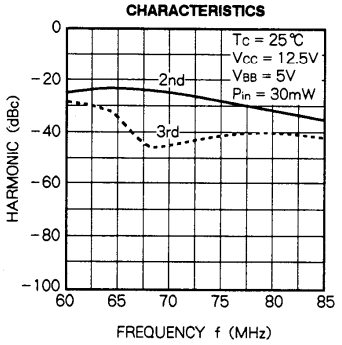

OUTPUT POWER, TOTAL CURRENT, 1st CURRENT VS. INPUT POWER CHARACTERISTICS

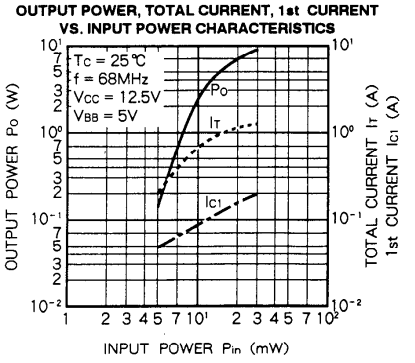

OUTPUT POWER, TOTAL CURRENT, 1st CURRENT VS. INPUT POWER CHARACTERISTICS

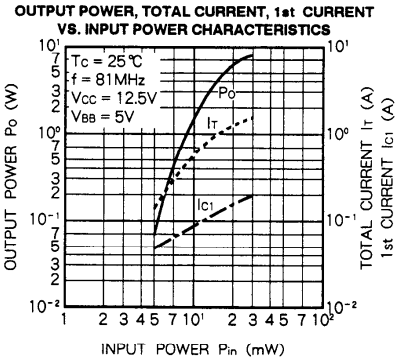

OUTPUT POWER, TOTAL CURRENT, 1st CURRENT VS. SUPPLY VOLTAGE CHARACTERISTICS

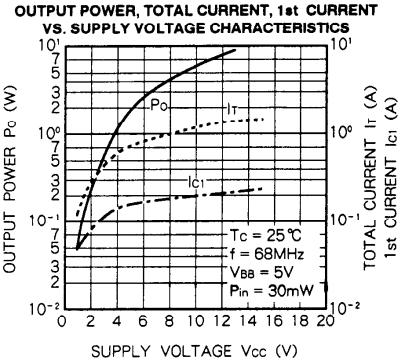

OUTPUT POWER, TOTAL CURRENT, 1st CURRENT VS. SUPPLY VOLTAGE CHARACTERISTICS

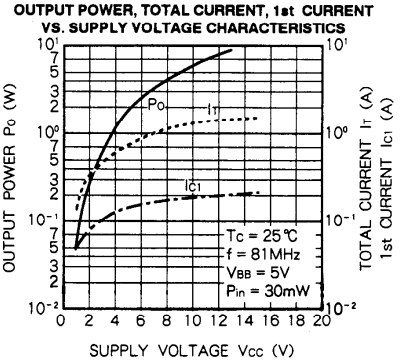

OUTPUT POWER, 2nd CURRENT VS.
1st SUPPLY VOLTAGE CHARACTERISTICS

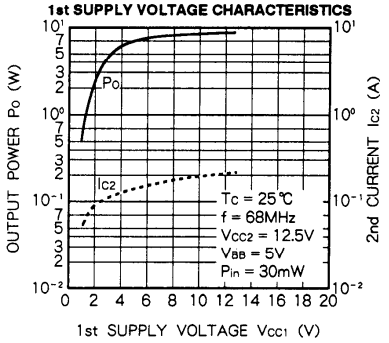

OUTPUT POWER, 2nd CURRENT VS.
1st SUPPLY VOLTAGE CHARACTERISTICS

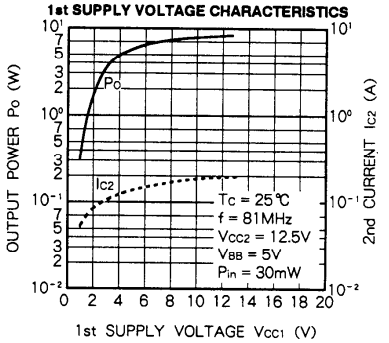

E Real-time phasefront imaging device

This appendix contains a manuscript that we have submitted to Optics Express. It describes the real-time phasefront imaging device that we have developed in Hannover. It can be used to minimize the mismatch between two interfering beams in a heterodyne interferometer and thus further reduce the effect of beam jitter.

Real-time phase front imaging device for heterodyne interferometers

Felipe Guzmán Cervantes, Gerhard Heinzel, Antonio F. García Marín, Vinzenz Wand, Frank Steier and Karsten Danzmann

Max-Planck-Institut für Gravitationsphysik (Albert-Einstein-Institut Hannover), and Institut für Gravitationsphysik, Universität Hannover, Callinstraße 38, 30167 Hannover, Germany

felipe.guzman@aei.mpg.de

Oliver Jennrich

ESA-ESTEC, Keplerlaan 1, Postbus 299, 2200 AG Noordwijk, The Netherlands

Abstract: We have developed an instrument that measures, in real-time, the phase front of a heterodyne interferometer with high spatial resolution (256×320 pixels in a $30\,\mu$m grid). Heterodyne frequencies up to about 10 kHz can be used, and the noise level was measured to be better than 3 mrad rms. This instrument was developed for, and will be used in the construction of, the interferometer to be launched in the LISA Technology Package (LTP).

OCIS codes: (040.2840) Heterodyne, (120.2650) Fringe analysis, (120.3180) Interferometry, (120.5050) Phase measurement, (140.3300) Laser beam shaping, (330.6130) Spatial resolution.

References and links

1. Gerhard Heinzel *et al*, "Interferometry for the LISA technology package (LTP) aboard SMART-2," Classical and Quantum Gravity **20**, 153–161 (2003).
2. Huijie Zhao and Guangjun Zhang, "Nonlinear error by orientation and elliptic polarization in a two-beam interferometer," Optical Engineering **41**, 3204–3208 (2002).
3. Gerhard Heinzel *et al*, "Successful testing of the LISA Technology Package (LTP) interferometer engineering model," Classical and Quantum Gravity **22**, 149–154 (2005).
4. Gerhard Heinzel *et al*, "The LTP interferometer and phasemeter," Classical and Quantum Gravity **21**, 581–587 (2004).
5. David Robertson *et al*, "LTP interferometer-noise sources and performance," Classical and Quantum Gravity **22**, 155–163 (2005).
6. A.E. Siegman, *Lasers* (University Science Books, California, 1986).
7. Yves Surrel, "Fringe Analysis," Topics App. Phys. **77**, 55–102 (2000).
8. Klaus Freischlad and Chris L. Koliopoulos, "Fourier description of digital phase-measuring interferometry," J. Opt. Soc. Am. A. **7**, 542–551 (1990).
9. XFPA-320*256 User Manual, XenICs n.v.,Kapeldreef 75, B-3001 Leuven, Belgium, July 2003.

1. Introduction

Optical heterodyne interferometry is a useful technique to measure distance variations with sub-wavelength precision and large dynamic range. This concept is applied, for example, on LISA Pathfinder [1] which utilizes a set of heterodyne Mach-Zehnder interferometers to measure relative changes in the separation of two drag-free test masses with a noise level better than $10\,\mathrm{pm}/\sqrt{\mathrm{Hz}}$ in the frequency range of 3 mHz to 30 mHz. However, it is well-known that heterodyne interferometers are susceptible to various noise sources such as polarizing effects [2],

spurious beat notes produced by electro-magnetic pick-up induced sideband noise [3], as well as inhomogeneous sensitivity of photodetectors in combination with beam jitter [4, 5]. The latter effect is of particular importance if quadrant photodiodes (QPD) are used (these are often necessary to obtain alignment signals from the interferometer). The error term induced by the spatial inhomogeneity of the detector can be minimized if the interfering beams have identical shape. In order to match the shape of the two beams, it is usual to perform various adjustments that are both complex and time-consuming, based on repeated measurements of beam parameters [6]. This article describes an apparatus that in real-time compares the wavefronts of the interfering beams and thus allows the optimization of the beam shape by measuring the phase front of the interference pattern. It can also be used for the analysis of surfaces and optical components at subnanometer levels.

2. Theoretical Background

2.1. Interference pattern and heterodyne interferometry

The electric field $\mathbf{E}_j(\mathbf{r},t)$ of a linearly polarized light beam can be described as

$$\mathbf{E}_j(\mathbf{r},t) = E_j \mathbf{p}_j \exp\left[i\left(2\pi f_j t + \varphi_j\right)\right] \zeta_j(\mathbf{r}), \tag{1}$$

where j is an index to distinguish several beams with vector $\mathbf{p}_j$ describing the polarization, E_j is the amplitude of the electric field, and $\zeta_j(\mathbf{r})$ is a function describing its spatial distribution. The interference pattern $\mathbf{E}_{\text{total}}(\mathbf{r},t)$ resulting from the recombination of two slightly frequency-shifted electric fields $\mathbf{E}_1(\mathbf{r},t)$ and $\mathbf{E}_2(\mathbf{r},t)$ is given by

$$\begin{aligned} \mathbf{E}_{\text{total}}(\mathbf{r},t) &= \mathbf{E}_1(\mathbf{r},t) + \mathbf{E}_2(\mathbf{r},t) \\ &= E_1 \mathbf{p}_1 \exp\left[i\left(2\pi f_1 t + \varphi_1\right)\right] \zeta_1(\mathbf{r}) + \\ &\quad E_2 \mathbf{p}_2 \exp\left\{i\left[2\pi\left(f_1 + f_{\text{het}}\right) t + \varphi_2\right]\right\} \zeta_2(\mathbf{r}), \end{aligned} \tag{2}$$

where f_{het} is the frequency difference between the two electric fields (heterodyne frequency). The intensity distribution $I(\mathbf{r},t)$ of the interference pattern is proportional to $|\,\mathbf{E}_{\text{total}}(\mathbf{r},t)\,|^2$. Assuming identical polarization vectors $\mathbf{p}_1 = \mathbf{p}_2$, the heterodyne component can be described as

$$I(\mathbf{r},t) = A(\mathbf{r})\left[1 + C(\mathbf{r})\cos\left(2\pi f_{\text{het}} t - \varphi(\mathbf{r})\right)\right], \tag{3}$$

where $A(\mathbf{r})$ is a position-dependent factor, $C(\mathbf{r})$ describes the contrast in terms of the position,

$$\varphi(\mathbf{r}) = \varphi_1 - \varphi_2 + \psi(\mathbf{r}) \tag{4}$$

gives the position dependence of the phase, and $\psi(\mathbf{r})$ is a spatial distortion of the phase distribution. The term $\varphi_1 - \varphi_2$ is the desired physical quantity to be measured, describing the pathlength difference ΔL between the two interfering beams:

$$\Delta L = \frac{\lambda}{2\pi}\left(\varphi_1 - \varphi_2\right), \tag{5}$$

where $\lambda = c/f$ is the wavelength of the light. The factors $A(\mathbf{r})$, $C(\mathbf{r})$, and $\psi(\mathbf{r})$ depend on the parameters E_1, E_2, $\zeta_2(\mathbf{r})$, and $\zeta_2(\mathbf{r})$ of the interfering beams. The photocurrent, $I_{\text{PD}}(t)$, measured by a photodetector (PD) is given by

$$I_{\text{PD}}(t) = \int_{\text{PD}} \eta(\mathbf{r})\, I(\mathbf{r},t)\, d\text{S}, \tag{6}$$

where $\eta(\mathbf{r})$ is the position-dependent quantum-efficiency of the photodetector. Ideally, $I_{\mathrm{PD}}(t)$ would be given by

$$I_{\mathrm{PD}}(t) = \overline{I}\left[1 + C\cos\left(2\pi f_{\mathrm{het}} t - (\varphi_1 - \varphi_2)\right)\right],\ 0 \le c \le 1, \tag{7}$$

and its phase $\varphi_1 - \varphi_2$ would be a faithful measurement of ΔL. In reality, however, the photocurrent is described by the more complex expressions given in equations 3 to 6.

2.2. Spatially resolved phase measurement

The relative geometry of two interfering beams can be described by the spatial structure of the functions $A(\mathbf{r})$, $c(\mathbf{r})$, and $\psi(\mathbf{r})$. The apparatus described here measures these three functions in the real-time interference pattern using a CCD camera and pixelwise data processing. In order to obtain the phase, ϕ, of a sinusoidal function, $y(t)$, given by

$$y(t) = \overline{y}\left(1 + C\cos\left(2\pi f t - \phi\right)\right), \tag{8}$$

several mathematical approaches [7] can be used that are based on measuring n equidistant samples $y_k = y(t_k)$, with $t_k = k\Delta t$. The approach chosen for this experiment is a 4-point algorithm [8], which corresponds to a straightforward Discrete Fourier Transform (DFT) of the signal with $n = 4$ samples and $\Delta t = T/4$, where $T = 1/f$ is the period of the signal. Then, the phase, ϕ, can be calculated from the samples $y_0 \ldots y_3$ by

$$\phi = \arctan\left(\frac{y_3 - y_1}{y_0 - y_2}\right). \tag{9}$$

The interference pattern is sampled with a CCD camera and the spatial distribution of the phase is measured by applying this algorithm pixelwise to the intensities $I_0 \ldots I_3$ captured synchronously at every pixel. For a noise-free signal, these intensities would be given by

$$I_k = I_{\mathrm{avg}}\left(1 + C\cos\left(\varphi + k\frac{\pi}{2}\right)\right), \tag{10}$$

where I_{avg} is the average of the sampled intensities.
Several useful quantities can be obtained from these data:

- Phase at the pixel γ:

$$\varphi_\gamma = \arctan\left(\frac{I_3^{(\gamma)} - I_1^{(\gamma)}}{I_0^{(\gamma)} - I_2^{(\gamma)}}\right). \tag{11}$$

- Contrast at the pixel γ:

$$C_\gamma = 2\,\frac{\sqrt{\left(I_0^{(\gamma)} - I_2^{(\gamma)}\right)^2 + \left(I_3^{(\gamma)} - I_1^{(\gamma)}\right)^2}}{I_0^{(\gamma)} + I_1^{(\gamma)} + I_2^{(\gamma)} + I_3^{(\gamma)}}. \tag{12}$$

- Total phase over the CCD surface:

$$\varphi_{\mathrm{total}} = \arctan\left(\frac{\sum_\gamma\left(I_3^{(\gamma)} - I_1^{(\gamma)}\right)}{\sum_\gamma\left(I_0^{(\gamma)} - I_2^{(\gamma)}\right)}\right). \tag{13}$$

- Total contrast over the CCD surface:

$$C_{\mathrm{total}} = 2\,\frac{\sqrt{\left(\sum_\gamma\left(I_0^{(\gamma)} - I_2^{(\gamma)}\right)\right)^2 + \left(\sum_\gamma\left(I_3^{(\gamma)} - I_1^{(\gamma)}\right)\right)^2}}{\sum_\gamma\left(I_0^{(\gamma)} + I_1^{(\gamma)} + I_2^{(\gamma)} + I_3^{(\gamma)}\right)}. \tag{14}$$

- Average intensity at the pixel γ:

$$I_{\text{avg}}^{(\gamma)} = \frac{I_0^{(\gamma)} + I_1^{(\gamma)} + I_2^{(\gamma)} + I_3^{(\gamma)}}{4}. \tag{15}$$

- The maximum and minimum intensity for the set of exposures ($I_0 \ldots I_3$) can be also determined for diagnostic purposes.

Furthermore, an exposure of the dark fringe can be directly captured by triggering the CCD camera with the appropriate delay τ_{df}:

$$\tau_{\text{df}} = \frac{3\pi/2 - \varphi_{\text{total}}}{2\pi} T_{\text{het}}. \tag{16}$$

3. Instrument components and setup

The interferometer configuration used in this experiment is a non-polarizing heterodyne Mach-Zehnder interferometer. The light source is a Nd:YAG NPRO laser with a wavelength of 1064 nm. Two acousto-optic modulators (AOM), driven by slightly frequency shifted RF signals near 80 MHz, are used to generate two laser beams with a frequency difference of $f_{\text{het}} \approx 1623\,\text{Hz}$. Since the diffraction orders of such modulated light present a non-gaussian distorted beam profile, single-mode polarization-maintaining fiber optics are used as mode cleaners. In order to obtain a high spatial resolution for the phase measurement, a CCD camera is used to sample the interference pattern. The algorithm given in equation 11 is applied pixel-wise on the intensities sampled at every pixel. The CCD camera needs to fulfill the following requirements for this application:

- Simultaneous exposure for every pixel ("global shutter").
- The exposure time must be very short compared with the heterodyne period, $T_{\text{het}} \approx 1/1623\,\text{Hz} = 616\,\mu\text{s}$.
- The camera must be able to be triggered externally to allow frames to be captured at the required instances of time.
- The signal for each pixel needs to be proportional to the intensity on that pixel. Saturation effects, such as "blooming", must be avoided.

The CCD camera used is a model XEVA-USB from XenICs [9] with a 12-bit dynamic range that reaches 30 frames per second (fps) at a resolution of 320×256 pixels with a pixel pitch of $30\,\mu$m. The photosensitive chip is made of InGaAs, which has a high quantum efficiency for the near infrared (0.9–1.7 μm). The exposure time used is $1\,\mu\text{s}\,(1/616\,T_{\text{het}})$. Ideally, the interference pattern should be sampled 4 times within a single heterodyne period of T_{het}. This would require a sampling period of $\Delta t = 154\,\mu\text{s}$ (approximately 6500 fps) for the CCD camera which cannot be reached in practice due to the time required to transfer the image. Hence, an integer number m of heterodyne periods T_{het} is added to Δt. Thus, the trigger signal to capture the intensity sample I_k is sent to the CCD camera with the delay

$$\Delta t_k = m\,T_{\text{het}} + \tau_k. \tag{17}$$

with $\tau_k = k\,T_{\text{het}}/4$. The experimental setup is outlined in Figure 1. In practice, the environment is not stable enough to preserve a constant phase relationship over many periods of f_{het}. Hence, additional circuitry is used to re-synchronize the trigger timing electronics with the actual phase of the heterodyne signal: A single-element diode (SED) is located at the second output of the interference beamsplitter where the same interference pattern emerges with a 180° phase shift. The heterodyne signal measured by the SED is bandpass filtered and digitized by a comparator.

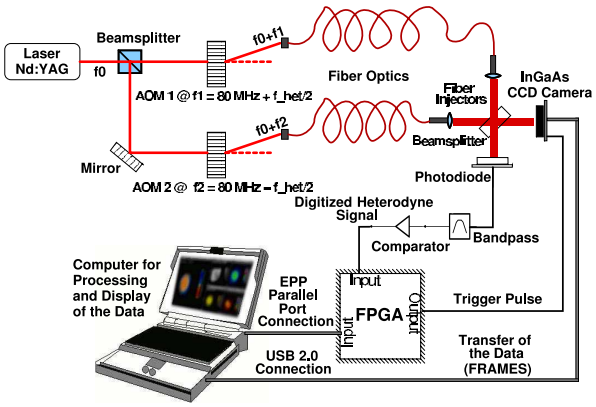

Fig. 1. Experimental setup used for the phasemeter.

The rising edge of this digital signal is used to trigger the timing control electronics that resides in a Field Programmable Gate Array (FPGA). In order to capture the frame k, the FPGA triggers the camera with the very well-controlled delay τ_k with respect to this rising edge (see Figure 2). A parallel-port-interface was also included in the FPGA in order to control the trigger sequence.

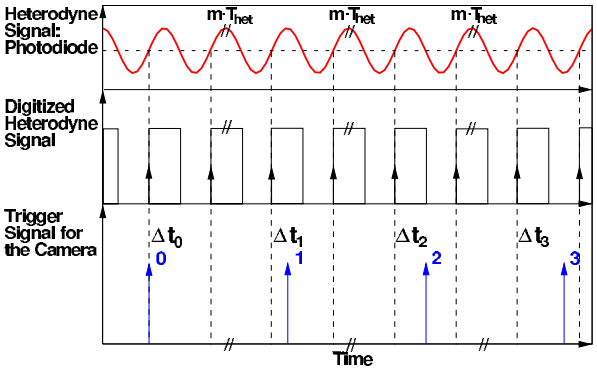

Fig. 2. Time diagram of the signals processed to trigger the CCD camera.

When the phasemeter software is ready to receive a frame, a command is sent from the PC to the FPGA through the parallel port, which includes the corresponding delay τ_k. The FPGA waits for the next rising edge and then sends a trigger pulse to the CCD camera delayed by τ. The CCD camera captures the frame and transfers it to the PC through its USB 2.0 interface. After all four frames have been acquired, the phasemeter software proceeds to compute the physical quantities described in equations 11 to 15, and an additional exposure is captured by triggering the camera with a delay τ_{df} given by equation 16, which corresponds to an exposure of the dark fringe.

4. Results

A graphical user interface (GUI) was developed to display the measured data in real-time (see Figure 3). The phasemeter reaches a rate of approx. 5 to 6 data displays per second, and hence allows real-time optical alignment of an interferometer and optimal adjustment of its components. The five different displays in Figure 3 are shown separately as 3D representations in Figures 4 to 8. These measurements were conducted on a tabletop fiber-coupled Mach-Zehnder interferometer.

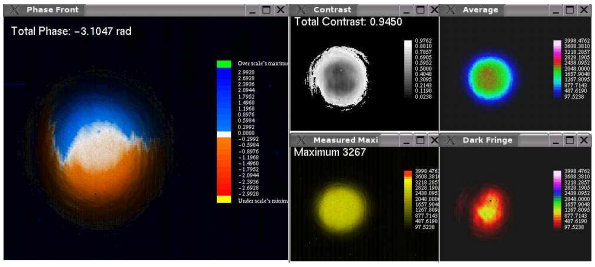

Fig. 3. Graphical User Interface programmed to display the measured data in real-time.

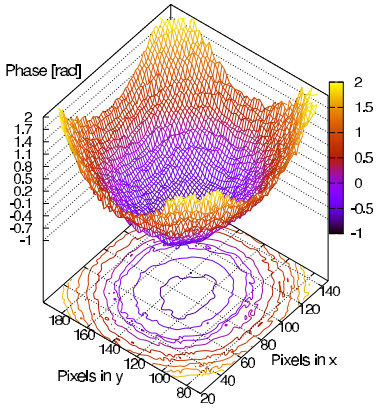

Fig. 4. Spatial Distribution of the Phase.

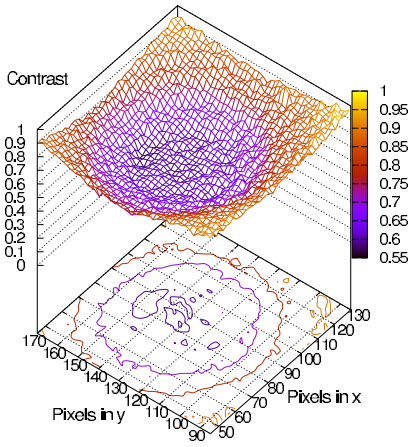

Fig. 5. Spatial Distribution of the Contrast.

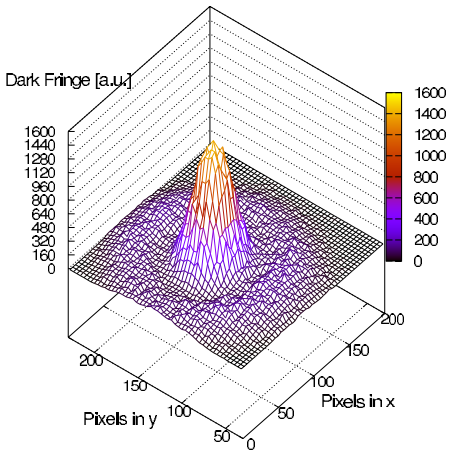

Fig. 6. Exposure of a Dark Fringe.

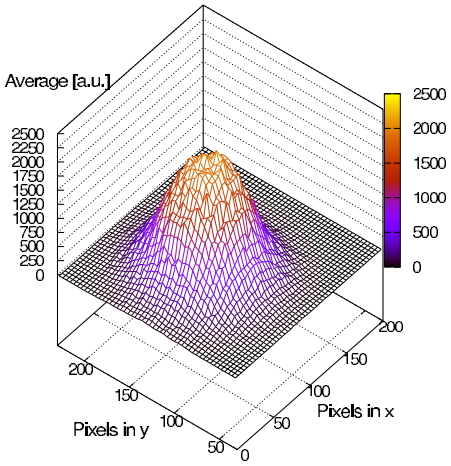

Fig. 7. Average intensity over 4 exposures.

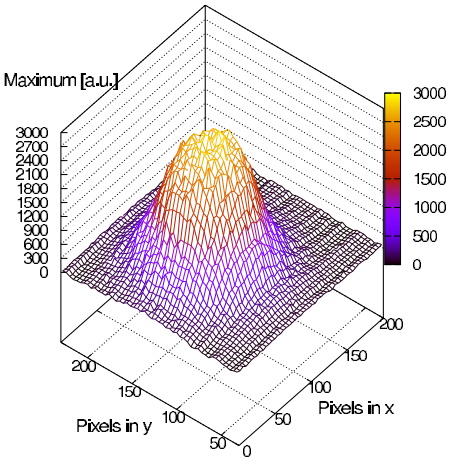

Fig. 8. Maximum intensity over 4 exposures.

4.1. Performance of the phasemeter

As can be seen in equation 9, one noise source of the phase measurement is the fluctuation of the sampled intensities. The rms error of the phase, $\Delta\varphi_{\mathrm{rms}}$, induced by intensity fluctuations ΔI_{rms} can be estimated from equation 11 as:

$$\Delta\varphi_{\mathrm{rms}} = \sqrt{\sum_k \left(\frac{\partial\varphi}{\partial I_k}\right)^2}\,\Delta I_{\mathrm{rms}} = \sqrt{\frac{2}{(I_0 - I_2)^2 + (I_1 - I_3)^2}}\,\Delta I_{\mathrm{rms}}. \tag{18}$$

After simplifying equation 18 by using equation 10, we obtain:

$$\Delta\varphi_{\mathrm{rms}} = \frac{\sqrt{2}}{C}\,\frac{\Delta I_{\mathrm{rms}}}{I_{\mathrm{avg}}}. \tag{19}$$

The main error sources influencing this phase measurement procedure are listed in Table 4.1. They are:

- Laser power fluctuations: An Allan deviation of 8.6×10^{-4} was measured at an averaging time of 33 ms, which corresponds to the sampling period of the CCD camera (30 fps), yielding a phase error of 1.22 mrad from equation 19.
- ADC digital noise of the camera: A rms intensity error of 4 quantization units was measured by constant and spatially homogeneous illumination of the CCD camera. The pixelwise rms variation and an average over the CCD surface were then computed. This value corresponds to a relative intensity fluctuation of 9.76×10^{-4} and to a phase error of 1.38 mrad.
- Time jitter: There are at least three sources of jitter. The synchronization delay of the comparator output with respect to the 10 MHz clock of the FPGA, which is uniformly distributed between 0 and 100 ns. Secondly, a similar delay between the FPGA clock and the CCD internal clock, which is also at 10 MHz but unsynchronized, and thirdly other jitter effects. A phase error of 0.99 mrad was obtained by simulating the first and second effects in software, using two independent random delays with uniform distribution.

Table 1. Main noise sources of the phase measurement.

Noise Source	**RMS Phase Error**
Laser power fluctuations	1.22 mrad
ADC digital noise of the camera	1.38 mrad
Time jitter	0.99 mrad
RMS sum	$\sqrt{1.22^2 + 1.38^2 + 0.99^2}$
Total phase error expected	**2.09 mrad**

In order to measure the real noise level of the instrument, the camera was illuminated with a homogeneous light source, whose intensity was modulated sinusoidally at a frequency of approximately 1623 Hz. A rms phase error of 2.96 mrad was obtained from this measurement. According to equation 5, this value corresponds to a rms spatial resolution of about 500 pm.

4.2. Measurements

A phase front measurement was conducted on the engineering model of the optical bench for LISA Pathfinder [1, 3]. These results are presented in Figure 9 and clearly show an inhomogeneous phase front, which can be attributed to unequal focal lengths of the two fiber injectors.

A further test was done in order to perform an adjustment of the lenses in the two fiber injectors on a table top interferometer by using this instrument. The aim of this adjustment was to match the parameters of the interfering beams and to obtain a homogeneous phase front. The result of this experiment is shown in Figure 10. It can be seen that over a surface of approxi-

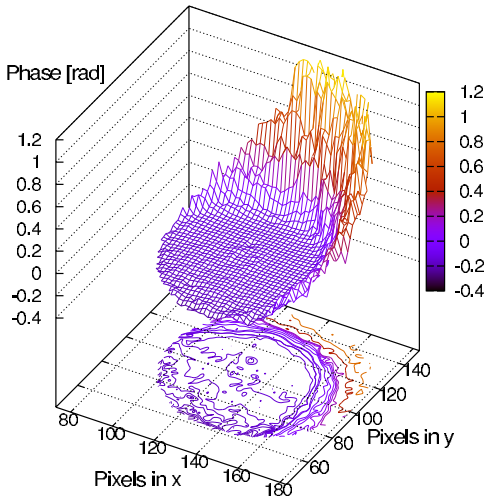

Fig. 9. Phase front measured on the engineering model of the optical bench for LISA Pathfinder.

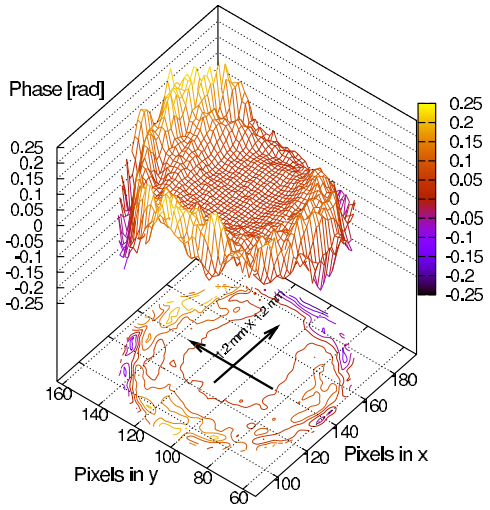

Fig. 10. Adjusted phase front measured on a tabletop fiber-coupled Mach-Zehnder interferometer.

mately 1.2 mm×1.2 mm the phase front presents a reasonably homogeneous spatial profile. A circular section of approximately 1 mm diameter at the beam center was analyzed. The standard deviation of these data is 3.49 mrad, which is very close to the measured sensitivity of the instrument. This value corresponds to a spatial resolution of 590 pm, which amounts to a considerable improvement in the adjustment of the beam shapes.

5. Conclusions

We have developed an instrument that allows the comparison of the wavefronts of two interfering beams in a heterodyne interferometer by measuring the phase front of their interference pattern simultaneously over 256×320 pixels. A rms noise level of 2.96 mrad, which corresponds to a wavefront roughness of 500 pm, was experimentally obtained. This makes it possible to optimize the beam shapes by adjusting the optical components in real-time with the help of the data displayed onto the graphical user interface (5 to 6 data displays per second). By using well matched wavefronts, this instrument can be also applied to analyze, and measure accurately, surfaces and optical components down to subnanometer levels. It is planned that this instrument be used in the production of the flight model of the optical bench for LISA Pathfinder.

6. Acknowledgement

The authors kindly thank Albrecht Rüdiger, Martin Hewitson, and Alexander Bunkowski for their valuable contributions in reviewing and improving various parts of the manuscript.

F Effects of photodiode offsets

This appendix reprints a document produced in Glasgow concerning the effects of photodiode offset in conjunction with beam jitter.

LTP Project
Institute for Gravitational Research
Department of Physics and Astronomy
University of Glasgow
Glasgow G12 8QQ, Scotland

Document	**S2-UGL-TN-3012**
Title	**Photodiode Positional Offsets**
Issue	**1.0**
Date	**26 Sept 2005**

Prepared by .....Harry Ward

Approved by .....David Robertson

TABLE OF CONTENTS

1 INTRODUCTION

This document is intended to provide details of the required alignment accuracy of the principal measurement photodiodes with respect to the incident beams. Although the interfering beams are significantly smaller than the active area of the photodiodes, the presence of the inactive slits that divide the diodes into quadrants allows, in the presence of beam decentre, coupling of residual beam mismatches to apparent phase shifts. In this document we report on numerical simulations that assess the significance of these couplings and conclude requirements on beam centring.

All simulations are conducted in MATLAB, using functions provided by an additional optical toolbox – Lightpipes.

An alternative 1D analytical simulation is also described. The results of the two approaches agree to within 10% for a simple case of a relative beam tilt mismatch. This gives confidence that the Lightpipes 2D simulations can be trusted when they model the more realistic combinations of beam mismatches that might occur in LTP.

Throughout an optical wavelength λ=1064 nm is assumed.

The beam pictures used throughout are stills taken from movies produced by the modelling software. These movies will only play if the relevant files are present alongside the Word version of this document. The movies are not necessary to the understanding of the document.

2 EFFECTS OF VARIOUS OFFSETS

2.1 SIMPLEST CASE: RELATIVE BEAM TILT

Beams matched in size and curvature and position, but relatively tilted at the quadrant photodiode. Relative path lengths swept by one lambda to generate plots. Relative phase of length sweep and interference signal printed out by function as "angletotal" (in radians).

Function: `tilt4.m`

```
tilt4(grid, gridsize, steps, w, tilt, orientation, z1, z2,
PDslitwidth, PDradius, PDxoffset, PDyoffset, doplots, movienum)
```

Example : (all simulations done for a PD uniform circular active-area diameter of 4mm)

```
tilt4(8,6e-3,100,700e-6,200e-6,0,1e5,1e5,50e-6,2e-3,200e-6,0e-6,0,1)
```

`angletotal = -8.3989e-008` with no lateral PD offsets

Now try a 200 micron PD offset

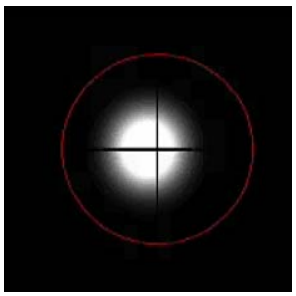

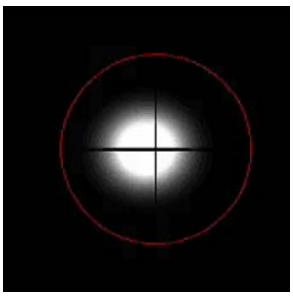

x offset, x tilt

`angletotal =-0.0096`

x offset, y tilt

`angletotal = -8.5536e-008`

(Note: similar results when grid increased to 2^10 or when steps increased to 100)

So with a relative beam tilt of 200μrad and PD offset of 200μm the worst-case resulting phase error is about 10mrad for typical beam and PD sizes and PD slit width.

We can express this coupling factor as

0.25μrad of phase shift / μrad relative beam tilt / μm PD offset.

Before drawing conclusions, check what happens if we make the slit of zero width using

`tilt4(8,6e-3,30,700e-6,50e-6,0,3e5,3e5,0e-6,2e-3,200e-6,0e-6,1,30)`.

Result is `angletotal = 4.2047e-004` for a beam relative tilt of 200μrad and a PD offset of 200μm in the (worst-case of the) same direction. This is due to the beam beginning to fall off the diode slightly, but this is a much smaller effect than appears when we use a quadrant diode with a slit width of 50μm.

A further check is to see how the error using a quadrant detector behaves as the PD lateral offset is reduced. The answer is that (at these small offsets) the phase error scales linearly.

So what does this mean for LTP? Typically we will be using interferometer signals to keep the test masses relatively aligned, so we have to concern ourselves with the DC error in such a system and the spectral density of residual angular fluctuations that there will be in the signal band. Typically we don't care about a pure DC term. So knowing the residual tilt noise plus knowing the scaling factor from the simulations, we can set a tolerable PD offset given the overall interferometer noise goal.

In line with numbers provided in discussions with Stefano and with Gerhard, let's postulate a residual tilt noise of 300 nrad/√Hz. Then the noise coupled to the interferometer output will be

[0.25 x 0.3 x PD offset(in microns) /2π] μcycles/√Hz

So a PD offset of 100 microns could result in a noise level of about 1.2 μcycles/√Hz.

Ideally we aim to keep each interferometer noise contribution to a maximum of ~ 1 μcycles/√Hz; this would set a limit to a PD offset of about 80 μm maximum.

2.2 RELATIVE BEAM CURVATURE MISMATCH

Beams matched in position, but propagating different distances from the splitter so that they have different radii of curvature (and sizes) at the quadrant photodiode. Relative path lengths swept by one lambda to generate plots. Relative phase of length sweep and interference signal printed out by function as "angletotal" (in radians).

Check with matched beams that offsetting PD has no effect:

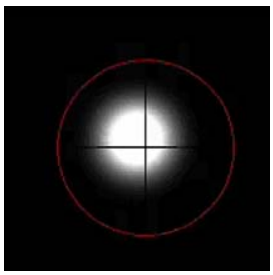

`angletotal = -8.8936e-008`, so negligible effect

Now re-centre the PD and change relative propagation distances to 30cm, and 60 cm.

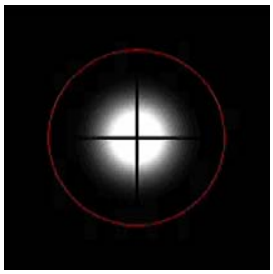

`angletotal = -0.0519` – but this is just the new nominal zero phase for this particular beam mismatch.

The question is by how much this changes if we offset the PD. This will vary slightly with different beam propagation distances, but in general the phase shift is of order 1mrad for 200μm PD offset. For example, the following result is with a 200μm PD offset with a 30cm/60cm difference in propagation from a 700μm waist. (In LPF we could, if justified, try to balance the curvatures better than this for the most sensitive measurement recombination point.)

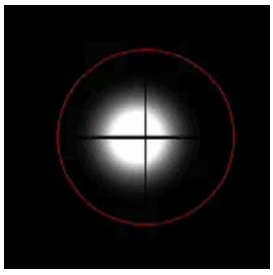

`angletotal = -0.0528`

The question is then what happens in LTP. Static curvature errors produce only a DC term in the apparent relative phase signals and so are not a particular concern. But we do have to worry about the combined effects of curvature mismatch and relative angular tilts – and also lateral displacements – of the interfering beams.

Let's try a simple example of a curvature mismatch (30cm/60cm propagation lengths) with a 200µrad relative beam tilt and a 200µm PD offset. Starting with zero PD offset to get the nominal phase zero:

`angletotal = -0.0613`

Now offset the PD in same direction as tilt: `angletotal = -0.0714`

So this phase shift of 10mrad is the same as we saw for a simple tilt with no curvature error.

2.3 RELATIVE BEAM POSITION MISMATCH

The foregoing discussions have dealt with beams that were perfectly overlapped in lateral position at the point of detection. In LTP there will typically be some lateral component to the overall misalignment of the beams due to inbuilt imperfections of the interferometer. Furthermore, while the feedback to the proof masses will tilt them to attempt to the null the differential wavefront sensing signals, the origin of an overall tilt error will typically be distributed throughout the interferometer and so correction by pivoting at a point will leave a situation in which the interfering beams have some relative lateral offset.

So the question is, given a lateral offset, what centring of the PD is necessary to keep the coupling of residual tilt noise of the proof masses at a tolerable level.

To get an idea of scale, let's model a case in which the tilt of a proof mass is used to "correct" an inbuilt tilt of 100µrad (e.g in the vertical) acquired elsewhere in the fixed components of the interferometer system. This could result in a lateral offset at a PD 0.5m away of, say, 50µm. For now we assume equal 30 cm paths.

This model is done using

Function: `shift4.m`

```
shift4(grid, gridsize, steps, w, xbeamshift, ybeamshift,  z1, z2,
PDslitwidth, PDradius, PDxoffset, PDyoffset, doplots, movienum)
```

Results: (computed with grid=10, steps=2)

For PD offset of 25µm, phase shift ~ 2E-5 rad / 100µm relative lateral beam offset in the worst-case (i.e. same) direction.

For PD offset of 50µm, phase shift ~ 4E-5 rad / 100µm relative lateral beam offset in the worst-case (i.e. same) direction.

For PD offset of 100µm, phase shift ~ 9E-5 rad / 100µm relative lateral beam offset in the worst-case (i.e. same) direction.

For PD offset of 200µm, phase shift ~ 16E-5 rad / 100µm relative lateral beam offset in the worst-case (i.e. same) direction.

We can express this coupling factor as

90 µrad of phase shift / 100 µm relative beam offset / 100 µm PD offset.

While our potential value of 50 μm relative beam offset is a DC value and will therefore not be so significant, we can expect the 300 nrad/√Hz residual proof mass tilt noise to result in a lateral beam displacement noise (assuming tight feedback control to null the DWS signals) of perhaps 150 nm/√Hz. Then the noise coupled to the interferometer output will be

[90 x 1.5e-5 x PD offset(in microns) /2π] μcycles/√Hz

So a PD offset of even 100 microns would only result in a negligible noise level of about 0.02 μcycles/√Hz.

Might a DC lateral beam offset affect the coupling of residual beam angle fluctuations? Given the very different scales of significance of the two effects it seems clear that the angular offset coupling would be by far the more dominant.

3 ALTERNATIVE 1D-ANALYTICAL MODEL

As a check on the results obtained using the beam propagation toolbox a simple 1D analytical model has also been developed.

The model deals solely with a relative tilt of two plane wavefronts, of equal radius, and with Gaussian intensity profiles. The model includes the presence of the PD slit and allows lateral offset of the PD centre from the centre of relative rotation of the two beams. The finite size of the PD active area is included in the calculation.

3.1 MATLAB CALCULATION

The function that is used to represent the interference of the two beams is

```
function y = tiltvis2(x)
global w ang lambda phase;

y = (1/sqrt(pi)/w)*exp(-
x.^2/w^2).*(1+cos(phase+(2*pi*x*ang/lambda)));
```

where the function returns a value proportional to the intensity at position x along the x-axis, given the beam radius w, the wavelength lambda, the relative tilt angle ang and the relative phase between the two beams at the point about which the beams are pivoted.

This function is then integrated appropriately over ranges determined by the PD size, slit width and offset. This is performed in the function

```
function [totalvis, angletotal] = runvis2(steps, beamwidth,relangle,
PDradius, PDslitwidth, PDoffset);

global w ang lambda phase;

lambda=1.064e-6;
ang=relangle;
w=beamwidth;

for step=0:steps;

phase=2*pi*(step/(steps+1));
TotalI(step+1) = 2*(quad(@tiltvis2,-PDradius+PDoffset,PDoffset-
PDslitwidth/2)+quad(@tiltvis2,PDoffset+PDslitwidth/2,PDoffset+PDradiu
s));
```

```
end


spectotal=fft(TotalI);
totalvis=abs(spectotal(2))*2/spectotal(1);
angletotal=angle(spectotal(2))
```

which returns the apparent phase shift (with respect to the zero actual phase at the beam centre (x=0) point).

3.2 RESULTS

We apply the analytical calculation to the example dealt with earlier in section 2.1. There we modeled a 200μrad relative beam tilt using

```
tilt4(grid, gridsize, steps, w, tilt, orientation, z1, z2,
PDslitwidth, PDradius, PDxoffset, PDyoffset, doplots, movienum)
```

Example : (all simulations done for a PD uniform circular active-area diameter of 4mm)

```
tilt4(8,6e-3,100,700e-6,200e-6,0,1e5,1e5,50e-6,2e-3,200e-6,0e-6,0,1)
```

from which, with a 200μm PD offset in the x-direction we got the result

```
angletotal =-0.0096
```

To enable a strict comparison with the 1D analytical model we repeat the tilt4 2D model with zero values for the z1 and z2 propagation distances. This yields the same result.

Now performing the 1D calculation using

```
runvis2(4,700e-6,200e-6,2e-3,50e-6, 200e-6)
```

gives

```
angletotal =   -0.0106
```

The agreement is reasonable and gives confidence that the 2D model can be used to give reasonably accurate (at he 10% level) results for cases of more realistic superpositions of beam mismatches.

4 CONCLUSION

Relative tilt noise of the interfering beams sets the most stringent requirement on beam centring on a quadrant photodiode. With a 300 nrad/√Hz residual in-band tilt noise, a 50 μm photodiode slit width and assuming a tolerable noise contribution from the effect, **we conclude that the maximum tolerable decentre of the main measurement photodiodes is 80 μm**.

5 ACRONYMS

PD Photodiode

LTP LISA Technology Package

DWS Differential Wavefront Sensing

6 PROGRAMS

6.1 TILT4.M

```
function [totalvis,avesegvis] = tilt4(grid, gridsize, steps, w, tilt,
orientation, z1, z2, PDslitwidth, PDradius, PDxoffset, PDyoffset,
doplots, movienum)


% This first part of the programme defines the grid size
% and the physical parameters of the beam


%clear all;
close all;
m=1;
cm=.01*m;
mm=0.001*m;
nm=1e-9*m;
%gridsize=5*mm;
lambda=1064*nm;
n=grid;
N=2^n
N2=N/2;


% generate PD outline coordinates for drawing on display
nop=50;
style='r-';


PDxshift=round(PDxoffset/gridsize*N)
PDyshift=round(PDyoffset/gridsize*N)


PDslit=round(PDslitwidth/gridsize*N)


theta=linspace(0,2*pi,nop);
rho=ones(1,nop)*PDradius/gridsize*N;
[X,Y] = pol2cart(theta,rho);
xpd=X+1+N2+PDxshift;
ypd=Y+1+N2+PDyshift;
```

```
% Set up relative beam tilt at the correct orientation angle
rel_tilt_angle=tilt;
tilt_orientation=orientation;
orient=tilt_orientation/180*pi;


tx=rel_tilt_angle*cos(orient);        % relative x tilt angle between
beams at recombination
ty=rel_tilt_angle*sin(orient);        % relative y tilt angle between
beams at recombination


%Generate beams
z1=z1*lambda;    % beam 1 propagation distance before recombination
z2=z2*lambda;    % beam 2 propagation distance before recombination
RBS=0.5;         % beam splitter ratio


% Here we create a Gaussian beam (at the centre of the grid) from a
planar beam, and then
% propagate it a distance z0

    F1=LPBegin(gridsize,lambda,N);
    F1=LPGaussAperture(w,0,0,1,F1);


% We then split the Gaussian beam to create two coherent
% beams which are then (symmetrically) relatively tilted


    F_1=LPIntAttenuator(RBS,F1);
    F_1=LPForvard(z1,F_1);
    F_1=LPTilt(tx/2,ty/2,F_1);


    F_2=LPIntAttenuator(1-RBS,F1);
    F_2=LPForvard(z2,F_2);
    F_2=LPTilt(-tx/2,-ty/2,F_2);


% Now generate the interference signal
% Beam 2 is stepped forward over 1 wavelength to map out the
% interference fringe.
```

```
for step=0:steps;

% The two Gaussian beams are then combined and the
% the beam pattern analysed by a (possibly offset) quadrant detector

  F_sum=LPBeamMix(F_1,F_2);

% now screen so that the beam is only shown on the PD active areas

  F_sum=LPRectScreen(PDslitwidth,gridsize,PDxoffset,0,0,F_sum);
  F_sum=LPRectScreen(gridsize,PDslitwidth,0,PDyoffset,0,F_sum);
  F_sum=LPCircAperture(PDradius,PDxoffset,PDyoffset,F_sum);

  IntensityR=LPIntensity(0,F_sum);

 % accumulate data into arrays for later processing to vield
visibilities and phase shifts

    TotalI(step+1)=sum(sum(IntensityR));



    Int_Q1(step+1)=sum(sum(IntensityR(1:N2+PDyshift,
1:N2+PDxshift)));
    Int_Q2(step+1)=sum(sum(IntensityR(1:N2+PDyshift,
N2+PDxshift+1:N)));
    Int_Q3(step+1)=sum(sum(IntensityR(N2+PDyshift+1:N,
1:N2+PDxshift)));
    Int_Q4(step+1)=sum(sum(IntensityR(N2+PDyshift+1:N,
N2+PDxshift+1:N)));


 % step forward to get next element of the interference fringe


    F_2=LPForvard(1*lambda/(steps+1),F_2);

    if doplots==1


    figure(step+1);
    imagesc(IntensityR,[0 1]); colormap(gray)
```

```
    hold;
    plot(xpd,ypd,style);
    axis square

    M(step+1)=getframe;

end
end

if doplots==1
 movie(M,1);
 moviename=['movie', num2str(movienum),'.avi'];
 movie2avi(M,moviename)
end



% Now FFT the values of a fringe over one cycle to get the dc and
fundamental amplitude
% This allows calculation  of the waveform phase (wrt the pathlength
modulation phase) and the fringe visibility


TotalI-(Int_Q1+Int_Q2+Int_Q3+Int_Q4);


specQ1=fft(Int_Q1);
specQ1(1);
visQ1=abs(specQ1(2))*2/specQ1(1)
angleQ1=angle(specQ1(2))

specQ2=fft(Int_Q2);
specQ2(1);
visQ2=abs(specQ2(2))*2/specQ2(1)
angleQ2=angle(specQ2(2))

specQ3=fft(Int_Q3);
specQ3(1);
visQ3=abs(specQ3(2))*2/specQ3(1)
angleQ3=angle(specQ3(2))
```

```
specQ4=fft(Int_Q4);
specQ4(1);
visQ4=abs(specQ4(2))*2/specQ4(1)
angleQ4=angle(specQ4(2))


spectotal=fft(TotalI);
totalvis=abs(spectotal(2))*2/spectotal(1);
angletotal=angle(spectotal(2))

avesegvis=(visQ1+visQ2+visQ3+visQ4)/4



I_LR=Int_Q1+Int_Q2-Int_Q3-Int_Q4;
I_UD=Int_Q1+Int_Q3-Int_Q2-Int_Q4;

%figure;
%plot(TotalI);
%figure;
%plot(I_LR);
%figure;
%plot(I_UD);

% diff=TotalI-(Int_Q1+Int_Q2+Int_Q3+Int_Q4)
```

6.2 SHIFT4.M

```
function [visTotal,avesegvis] = shift4(grid, gridsize, steps, w,
xrelbeamshift, yrelbeamshift, z1, z2, PDslitwidth, PDradius,
PDxoffset, PDyoffset, doplots, movienum)


% This first part of the programme defines the grid size
% and the physical parameters of the beam


%clear all;
close all;
m=1;
cm=.01*m;
mm=0.001*m;
nm=1e-9*m;
%gridsize=5*mm;
lambda=1064*nm;
n=grid;
N=2^n
N2=N/2;


% generate PD outline coordinates for drawing on display
nop=50;
style='r-';


PDxshift=round(PDxoffset/gridsize*N)
PDyshift=round(PDyoffset/gridsize*N)


PDslit=round(PDslitwidth/gridsize*N)


theta=linspace(0,2*pi,nop);
rho=ones(1,nop)*PDradius/gridsize*N;
[X,Y] = pol2cart(theta,rho);
xpd=X+1+N2+PDxshift;
ypd=Y+1+N2+PDyshift;
%Generate beams
z1=z1*lambda;    % beam 1 propagation distance before recombination
```

```
z2=z2*lambda;    % beam 2 propagation distance before recombination

% Here we create two, equal intensity, Gaussian beams from a planar
beam, and then
% propagate them distances z1 and z2 respectively

    F1=LPBegin(gridsize,lambda,N);
    F_1=LPGaussAperture(w,-xrelbeamshift/2,-yrelbeamshift/2,1,F1);
    F_2=LPGaussAperture(w,+xrelbeamshift/2,+yrelbeamshift/2,1,F1);
    F_1=LPForvard(z1,F_1);
    F_2=LPForvard(z2,F_2);
    clear F1;

% Now generate the interference signal
% Beam 2 is stepped forward over 1 wavelength to map out the
% interference fringe.

for step=0:steps;

% The two Gaussian beams are then combined and the
% the beam pattern analysed by a (possibly offset) quadrant detector

  F_sum=LPBeamMix(F_1,F_2);

% now screen so that the beam is only shown on the PD active areas

  F_sum=LPRectScreen(PDslitwidth,gridsize,PDxoffset,0,0,F_sum);
  F_sum=LPRectScreen(gridsize,PDslitwidth,0,PDyoffset,0,F_sum);
  F_sum=LPCircAperture(PDradius,PDxoffset,PDyoffset,F_sum);

  IntensityR=LPIntensity(0,F_sum);

 % accumulate data into arrays for later processing to yield
visibilities and phase shifts
     TotalI(step+1)=sum(sum(IntensityR));
```

```
    Int_Q1(step+1)=sum(sum(IntensityR(1:N2+PDyshift,
1:N2+PDxshift)));
    Int_Q2(step+1)=sum(sum(IntensityR(1:N2+PDyshift,
N2+PDxshift+1:N)));
    Int_Q3(step+1)=sum(sum(IntensityR(N2+PDyshift+1:N,
1:N2+PDxshift)));
    Int_Q4(step+1)=sum(sum(IntensityR(N2+PDyshift+1:N,
N2+PDxshift+1:N)));

 % step forward to get next element of the interference fringe

    F_2=LPForvard(1*lambda/(steps+1),F_2);

    if doplots==1

    figure(step+1);
    imagesc(IntensityR,[0 1]); colormap(gray)
    hold;
    plot(xpd,ypd,style);
    axis square

    M(step+1)=getframe;

    end
end

if doplots==1
 movie(M,1);
 moviename=['movie', num2str(movienum),'.avi'];
 movie2avi(M,moviename)
end

% Now FFT the values of a fringe over one cycle to get the dc and
fundamental amplitude
% This allows calculation  of the waveform phase (wrt the pathlength
modulation phase) and the fringe visibility

TotalI-(Int_Q1+Int_Q2+Int_Q3+Int_Q4);
```

```
specQ1=fft(Int_Q1);
specQ1(1);
visQ1=abs(specQ1(2))*2/specQ1(1)
angleQ1=angle(specQ1(2))

specQ2=fft(Int_Q2);
specQ2(1);
visQ2=abs(specQ2(2))*2/specQ2(1)
angleQ2=angle(specQ2(2))

specQ3=fft(Int_Q3);
specQ3(1);
visQ3=abs(specQ3(2))*2/specQ3(1)
angleQ3=angle(specQ3(2))

specQ4=fft(Int_Q4);
specQ4(1);
visQ4=abs(specQ4(2))*2/specQ4(1)
angleQ4=angle(specQ4(2))

spectotal=fft(TotalI);
totalvis=abs(spectotal(2))*2/spectotal(1);
angletotal=angle(spectotal(2))

avesegvis=(visQ1+visQ2+visQ3+visQ4)/4
I_LR=Int_Q1+Int_Q2-Int_Q3-Int_Q4;
I_UD=Int_Q1+Int_Q3-Int_Q2-Int_Q4;

%figure;
%plot(TotalI);
%figure;
%plot(I_LR);
%figure;
%plot(I_UD);

% diff=TotalI-(Int_Q1+Int_Q2+Int_Q3+Int_Q4)
```

G A selection of published literature on related subjects

COHEN, SC:
HETERODYNE DETECTION - PHASE FRONT ALIGNMENT, BEAM SPOT SIZE, AND DETECTOR UNIFORMITY
APPLIED OPTICS, Volume **14**, Issue 8, page 1953–1959, **1975**

TAKENAKA, T; TANAKA, K; FUKUMITSU, O:
SIGNAL-TO-NOISE RATIO IN OPTICAL HETERODYNE-DETECTION FOR GAUSSIAN FIELDS
APPLIED OPTICS, Volume **17**, Issue 21, page 3466–3471, **1978**

SAGA, N; TANAKA, K; FUKUMITSU, O:
DIFFRACTION OF A GAUSSIAN-BEAM THROUGH A FINITE APERTURE LENS AND THE RESULTING HETERODYNE EFFICIENCY
APPLIED OPTICS, Volume **20**, Issue 16, page 2827–2831, **1981**

SALZMAN, J; KATZIR, A:
SIGNAL-TO-NOISE RATIO OF HETERODYNE-DETECTION - MATRIX FORMALISM
APPLIED OPTICS, Volume **22**, Issue 6, page 888–890, **1983**

SANIIE, J; LUUKKALA, M:
DIGITAL PHASE DETECTION BASED ON IN-PHASE AND QUADRATURE SAMPLING
JOURNAL OF PHYSICS E-SCIENTIFIC INSTRUMENTS, Volume **16**, Issue 7, page 606–607, **1983**

SCHWIDER, J; BUROW, R; ELSSNER, KE; GRZANNA, J et al:
DIGITAL WAVE-FRONT MEASURING INTERFEROMETRY - SOME SYSTEMATIC-ERROR SOURCES
APPLIED OPTICS, Volume **22**, Issue 21, page 3421–3432, **1983**

TANAKA, M; NAKAYAMA, K:
A NEW OPTICAL INTERFEROMETER FOR ABSOLUTE MEASUREMENT OF LINEAR DISPLACEMENT IN THE SUBNANOMETER RANGE
JAPANESE JOURNAL OF APPLIED PHYSICS PART 2-LETTERS, Volume **22**, Issue 4, page L233–L235, **1983**

BARASH, VY; FEDOTOVA, GV:
HETERODYNE INTERFEROMETER TO MEASURE VIBRATION PARAMETERS
MEASUREMENT TECHNIQUES USSR, Volume **27**, Issue 1, page 50–51, **1984**

GREIVENKAMP, JE:
GENERALIZED DATA REDUCTION FOR HETERODYNE INTERFEROMETRY
OPTICAL ENGINEERING, Volume **23**, Issue 4, page 350–352, **1984**

RATHORE, TS; MOMBASAWALA, LS:
AN ACCURATE DIGITAL PHASE MEASUREMENT SCHEME
PROCEEDINGS OF THE IEEE, Volume **72**, Issue 3, page 397–398, **1984**

SALZMAN, J; KATZIR, A:
HETERODYNE-DETECTION SNR - CALCULATIONS WITH MATRIX FORMALISM
APPLIED OPTICS, Volume **23**, Issue 7, page 1066–1074, **1984**

SIUZDAK, J:
A NOISE RESISTANT PHASEMETER WITH SYNCHRONOUS DETECTION
INTERNATIONAL JOURNAL OF ELECTRONICS, Volume **57**, Issue 5, page 737–743, **1984**

TANAKA, K; SAGA, N:
MAXIMUM HETERODYNE EFFICIENCY OF OPTICAL HETERODYNE-DETECTION IN THE PRESENCE OF BACKGROUND-RADIATION
APPLIED OPTICS, Volume **23**, Issue 21, page 3901–3904, **1984**

XU, KS; JI, RC; ZHANG, ZM:
A NEW METHOD FOR MEASURING THE PHASE OF THE FOURIER SPECTRUM
OPTICS COMMUNICATIONS, Volume **50**, Issue 2, page 85–89, **1984**

BOBROFF, N:
RESIDUAL ERRORS IN LASER INTERFEROMETRY FROM AIR TURBULENCE AND NONLINEARITY
APPLIED OPTICS, Volume **26**, Issue 13, page 2676–2682, **1987**

NAKATANI, N; IZUMI, T; ASANO, S; YAMADA, T et al:
OPTICAL FIBER HETERODYNE INTERFEROMETER PROBE FREE FROM EXTERNAL DISTURBANCE
REVIEW OF SCIENTIFIC INSTRUMENTS, Volume **58**, Issue 11, page 2161–2164, **1987**

SUTTON, CM:
NONLINEARITY IN LENGTH MEASUREMENT USING HETERODYNE LASER MICHELSON INTERFEROMETRY
JOURNAL OF PHYSICS E-SCIENTIFIC INSTRUMENTS, Volume **20**, Issue 10, page 1290–1292, **1987**

CRETIN, B; XIE, WX; WANG, S; HAUDEN, D:
HETERODYNE INTERFEROMETERS - PRACTICAL LIMITATIONS AND IMPROVEMENTS
OPTICS COMMUNICATIONS, Volume **65**, Issue 3, page 157–162, **1988**

OHYAMA, N; KINOSHITA, S; CORNEJORODRIGUEZ, A; HONDA, T et al:
ACCURACY OF PHASE DETERMINATION WITH UNEQUAL REFERENCE PHASE-SHIFT
JOURNAL OF THE OPTICAL SOCIETY OF AMERICA A-OPTICS IMAGE SCIENCE AND, Volume **5**, Issue 12, page 2019–2025, **1988**

TANAKA, M; YAMAGAMI, T; NAKAYAMA, K:
LINEAR INTERPOLATION OF PERIODIC ERROR IN A HETERODYNE LASER INTERFEROMETER AT SUBNANOMETER LEVELS
IEEE TRANSACTIONS ON INSTRUMENTATION AND MEASUREMENT, Volume **38**, Issue 2, page 552–554, **1989**

AUGUSTYN, W; DAVIS, P:
AN ANALYSIS OF POLARIZATION MIXING ERRORS IN DISTANCE MEASURING INTERFEROMETERS
JOURNAL OF VACUUM SCIENCE & TECHNOLOGY B, Volume **8**, Issue 6, page 2032–2036, **1990**

FREISCHLAD, K; KOLIOPOULOS, CL:
FOURIER DESCRIPTION OF DIGITAL PHASE-MEASURING INTERFEROMETRY
JOURNAL OF THE OPTICAL SOCIETY OF AMERICA A-OPTICS IMAGE SCIENCE AND, Volume **7**, Issue 4, page 542–551, **1990**

ROSENBLUTH, AE; BOBROFF, N:
OPTICAL SOURCES OF NONLINEARITY IN HETERODYNE INTERFEROMETERS
PRECISION ENGINEERING-JOURNAL OF THE AMERICAN SOCIETY FOR PRECISION, Volume **12**, Issue 1, page 7–11, **1990**

MICHELETTI, R:
PHASE-ANGLE MEASUREMENT BETWEEN 2 SINUSOIDAL SIGNALS
IEEE TRANSACTIONS ON INSTRUMENTATION AND MEASUREMENT, Volume **40**, Issue 1, page 40–41, **1991**

OKA, K; TSUKADA, M; OHTSUKA, Y:
REAL-TIME PHASE DEMODULATOR FOR OPTICAL HETERODYNE-DETECTION PROCESSES
MEASUREMENT SCIENCE & TECHNOLOGY, Volume **2**, Issue 2, page 106–110, **1991**

SODNIK, Z; FISCHER, E; ITTNER, T; TIZIANI, HJ:
2-WAVELENGTH DOUBLE HETERODYNE INTERFEROMETRY USING A MATCHED GRATING TECHNIQUE
APPLIED OPTICS, Volume **30**, Issue 22, page 3139–3144, **1991**

HOU, WM; WILKENING, G:
INVESTIGATION AND COMPENSATION OF THE NONLINEARITY OF HETERODYNE INTERFEROMETERS
PRECISION ENGINEERING-JOURNAL OF THE AMERICAN SOCIETY FOR PRECISION, Volume **14**, Issue 2, page 91–98, **1992**

OKA, K; OHTSUKA, Y:
POLARIZATION HETERODYNE INTERFEROMETRY USING ANOTHER LOCAL OSCILLATOR BEAM
OPTICS COMMUNICATIONS, Volume **92**, Issue 1-3, page 1–5, **1992**

BOBROFF, N:
RECENT ADVANCES IN DISPLACEMENT MEASURING INTERFEROMETRY
MEASUREMENT SCIENCE & TECHNOLOGY, Volume **4**, Issue 9, page 907–926, **1993**

DEFREITAS, JM; PLAYER, MA:
IMPORTANCE OF ROTATIONAL BEAM ALIGNMENT IN THE GENERATION OF 2ND-HARMONIC ERRORS IN LASER HETERODYNE INTERFEROMETRY
MEASUREMENT SCIENCE & TECHNOLOGY, Volume **4**, Issue 10, page 1173–1176, **1993**

OLDHAM, NM; KRAMAR, JA; HETRICK, PS; TEAGUE, EC:
ELECTRONIC LIMITATIONS IN PHASE METERS FOR HETERODYNE INTERFEROMETRY
PRECISION ENGINEERING-JOURNAL OF THE AMERICAN SOCIETY FOR PRECISION, Volume **15**, Issue 3, page 173–179, **1993**

HOU, WM; ZHAO, XB:
DRIFT OF NONLINEARITY IN THE HETERODYNE INTERFEROMETER
PRECISION ENGINEERING-JOURNAL OF THE AMERICAN SOCIETY FOR PRECISION, Volume **16**, Issue 1, page 25–35, **1994**

DEFREITAS, JM; PLAYER, MA:
POLARIZATION EFFECTS IN HETERODYNE INTERFEROMETRY
JOURNAL OF MODERN OPTICS, Volume **42**, Issue 9, page 1875–1899, **1995**

GRACE, V; MOLESINI, G; QUERCIOLI, F:
ACCURATE POLARIZATION INTERFEROMETER
REVIEW OF SCIENTIFIC INSTRUMENTS, Volume **66**, Issue 7, page 3729–3734, **1995**

Chou, C; Huang, YC; Chang, M:
Polarized common path optical heterodyne interferometer for measuring the elliptical birefringence of a quartz wave plate
JAPANESE JOURNAL OF APPLIED PHYSICS PART 1-REGULAR PAPERS SHORT NOTES &, Volume **35**, Issue 10, page 5526–5529, **1996**

Hellings, R; Giampieri, G; Maleki, L; Tinto, M et al:
Heterodyne laser tracking at high Doppler rates
OPTICS COMMUNICATIONS, Volume **124**, Issue 3-4, page 313–320, **1996**

Park, BC; Eom, TB; Chung, MS:
Polarization properties of cube-corner retroreflectors and their effects on signal strength and nonlinearity in heterodyne interferometers
APPLIED OPTICS, Volume **35**, Issue 22, page 4372–4380, **1996**

Su, DC; Chiu, MH; Chen, CD:
A heterodyne interferometer using an electro-optic modulator for measuring small displacements
JOURNAL OF OPTICS-NOUVELLE REVUE D OPTIQUE, Volume **27**, Issue 1, page 19–23, **1996**

Wu, CM; Su, CS; Peng, GS:
Correction of nonlinearity in one-frequency optical interferometry
MEASUREMENT SCIENCE & TECHNOLOGY, Volume **7**, Issue 4, page 520–524, **1996**

Wui, CM; Su, CS:
Nonlinearity in measurements of length by optical interferometry
MEASUREMENT SCIENCE & TECHNOLOGY, Volume **7**, Issue 1, page 62–68, **1996**

DeFreitas, JM:
Analysis of laser source birefringence and dichroism on nonlinearity in heterodyne interferometry
MEASUREMENT SCIENCE & TECHNOLOGY, Volume **8**, Issue 11, page 1356–1359, **1997**

Leonard, F:
Referencing the phase to the centre of the spectral window. Why?
MECHANICAL SYSTEMS AND SIGNAL PROCESSING, Volume **11**, Issue 1, page 75–90, **1997**

Li, B; Liang, JW:
Effects of polarization mixing on the dual-wavelength heterodyne interferometer
APPLIED OPTICS, Volume **36**, Issue 16, page 3668–3672, **1997**

Onodera, R; Ishii, Y:
Fourier description of the phase-measuring process in two-wavelength phase-shifting interferometry
OPTICS COMMUNICATIONS, Volume **137**, Issue 1-3, page 27–30, **1997**

Quinn, BG:
Estimation of frequency, amplitude, and phase from the DFT of a time series
IEEE TRANSACTIONS ON SIGNAL PROCESSING, Volume **45**, Issue 3, page 814–817, **1997**

Sun, KX; Gustafson, EK; Fejer, MM; Byer, RL:
Polarization-based balanced heterodyne detection method in a Sagnac interferometer for precision phase measurement
OPTICS LETTERS, Volume **22**, Issue 17, page 1359–1361, **1997**

Surrel, Y:
Additive noise effect in digital phase detection
APPLIED OPTICS, Volume **36**, Issue 1, page 271–276, **1997**

Demarest, FC:
High-resolution, high-speed, low data age uncertainty, heterodyne displacement measuring interferometer electronics
MEASUREMENT SCIENCE & TECHNOLOGY, Volume **9**, Issue 7, page 1024–1030, **1998**

Huang, YC; Chou, C; Chou, LY; Shyu, JC et al:
Polarized optical heterodyne profilometer
JAPANESE JOURNAL OF APPLIED PHYSICS PART 1-REGULAR PAPERS SHORT NOTES &, Volume **37**, Issue 1, page 351–354, **1998**

Onodera, R; Ishii, Y:
Two-wavelength interferometry that uses a Fourier-transform method
APPLIED OPTICS, Volume **37**, Issue 34, page 7988–7994, **1998**

Stone, JA; Howard, LP:
A simple technique for observing periodic nonlinearities in Michelson interferometers
PRECISION ENGINEERING-JOURNAL OF THE AMERICAN SOCIETY FOR PRECISION, Volume **22**, Issue 4, page 220–232, **1998**

Wu, CM; Deslattes, RD:
Analytical modeling of the periodic nonlinearity in heterodyne interferometry
APPLIED OPTICS, Volume **37**, Issue 28, page 6696–6700, **1998**

Petru, F; Cip, O:
Problems regarding linearity of data of a laser interferometer with a single-frequency laser
PRECISION ENGINEERING-JOURNAL OF THE AMERICAN SOCIETY FOR PRECISION, Volume **23**, Issue 1, page 39–50, **1999**

Wu, CM; Lawall, J; Deslattes, RD:
Heterodyne interferometer with subatomic periodic nonlinearity
APPLIED OPTICS, Volume **38**, Issue 19, page 4089–4094, **1999**

Yin, CY; Dai, GL; Chao, ZX; Xu, Y et al:
Determining the residual nonlinearity of a high-precision heterodyne interferometer
OPTICAL ENGINEERING, Volume **38**, Issue 8, page 1361–1365, **1999**

Yokoyama, S; Ohnishi, J; Iwasaki, S; Seta, K et al:
Real-time and high-resolution absolute-distance measurement using a two-wavelength superheterodyne interferometer
MEASUREMENT SCIENCE & TECHNOLOGY, Volume **10**, Issue 12, page 1233–1239, **1999**

Zhao, Y; Zhou, T; Li, DC:
Heterodyne absolute distance interferometer with a dual-mode HeNe laser
OPTICAL ENGINEERING, Volume **38**, Issue 2, page 246–249, **1999**

Badami, VG; Patterson, SR:
A frequency domain method for the measurement of nonlinearity in heterodyne interferometry
PRECISION ENGINEERING-JOURNAL OF THE INTERNATIONAL SOCIETIES FOR, Volume **24**, Issue 1, page 41–49, **2000**

Guo, JH; Zhang, Y; Shen, S:
Compensation of nonlinearity in a new optical heterodyne interferometer with doubled measurement resolution
OPTICS COMMUNICATIONS, Volume **184**, Issue 1-4, page 49–55, **2000**

Heilmann, RK; Konkola, PT; Chen, CG; Schattenburg, ML:
Relativistic corrections in displacement measuring interferometry
JOURNAL OF VACUUM SCIENCE & TECHNOLOGY B, Volume **18**, Issue 6, page 3277–3281, **2000**

Lawall, J; Kessler, E:
Michelson interferometry with 10 pm accuracy
REVIEW OF SCIENTIFIC INSTRUMENTS, Volume **71**, Issue 7, page 2669–2676, **2000**

Lin, DJ; Jiang, H; Yin, CY:
Analysis of nonlinearity in a high-resolution grating interferometer
OPTICS AND LASER TECHNOLOGY, Volume **32**, Issue 2, page 95–99, **2000**

Surrel, Y:
Fringe analysis
PHOTO-MECHANICS, Volume **77**, Issue , page 55–102, **2000**

Yim, NB; Eom, CI; Kim, SW:
Dual mode phase measurement for optical heterodyne interferometry
MEASUREMENT SCIENCE & TECHNOLOGY, Volume **11**, Issue 8, page 1131–1137, **2000**

Eom, T; Kim, J; Jeong, K:
The dynamic compensation of nonlinearity in a homodyne laser interferometer
MEASUREMENT SCIENCE & TECHNOLOGY, Volume **12**, Issue 10, page 1734–1738, **2001**

Goldberg, KA; Bokor, J:
Fourier-transform method of phase-shift determination
APPLIED OPTICS, Volume **40**, Issue 17, page 2886–2894, **2001**

Koning, R; Dixson, R; Fu, J; Vorburger, TV:
The role of periodic interferometer errors in the calibration of capacitance displacement sensors for nanometrology applications
MEASUREMENT SCIENCE & TECHNOLOGY, Volume **12**, Issue 11, page 2002–2008, **2001**

Yokoyama, T; Araki, T; Yokoyama, S; Suzuki, N:
A subnanometre heterodyne interferometric system with improved phase sensitivity using a three-longitudinal-mode He-Ne laser
MEASUREMENT SCIENCE & TECHNOLOGY, Volume **12**, Issue 2, page 157–162, **2001**

Chen, BY; Cheng, XH; Li, DC:
Dual-wavelength interferometric technique with subnanometric resolution
APPLIED OPTICS, Volume **41**, Issue 28, page 5933–5937, **2002**

Connelly, MJ:
Digital synthetic-heterodyne interferometric demodulation
JOURNAL OF OPTICS A-PURE AND APPLIED OPTICS, Volume **4**, Issue 6, page S400–S405, **2002**

Cosijns, SJAG; Haitjema, H; Schellekens, PHJ:
Modeling and verifying non-linearities in heterodyne displacement interferometry
PRECISION ENGINEERING-JOURNAL OF THE INTERNATIONAL SOCIETIES FOR, Volume **26**, Issue 4, page 448–455, **2002**

Dubovitsky, S; Lay, OP; Seidel, DJ:
Elimination of heterodyne interferometer nonlinearity by carrier phase modulation
OPTICS LETTERS, Volume **27**, Issue 8, page 619–621, **2002**

Eom, T; Choi, T; Lee, K; Choi, H et al:
A simple method for the compensation of the nonlinearity in the heterodyne interferometer
MEASUREMENT SCIENCE & TECHNOLOGY, Volume **13**, Issue 2, page 222–225, **2002**

Halverson, PG; Spero, RE:
Signal processing and testing of displacement metrology gauges with picometre-scale cyclic nonlinearity
JOURNAL OF OPTICS A-PURE AND APPLIED OPTICS, Volume **4**, Issue 6, page S304–S310, **2002**

Lay, OP; Dubovitsky, S:
Polarization compensation: a passive approach to a reducing heterodyne interferometer nonlinearity
OPTICS LETTERS, Volume **27**, Issue 10, page 797–799, **2002**

Lin, DJ; Yan, JQ; Chao, ZX; Jiang, H et al:
Phasemeter with external trigger applied to PZT-modulated interferometer
INTERNATIONAL JOURNAL OF ELECTRONICS, Volume **89**, Issue 10, page 759–769, **2002**

Logan, JE; Halverson, PG; Regehr, MW; Spero, RE:
Automatic alignment of a displacement-measuring heterodyne interferometer
APPLIED OPTICS, Volume **41**, Issue 21, page 4314–4317, **2002**

Peggs, GN; Yacoot, A:
A review of recent work in sub-nanometre displacement measurement using optical and X-ray interferometry
PHILOSOPHICAL TRANSACTIONS OF THE ROYAL SOCIETY OF LONDON SERIES, Volume **360**, Issue 1794, page 953–968, **2002**

Wu, CM; Lin, ST; Fu, J:
Heterodyne interferometer with two spatial-separated polarization beams for nanometrology
OPTICAL AND QUANTUM ELECTRONICS, Volume **34**, Issue 12, page 1267–1276, **2002**

Zhao, HJ; Zhang, GJ:
Nonlinear error by orientation and elliptic polarization in a two-beam interferometer
OPTICAL ENGINEERING, Volume **41**, Issue 12, page 3204–3208, **2002**

Li, Z; Herrmann, K; Pohlenz, F:
A neural network approach to correcting nonlinearity in optical interferometers
MEASUREMENT SCIENCE & TECHNOLOGY, Volume **14**, Issue 3, page 376–381, **2003**

Lorier, DJ; Knarren, BAWH; Cosijns, SJAG; Haitjema, H et al:
Laser polarization state measurement in heterodyne interferometry
CIRP ANNALS-MANUFACTURING TECHNOLOGY, Volume **52**, Issue 1, page 439–442, **2003**

Muller, H; Herrmann, S; Schuldt, T; Scholz, M et al:
Offset compensation by use of amplitude-modulated sidebands in optical frequency standards
OPTICS LETTERS, Volume **28**, Issue 22, page 2186–2188, **2003**

Schmitz, TL; Beckwith, JE:
An investigation of two unexplored periodic error sources in differential-path interferometry
PRECISION ENGINEERING-JOURNAL OF THE INTERNATIONAL SOCIETIES FOR, Volume **27**, Issue 3, page 311–322, **2003**

Wu, CM:
Periodic nonlinearity resulting from ghost reflections in heterodyne interferometry
OPTICS COMMUNICATIONS, Volume **215**, Issue 1-3, page 17–23, **2003**

Yang, SY; Takajo, H:
Quantization error reduction in the measurement of Fourier intensity for phase retrieval
JAPANESE JOURNAL OF APPLIED PHYSICS PART 1-REGULAR PAPERS SHORT NOTES &, Volume **43**, Issue 8B, page 5747–5751, **2004**

Park, TJ; Choi, HS; Han, CS; Lee, YW:
Real-time precision displacement measurement interferometer using the robust discrete time Kalman filter
OPTICS AND LASER TECHNOLOGY, Volume **37**, Issue 3, page 229–234, **2005**

References

[1] Robertson, D; Ward, H et al: Presentation given at progress meeting, ESTEC 2003.

[2] B. Razavi, 'RF Microelectronics', Prentice-Hall 1998.

[3] I.S. Gradstein; I.M. Ryshik: 'Tables of Series, Products and Integrals', Harri Deutsch 1981

[4] W.H. Press, S.A. Teukolsky, W.T. Vetterling, B.P. Flannery: 'Numerical Recipes in C, The Art of Scientific Computing', Cambridge University Press, 2nd ed., 1992.

[5] G. Heinzel, A. Rüdiger and R. Schilling:
"Spectrum and spectral density estimation by the Discrete Fourier transform (DFT), including a comprehensive list of window functions and some new flat-top windows",
Internal report, AEI Hannover, February 2002.

[6] "S2-AEI-TN-3017: Lisa Pathfinder Optical Bench Engineering model: functional and performance tests – Test Report",
Gerhard Heinzel, Vinzenz Wand, Antonio Garcia,
June 2004.

[7] Yves Surrel, Topics App. Phys. **77**, 55-102 (2000).

[8] Klaus Freischlad and Chris L. Koliopoulos, J. Opt. Soc. Am. A. **7**, 542-551

[9] Heinzel, G; Braxmaier, C; Schilling, R; Rudiger, A; Robertson, D; Plate, MT; Wand, V; Arai, K; Johann, U; Danzmann, K:
Interferometry for the LISA technology package (LTP) aboard SMART-2
CLASSICAL AND QUANTUM GRAVITY, Volume **20**, Issue 10, page S153–S161, **2003**

[10] Heinzel, G; Wand, V; Garcia, A; Jennrich, OP; Braxmaier, C; Robertson, D; Middleton, K; Hoyland, D; Rudiger, A; Schilling, R; Johann, U; Danzmann, K:
The LTP interferometer and phasemeter
CLASSICAL AND QUANTUM GRAVITY, Volume **21**, Issue 5, page S581–S587, **2004**

[11] Heinzel G, Braxmaier C, Caldwell M, Danzmann K, Draaisma F, Garcia A, Hough J, Jennrich O, Johann U, Killow C, Middleton K, te Plate M, Robertson D, Rudiger A, Schilling R, Steier F, Wand V, Ward H :
Successful testing of the LISA Technology Package (LTP) interferometer engineering model
CLASSICAL AND QUANTUM GRAVITY, Volume **22**, Issue 10, page S149–S154, **2005**

[12] "PRE-INVESTIGATION TEST PLAN AND EVALUATION REPORT",
D Robertson, J Hough, C Killow and H Ward,
28th November 2002

[13] "The effect of fibre path stabilisation on the stability measurements on the bonded breadboard optical bench",
D Robertson, J Hough, C Killow and H Ward,
10/03/2004

[14] "SMART-2 interferometer", G Heinzel, Technical note S2-AEI-TN-3010, 2002/09/17.